CO_2-SELECTIVE POLYMER BRUSH MEMBRANES AND ANTIBACTERIAL POLYELECTROLYTE MULTILAYER MEMBRANES: SYNTHESIS, CHARACTERIZATION, AND APPLICATION

By

Sebastian T. Grajales

A DISSERTATION

Submitted to
Michigan State University
in partial fulfillment of the requirement
for the degree of

Chemistry - Doctor of Philosophy

2014

ABSTRACT

CO_2-SELECTIVE POLYMER BRUSH MEMBRANES AND ANTIBACTERIAL POLYELECTROLYTE MULTILAYER MEMBRANES: SYNTHESIS, CHARACTERIZATION, AND APPLICATION

By

Sebastian T. Grajales

Composite membranes consist of a selective skin on a highly permeable support. The minimal thickness of the skin layer affords relatively high flux along with selectivity, whereas the support provides mechanical strength. This dissertation presents methods for improving the function of composite membranes prepared by either polymerization from a porous substrate or alternating polyelectrolyte deposition on ultrafiltration membranes. Specifically, this work aims to create gas-separation membranes that selectively remove CO_2 from H_2 streams and nanofiltration membranes that resist biofouling.

Steam reforming of hydrocarbons followed by the water gas shift reaction yields H_2 streams that contain 20 % CO_2 as a byproduct. Ideally, in membrane-based purification of these streams, the CO_2 should preferentially pass through the membrane so the H_2 remains at high pressure. Because H_2 is smaller than CO_2, membranes that selectively pass CO_2 must have a high CO_2/H_2 solubility selectivity and minimal diffusive resistance. Amorphous poly(ethylene glycol) (PEG) possesses these properties, but crystallization of PEG chains dramatically decreases flux and eliminates selectivity. One goal of this research is to create ultrathin, PEG-containing membrane skins in which PEG chains do not crystallize. Surface-initiated atom transfer radical polymerization of PEG-methyl ether methacrylate (PEGMEMA) monomers produces thin (<200 nm) membrane skins on porous substrates, but crystallization of long PEG side chains (22-23 ethylene oxide units) restricts both flux and selectivity. However, copolymerization of monomers

containing 8-9 and 22-23 ethylene glycol units yields membranes that maintain a CO_2/H_2 selectivity of 13 or more, which is equal to the highest reported room-temperature CO_2/H_2 selectivities. The short PEG chains in these films frustrate crystallization, and the high PEG content in the larger monomers leads to high selectivity.

Formation of nanoparticles in membrane skins also inhibits room-temperature PEG crystallization. The incorporation of tetraisopropoxytitanate into a poly(PEGMEMA) film and subsequent condensation to TiO_2 nanoparticles yields a nanocomposite membrane that maintains a CO_2/H_2 selectivity of 6 over time. A small amount of crystallization in these films likely decreases selectivity from ~13 to 6. Unfortunately, the use of higher nanoparticle concentrations to better frustrate crystallization leads to defect formation and elimination of selectivity.

Membranes employed in aqueous environments commonly exhibit a decrease in permeability over time due to fouling. Biofouling, the formation of a microbial foulant layer, is particularly intrusive because even a few cells can multiply to create a film that reduces permeability. One goal of this research is to create skin layers that both kill bacteria and provide useful ion-transport selectivities. Alternating layer-by-layer deposition of poly(styrene sulfonate) and polycations containing antibacterial guanidine groups generates a surface that resists biofouling. Reflectance FTIR spectra confirm the layer-by-layer growth of these polyelectrolyte films on Al-coated Si wafers, and filtration of bacterial solutions show that multilayer films can be 100% bactericidal at short times. However, preliminary dead-end filtration studies reveal $MgCl_2$ and NaCl rejections <50%. Future work will examine the permeability of these membranes in cross-flow filtration and investigate methods to improve ion-transport selectivity.

This Dissertation is dedicated to all of my family, and in particular my wife, Ann, and my daughters, Liliana and Isabel.

ACKNOWLEDGEMENTS

First, I would like to thank my advisor, Merlin Bruening. My relationship with him started when I attended one of his presentations and experienced his energy, enthusiasm, and passion for good science. I wish that I could better communicate my gratitude for him accepting me into his group, supporting my research, and strengthening many of my weaknesses. He is a friend and a mentor to me, not to mention the fact that his ability to earn grant money funded my research!

I thank my committee members Greg Baker, Volodymyr Tarabara, and Gary Blanchard for helping me. I would also like to thank earlier committee members Mercouri Kanatzidis for giving me advice and guidance, Mitch Smith for helping me through the transition of changing advisors, and Tom Pinnavaia for teaching me many concepts in the field of inorganic synthesis, as well as how to prepare for presentations and improve my technical writing ability.

Next, I would like to thank the Bruening group members: Jamie, Elizabeth, Sri, Somnath, David, Maneesha, Weihan, Xiaojie, Yujing, and Seth for supporting me and being good colleagues and friends.

Finally, I thank my family. My wife, Ann, supported me for all these years and my daughters, Liliana and Isabel, gave my life a new level of meaning. I wouldn’t be here without the support of my Mom, who has always believed that I could do anything. I thank my Dad and Stepmom who always encouraged me. I am very grateful for the support of my family.

TABLE OF CONTENTS

LIST OF TABLES ix

LIST OF FIGURES x

LIST OF SCHEMES xv

KEY TO ABBREVIATIONS xvi

Chapter One. Separations Using Polymer Membranes 1
- An Overview 1
- Classification of Membranes Processes 4
- Solution-diffusion permeation through dense membranes 6
- Penetrant Solubility 16
- Permeation through porous membranes 22
- Non-Ideal Membrane Performance 25
  - Concentration Polarization 26
  - Biofouling 29
- Synthesis of Selective, High-Flux Membranes 30
  - Atom transfer radical polymerization 31
- Research Overview 33
- REFERENCES 34

Chapter Two. Effects of Monomer Composition on CO_2-Selective Polymer Brush Membranes 41
- Introduction 41
- Experimental 45
  - Chemicals 45
  - Polymerization 46
  - Characterization methods 47
  - Gas Permeation 47
- Results and Discussion 49
  - Polymerization Rates as a Function of Monomer Composition 49
  - Determining the Composition of Copolymer Films 51
  - Crystallization of PEG Side Chains 56
  - Formation of Gas-Separation Membranes by ATRP 58
  - Gas Permeation through Poly(PEGMEMA) Membranes 59
- Summary 63
- Acknowledgements 64
- APPENDIX 65
- Determination of absorption coefficients in reflectance IR spectra 66
- Conclusions 72
- REFERENCES 73

Chapter Three. The effect of nanoparticles on CO_2-selective polymer membranes 77

Introduction 77
Experimental 82
    Chemicals 82
    Polymerization 83
    Formation of the Polymer-nanoparticle Composite Film 84
    Characterization methods 84
    Gas Permeation 85
Results and Discussion 86
    Membrane Synthesis 86
    Inhibition of Crystallization by TiO_x Nanoparticles 87
    Changes in Membrane Permeability due to Nanoparticle Formation 92
Conclusions 95
REFERENCES 97

Chapter Four. Guanidine-Based Antifouling, Ion-selective Membranes 102
Introduction 102
Materials and Method 105
    Preparation of films 105
    Characterization of solute rejection 106
    Evaluation of membrane antimicrobial activity 107
Results 108
    Membrane Surface Characterization 108
    Zeta Potentials 114
    Antibacterial Activity 116
    Transport properties 118
Conclusions 122
REFERENCES 124

LIST OF TABLES

Table 1.1: Physical/chemical properties exploited in chemical separations and the corresponding separation techniques. Adapted and modified from Mulder.[3] 2

Table 1.2: Selected milestones in understanding gas separations. Modified from reference 5. 7

Table 1.3: The three possible combinations of solubility and diffusivities that lead to selective gas transport, along with gas separations that employ these scenarios. Adapted from Pinnau and Freeman.[10] 11

Table 1.4: Kinetic diameters[a] and critical temperatures of various gases.[13] 14

Table 2.1: Composition of poly(PEGMEMA-475-*co*-PEGMEMA-1100) films[a] as a function of the PEGMEMA-475 mole percentages in the polymerization solution.[b] 56

Table A.1: Absorption coefficients, k, of homopolymer films. The k values were calculated using Eq. (A.1-A.5) and the peak absorbances corresponding to C-O-C and C=O stretches. The uncertainty is one standard deviation of the values obtained from films with a range of thicknesses. 70

Table 3.1: Selected nanoscale fillers in polymer materials and their corresponding applications. POSS is polyhedral oligomeric silsesquioxane..78

Table 3.2: Permeation properties of poly(PEGMEMA) membranes and poly(PEGMEMA) membranes containing TiO_2 nanoparticles, poly(PEGMEMA)-TiO_2. Transport measurements were made immediately after membrane preparation and one day later. 88

Table 4.1: Strong infrared absorption modes for PSS/PHMG and PSS/PHMB films. 108

LIST OF FIGURES

Figure 1.1: Schematic drawing of a membrane separating two phases. 3

Figure 1.2: Classification of membrane processes according to the size of the species being rejected. Adapted from reference 9. 5

Figure 1.3: Schematic diagram of different types of transport through porous and non-porous membranes. Adapted from Ho and Sirkar.[4] 6

Figure 1.4: Concentration profile of an analyte during solution-diffusion through a membrane, where c_1, c_2, c_3, and c_4 represent the concentrations of the analyte in the feed, upstream face of the membrane, downstream face of the membrane, and permeate, respectively. (This diagram neglects concentration polarization, which is discussed below.) 8

Figure 1.5: Concentration profile of a penetrant gas in a membrane from c_1 at the feed face to c_2 at the permeant face. The partial pressure levels are shown for the feed (p_1) and permeant (p_2) gas. 10

Figure 1.6: Schematic diagram of a size-selective separation with a composite membrane. The membrane has higher permeability for the smaller molecules due to diffusivity selectivity or molecular sieving. The low pressure side (right) of the membrane contains a higher fraction of small molecules than the feed side. 12

Figure 1.7: Schematic diagram of reverse selectivity. In this case, the membrane has higher permeability for larger molecules due to solubility selectivity. The lower pressure permeate side (right) of the membrane contains a higher fraction of the larger molecules than the feed side.....13

Figure 1.8: Polymer volume relative to temperature. Modified from Zolandz and Fleming.[14]....15

Figure 1.9: Overview of various phenomena that generate resistance to convective flux. The various resistances stem from the ideal membrane-R_m, cake layer formation-R_c, pore blocking-R_b, concentration polarization-R_{cp}, and adsorption-R_a. 26

Figure 1.10: Simplified scheme of a concentration profile (a) under a concentration driven membrane separation with perfect mixing and (b) with concentration polarization at the feed interface under steady-state conditions. The concentration at c_1 does not necessarily equal c_2, and c_3 does not necessarily equal c_4. Note that in the case of concentration polarization the concentration begins to increase at a distance δ, along the x-axis, from the membrane surface...27

Figure 1.11: Schematic drawings of (a) a dead-end membrane and (b) a cross-flow membrane module. In the dead-end mode the concentrations of rejected species continually increase on the feed side of the membrane, whereas the cross-flow module allows for rejected species to flow along the membrane face and out of the module via the retentate path. 29

Figure 1.12: Decreases in transmembrane flux over time, due to concentration polarization and fouling. 30

Figure 1.13: Reactions involved in ATRP. The ATRP mechanism contains an equilibrium where a dormant chain (R-X) activates at a rate of kact to form a radical (R●) and deactivates at a rate of k_{deact} to return to the protected state. Transition metals (TM) at two different oxidation states ("a" and "a+1") complexed with ligand(s) mediate the process. The active radical reacts with monomer to form polymer with a rate constant of k_p or terminates with a neighboring radical with a rate constant of k_t. 32

Figure 2.1: Evolution of film thickness with time in surface-initiated polymerization of pure and mixed monomer solutions. For copolymers, the legend shows the solution PEGMEMA-475 mole percentage with respect to the total monomer (PEGMEMA-475 plus PEGMEMA-1100). The overall monomer concentration was 0.67 M, and the catalyst system was 2.0 mM CuCl, 0.60 mM CuBr2, and 6.0 mM HMTETA. The error bars, which in many cases are obscured by the symbols, represent one standard deviation. 50

Figure 2.2: FTIR spectra of 152 nm-thick poly(PEGMEMA-475) (black line) and 118 nm-thick poly(PEGMEMA-1100) (dashed red line) films on gold-coated substrates. Spectra were taken immediately after polymerization before the PEG side chains in poly(PEGMEMA-1100) crystallized. The spectra are offset for clarity. 52

Figure 2.3: Ratios of C-O-C to C=O peak heights (A) and peak areas (B) in reflectance FTIR spectra of poly(PEGMEMA-1100), poly(PEGMEMA-475), poly(PEGMEMA-300) and poly(PEGMEMA-475-co-PEGMEMA-1100) films on gold-coated substrates. The ratios are plotted as a function of the ellipsometric thickness of the film, and for the copolymers, the legend shows the mole fraction of PEGMEMA-475 (relative to total monomer) in the polymerization solution. All polymerizations employed a total monomer concentration of 0.67 M, and the experimental section describes the polymerization conditions. 54

Figure 2.4: Ratios of C-O-C (1149 cm^{-1}) and C=O (1731 cm^{-1}) absorption coefficients, k, as a function of the average number of ethylene oxide units per repeat unit, EO_{avg}, in poly(PEGMEMA-300), poly(PEGMEMA-475), and poly(PEGMEMA-1100) films. The ethylene oxide units per monomer were calculated from ^{1}H-NMR spectra of monomers, and the standard deviations in the absorption coefficient ratios were determined using films with thicknesses ranging from 5 to 454 nm. The line is a fit to the data with a zero intercept. 55

Figure 2.5: Reflectance FTIR spectra of (A) 60 nm-thick poly(PEGMEMA-1100) immediately after polymerization (solid black line) and 24 hours later (dashed red line) and (B) 97 nm-thick poly(PEGMEMA-475-co-PEGMEMA-1100) immediately after polymerization (solid black line) and 404 days later (dashed red line). The copolymer was prepared from a solution containing 25 mole% PEGMEMA-475 and 75 mole% PEGMEMA-1100. 57

Figure 2.6: SEM image of the cross section of a gold-coated porous alumina membrane modified with a poly(PEGMEMA-475-co-PEGMEMA-1100) film. The alumina exhibits unfilled vertical

pores covered by a 130 nm-thick film that was grown from an aqueous solution containing 25 mole% PEGMEMA-475 and 75 mole% PEGMEMA-1100. 59

Figure 2.7: Single-gas fluxes through gold-coated porous alumina membranes capped with (A) poly(PEGMEMA-1100) or (B) poly(PEGMEMA-475-co-PEGMEMA-1100) grown from a solution containing 50 mole% PEGMEMA-475. (Fluxes are normalized by multiplying by the SEM thickness of the membrane skin.) The circles represent CO_2 data, and the triangles represent H_2 data; filled symbols represent measurements taken immediately after synthesis, and open symbols represent data obtained 24 h later. The inset in Figure A shows the data on an expanded ordinate for clarity...60

Figure 2.8: Single-gas CO_2/H_2 selectivity vs. mole fraction of PEGMEMA-475 in the monomer solution used to create amorphous poly(PEGMEMA-475-co-PEGMEMA-1100) films on porous alumina membranes. The triangles represent films grown from silylated alumina, and the squares represent films grown from initiators on gold-coated alumina. For the poly(PEGMEMA-1100) homopolymer on silylated alumina, the open circle near the origin represents selectivity after crystallization. Error bars are one standard deviation...62

Figure A.1: Schematic drawing of the reflection of light from (A) a bare gold surface and (B) a film-covered gold surface. 66

Figure A.2: Ratios of the C-O-C (1149 cm^{-1}) and C=O (1731 cm^{-1}) absorption coefficients in poly(PEGMEMA) homo and copolymer films as a function of film thickness. In the case of copolymer films, the legend shows the PEGMEMA-475 mole percentage of total monomer in the polymerization solution, and the rest of the monomer was PEGMEMA-1100. The polymerization was performed as described in the experimental section. 69

Figure A.3: Proton NMR spectra of (A) PEGMEMA-300, (B) PEGMEMA-475, and (C) PEGMEMA-1100. Peak areas in these spectra were averaged with areas from two additional replicate spectra to generate values for the number of average ethylene oxide units per monomer. 71

Figure 3.1: Cross-sectional scheme of the tortuous path of a permeant molecule traversing a polymer film containing dispersed, impermeable 2-D nanoparticles. 79

Figure 3.2: Permeability of a composite film as a function of filler volume fraction as predicted by the Maxwell equation. The polymer matrix has a permeability of 1 Barrer, and the filler is impermeable...80

Figure 3.3: Schematic drawing of the formation of nanoparticles to generate a nanocomposite polymer brush. 82

Figure 3.4: Reflectance FTIR of poly(PEGMEMA) immediately after synthesis (dashed red line) and after 24 hours at room temperature (black line)...89

Figure 3.5: Surface of poly(PEGMEMA) after a day at room temperature viewed through a cross-polarized optical microscope. 90

Figure 3.6: Reflectance FTIR spectra of a 44 nm-thick poly(PEGMEMA) film before and after treatment with TPOT to form nanoparticle films. Spectra were obtained immediately after film formation before crystallization could occur. 91

Figure 3.7: Reflectance FTIR spectra of a 44 nm-thick poly(PEGMEMA)-TiO_2 film generated by soaking in 0.1 M TPOT solution overnight. The spectra taken immediately upon removal from the TPOT solution (dashed red) and 24 hours later (black) showed little difference. 92

Figure 3.8: Permeances of poly(PEGMEMA)-TiO_2 membranes as a function of the TPOT concentration employed for nanoparticle formation. The measurements were taken after membrane aging overnight at room temperature. The black triangles correspond to CO_2 and the red circles to H_2. (The CO_2 permeance of the unmodified membrane, 0 M TPOT, was below the detection limit of the system.)..94

Figure 3.9: CO_2/H_2 selectivities of poly(PEGMEMA-1100) membranes as a function of the TPOT concentration used to modify the membranes prior to aging for one day at room temperature. ...95

Figure 4.1: Reflectance FTIR spectra (3600-2800 cm^{-1}) of $(PSS/PHMG)_x$ films adsorbed on aluminum-coated Si wafers..109

Figure 4.2: Reflectance FTIR spectra (1800-1000 cm^{-1}) of $(PSS/PHMG)_x$ films adsorbed on aluminum-coated Si wafers..110

Figure 4.3: Peak heights (1643 and 1008.6 cm^{-1}) in reflectance FTIR spectra of $(PSS/PHMG)_x$ films as a function of the number of adsorbed bilayers, x. 111

Figure 4.4: Reflectance FTIR spectra (1800-1000 cm^{-1}) of $(PSS/PHMB)_x$ films adsorbed on Al-coated Si wafers. 112

Figure 4.5: Reflectance FTIR spectra of 0.5-6 bilayers of $(PSS/PHMB)_x$ films adsorbed on aluminum-coated Si wafers..113

Figure 4.6: The peak heights of reflectance FTIR spectra of $(PSS/PHMB)_x$ films as a function of the number of adsorbed bilayers, x. Absorption increases with every sequential layer. 114

Figure 4.7: Zeta potentials of (PSS/PHMG) multilayers deposited on 50 kDa PES membranes. Each data point represents an average zeta potential of at least two samples generated on the same day using the same solutions. The pH refers to the electrolyte deposition solution as described in the experimental section. (Films with integer numbers of bilayers terminate with PHMG, whereas fractional bilayer numbers indicate termination with PSS.) 115

Figure 4.8: The bactericidal activity of 20 kDa PES membranes coated with $(PSS/PHMB)_x$ and $(PSS/PHMG)_x$ films. Activity was calculated by counting the number of colony forming units on bare and coated membranes [see Eq. (1.2)]. 117

Figure 4.9: Membrane pure water permeability as a function of the number of bilayers, x, for $(PSS/PHMG)_x$- and $(PSS/PHMB)_x$-modified 20 kDa PES ultrafiltration membranes. The pure flux was measured under a transmembrane pressure of 300 kPa. 119

Figure 4.10: NaCl rejection in dead-end filtration of 0.01 M NaCl solutions through 20 kDa PES ultrafiltration membranes coated with $(PSS/PHMB)_x$ (black triangles) and $(PSS/PHMG)_x$ (red circles) films 120

Figure 4.11: $MgSO_4$ rejection in dead-end filtration of 0.01 M $MgSO_4$ solutions through 20 kDa PES ultrafiltration membranes coated with $(PSS/PHMB)_x$ (black triangles) and $(PSS/PHMG)_x$ (red circles) films 121

Figure 4.12: $(NH_4)_3PO_4$ rejection in dead-end filtration of 0.01 M $(NH_4)_3PO_4$ solutions through 20 kDa PES ultrafiltration membranes coated with $(PSS/PHMB)_x$ (black triangles) and $(PSS/PHMG)_x$ (red circles) films. 122

LIST OF SCHEMES

Scheme 2.1: Methods for growth of a poly(PEGMEMA) membrane from porous alumina. 44

Scheme 2.2: Copolymerization of PEGMEMA-475 and PEGMEMA-1100 to provide a membrane skin. 45

Scheme 4.1: Preparation of an antibacterial polyelectrolyte multilayer film using (a) poly(styrenesulfonate) (PSS), and (b) poly(hexamethylene guanidine) (PHMG) or (c) poly(hexamethylene biguanidine) (PHMB). 103

Scheme 4.2: Mechanism of PHMB antibacterial action. (a) The healthy bacterial membrane contains a mixture of acidic and neutral phospholipids. (b) PHMB adsorbs to the bacterial membranes through interaction with phospholipds. (c) The affinity of PHMB for acidic phospholipids leads to sequestration of these phospholipids under the polymer. (d) Lipid sequestration leads to membrane deformation and eventually cellular leakage and death. Reproduced with permission from [37] 104

KEY TO ABBREVIATIONS

ATRP	atom transfer radical polymerization
b	ratio of the rate constants for adsorption and desorption
cb	bulk concentration
c'_H	gas capacity constant
cmHg	centimeters of mercury
CRP	controlled radical polymerization
D	diffusivity coefficient
Da	dalton
D_K	Knudsen diffusion coefficient
DMF	dimethylformamide
FTIR	fourier transform infrared spectroscopy
GC	gas chromatography
H	enthalpy
HMTETA	1,1,4,7,10,10-hexamethyltriethylenetetramine
i.d.	inner diameter
J	flux
K	partition coefficient
k	mass transfer coefficient
k	absorption coefficient
k_{act}	rate constant for the radical activation formation
K_{ATRP}	equilibrium constant for the activation/deactivation reaction

k_{deact}	rate constant for the deactivation reaction
k_p	rate constant for polymerization
k_t	rate constant for termination
l	thickness
L	ligand
[M]	monomer concentration
M_n	number average molecular weight
mol	mole
N	number of species
$\tilde{n}$	complex refractive index
N_2	nitrogen
NMR	nuclear magnetic resonance
P	permeability coefficient
p	partial pressure
Pa	Pascal
PEG	poly(ethylene glycol)
PEO	poly(ethylene oxide)
poly(PEGMEMA)	poly(ethylene glycol) methyl ether methacrylate
ppm	parts per million
r	radius
R•	radical terminated chain
R_a	non-ideal adsorption resistance

R_b	non-ideal pore blocking resistance
R_c	non-ideal cake layer resistance
R_{CO}	absorbance ratio for copolymer
R_{cp}	non-ideal concentration polarization resistance
R_m	ideal membrane resistance
RO	reverse osmosis
R_{tot}	total resistance to mass transport
R-X	halogen-capped dormant chain
S	solubility coefficient
s	distance away from pore wall
S	position at a distance x along a pore and s from a pore wall
STP	standard temperature and pressure
T	temperature
T_c	critical temperature
T_g	glass transition temperature
THF	tetrahydrofuran
TM	transition metal
$\bar{u}$	molecular velocity
V_g	glassy volume
V_l	theoretical densified volume
x	mole fraction of a given molecule
x	distance along a pore
z	coordination number around a given molecule

α	selectivity
β	a given angle from the pore wall
δ	solubility parameter
δ	stagnant layer thickness
ΔG_M	Gibbs' free energy of mixing
ΔH_M	enthalpy of mixing
ΔH_{vap}	enthalpy of vaporization
Δp	pressure gradient
ΔS_M	entropy of mixing
ε	porosity
η	viscosity
λ	mean free path
σ	number of segments in a given polymer chain
τ	tortuosity
φ	volume fraction of a given component
ΦN_2	sweep gas flow rate
χ	Flory-Huggins interaction parameter
Ω	number of distinguishable arrangements of molecules
ω	interaction energy between two molecules

Chapter One

Separations Using Polymer Membranes

An Overview

Chemical separations are at the heart of the chemical and petrochemical industries and represent some of the most costly and energy-intensive steps in industrial production. For example, a recent U.S. DOE target for CO_2 sequestration set a goal of 90% CO_2 sequestration at a cost increase of not more than 30% of the cost of power plant electricity.[1] The CO_2 separation process accounts for 60-80% of the overall isolation, transportation, and storage process needed to accomplish this goal.[2]

Industrial separations make use of a wide range of methods, but the physical and chemical differences among the species being separated limit the choice of the purification technique. Table 1.1 lists some important separation processes and the properties that they exploit.[3] Combinations of separation techniques are also possible.

Over the past 40 years, membrane-based separations have emerged as industrially viable alternatives to traditional processes such as distillation.[4] In these separations, a membrane divides two bulk phases between which selective transport occurs (Figure 1.1).[4]

Table 1.1: Physical/chemical properties exploited in chemical separations and the corresponding separation techniques. Adapted and modified from Mulder.[3]

physical/chemical property	separation process
size	microfiltration, ultrafiltration, dialysis, gas separation, gel permeation chromatography
vapor pressure	distillation, membrane distillation
freezing point	crystallization
critical point	gas separation
charge	ion exchange, electrodialysis, diffusion dialysis, electrophoresis
density	centrifugation
affinity	extraction, adsorption, absorption, reverse osmosis, gas separation, pervaporation, affinity chromatography
reactivity	complexation, carrier mediated transport

The membrane interphase can consist of a nonporous or porous solid, a porous solid with filled pores, or a liquid or gel, and transport through the membrane can take place under driving forces such as pressure, temperature, electrical potential, and concentration gradients.[4, 5]

For a specific separation, the applicability of a given membrane depends on its selectivity and permeability. High permeabilities are important for achieving a reasonable throughput at moderate driving forces, whereas high selectivities are vital for obtaining a pure product. In many cases, permeability and selectivity are inversely related, so optimization of a separation involves choosing the membrane material with the most economical combination of selectivity and permeability.

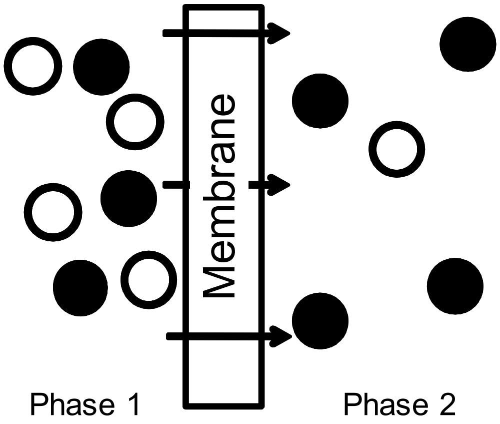

Figure 1.1: Schematic drawing of a membrane separating two phases.

Quantitative comparison of the energy and operating costs of membrane processes with the corresponding costs in other separation methods is sometimes difficult and often depends on the scale of the operation and the required purities. Generally, the advantages of membranes are low energy consumption, continuous operation, and a small footprint.[3] On a small scale, membranes are typically much easier to install than processes such as pressure swing adsorption.[6] In water desalination, the low energy requirements of reverse osmosis make it more attractive than distillation. However, the drawbacks of membrane separations can include low selectivity, fouling, and concentration polarization.[3]

This dissertation focuses on developing new membrane materials that may overcome drawbacks in specific membrane separations, including low selectivity in CO_2 removal from H_2 streams (chapters 2 and 3) and membrane biofouling in water purification (Chapter 4). To put this work in perspective, this introduction provides an overview of membrane theory and methods of transport. The solution diffusion model is discussed as well as permeation though porous membranes. That section is followed by a discussion of non-ideal permeation highlighting polarization and fouling, followed by membrane synthesis.

Classification of Membranes Processes

Depending on their pore sizes, membranes can separate a wide range of species, and Figure 1.2 shows the standard classifications of membrane separations along with the corresponding diameters of the retained species. Figure 1.3 illustrates how the mode of permeation varies with both the membrane pore size and the diameter of the species passing through the membrane. There are essentially four mechanisms of transport through a membrane: solution-diffusion, molecular sieving, Knudsen flow, and Poiseuille flow.

The research presented here focuses on dense, nonporous membranes as well as nanofiltration membranes. Nanofiltration membranes represent the transition between porous media and dense polymers, and proposed transport models include both solution diffusion and molecular sieving.[7, 8] In contrast, permeation through dense, gas-separation polymers most likely occurs though a solution diffusion mechanism (see below), although in special cases facilitated transport may occur and provide very high selectivities. Because of the emphasis of this work on dense membranes, the following sections provide a detailed analysis of the solution diffusion model and much shorter descriptions of transport through porous membranes.

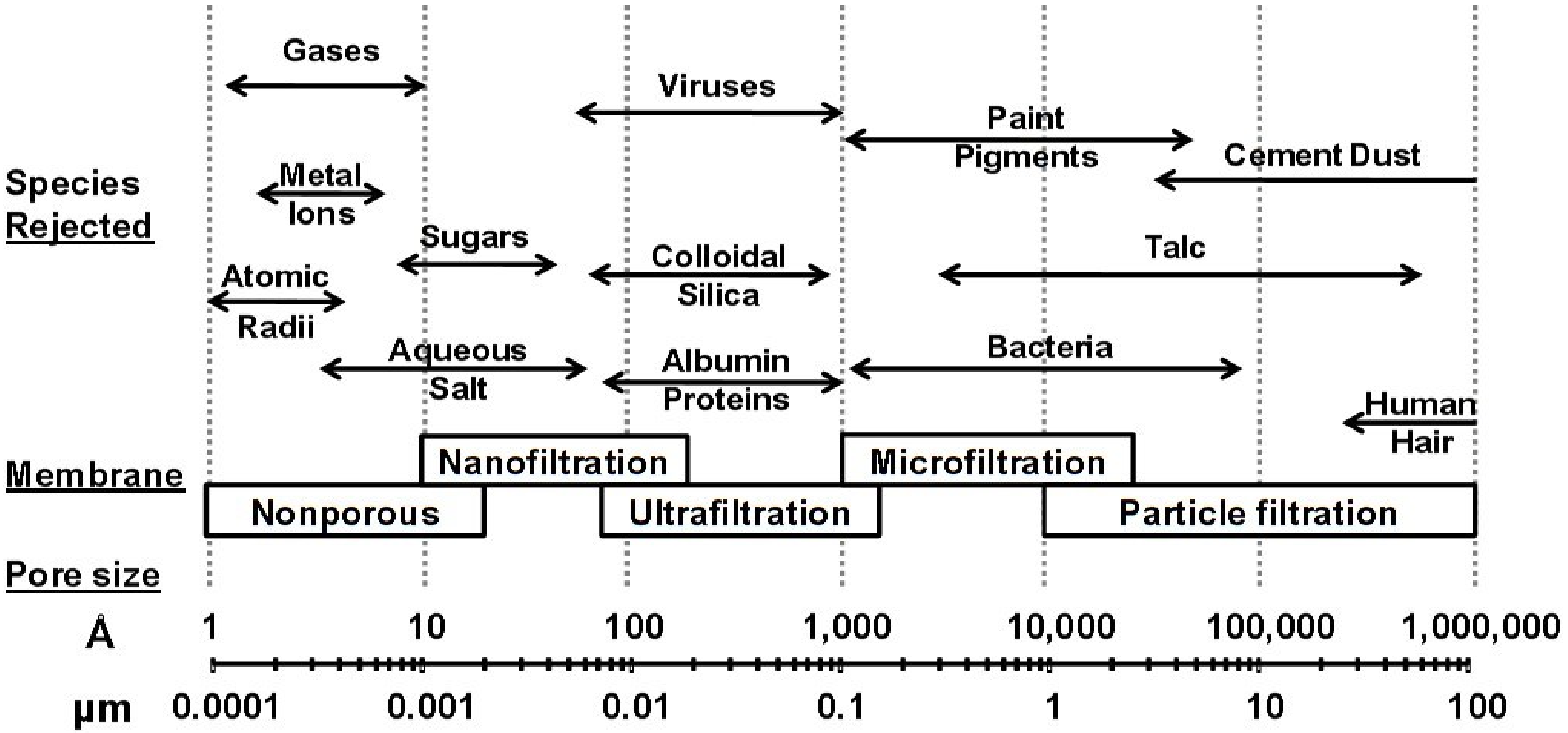

Figure 1.2: Classification of membrane processes according to the size of the species being rejected. Adapted from reference 9.

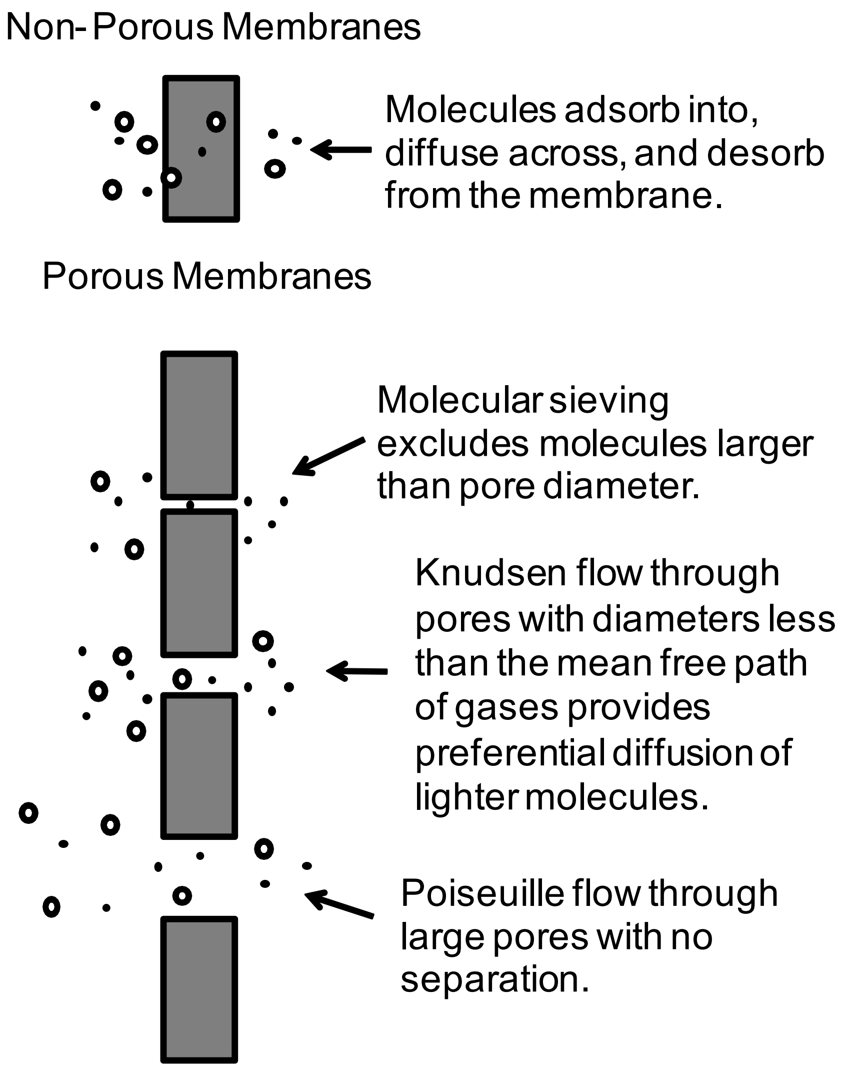

Figure 1.3: Schematic diagram of different types of transport through porous and non-porous membranes. Adapted from Ho and Sirkar.[4]

Solution-diffusion permeation through dense membranes

RO and membrane-based gas separations typically employ dense membranes to achieve selective transport of specific ions or small molecules such as water and gases. The development of increasingly selective polymeric membranes for gas separation accompanied advances in the theory of gas transport, and the table below shows a few historical highlights that lead to our current understanding of gas separation membranes, described below.

Table 1.2: Selected milestones in understanding gas separations. Modified from reference 5.

Event	Investigator	Year
First gas separation recorded	Graham	1829
Law of mass diffusion	Fick	1855
Permeability coefficient defined	von Wroblewski	1879
Knudsen diffusion defined	Knudsen	1908
Time-lag method to determine coefficients developed	Daynes	1920
Permeability and diffusivity models developed	Barrer	1939
Independent arrival at dual-mode sorption concept	Barrer, Barrie, and Slater	1958

In the solution-diffusion model for both liquid and gas separations, the permeation process involves dissolution of the transporting species into the membrane, diffusion across the membrane, and transfer into the receiving phase from the permeate face of the membrane (Figure 1.4). The amount of a species that flows through a given area of a membrane over a given time period is termed the flux, J, which has typical units of (mol m^{-2} s^{-1}) or (m^3 m^{-2} s^{-1}). In the absence of convection and migration, flux occurs by diffusion and follows Fick's first law, which is shown in Eq. (1.1) for a one-dimensional concentration gradient, $\frac{dc}{dx}$, and a diffusion coefficient, D.

$$J = -D\frac{dc}{dx} \tag{1.1}$$

The assumptions of a constant diffusion coefficient across a membrane of thickness, l, along with steady state flux lead to Eq. (1.2),

$$J_A = \frac{D_A(c_{2,A} - c_{3,A})}{l} \tag{1.2}$$

where $c_{2,A}$ is the concentration of A just inside the feed face of the membrane and $c_{3,A}$ is the concentration of A just inside the permeate face of the membrane. If the feed and permeate faces of the membrane are in equilibrium with the feed and permeate solutions, respectively, a partition coefficient K_A, Eq. (1.3), describes the ratio of the concentrations in the faces of the membrane and the neighboring solutions. (See Figure 1.4 for the definition of the symbols).

$$K_A = \frac{c_{2,A}}{c_{1,A}} = \frac{c_{4,A}}{c_{3,A}} \tag{1.3}$$

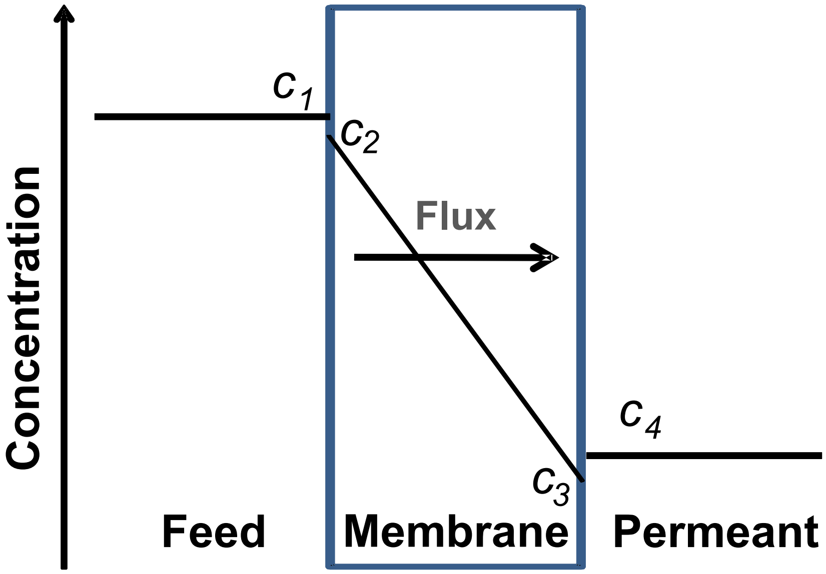

Figure 1.4: Concentration profile of an analyte during solution-diffusion through a membrane, where c_1, c_2, c_3, and c_4 represent the concentrations of the analyte in the feed, upstream face of the membrane, downstream face of the membrane, and permeate, respectively. (This diagram neglects concentration polarization, which is discussed below.)

Combining Eq. (1.3) and Eq. (1.2) yields Eq. (1.4), where P_A, the product of the diffusion and partition coefficients, is the permeability for species A.

$$J_A = \frac{D_A K_A (c_{1,A} - c_{4,A})}{l} = \frac{P_A (c_{1,A} - c_{4,A})}{l} \tag{1.4}$$

This expression shows that increases in diffusion and partition coefficients, increases in concentration gradients, and smaller membrane thicknesses all lead to higher fluxes.

Eq. (1.5) defines the selectivity ($\alpha_{\frac{A}{B}}$) of membrane separations, and in the ideal case where the permeate concentration is negligible compared to the feed concentration, this selectivity is also equivalent to the ratio of the permeabilities of components *A* and *B*.

$$\alpha_{\frac{\mathrm{A}}{\mathrm{B}}} = \frac{c_{4,\mathrm{A}} / c_{4,\mathrm{B}}}{c_{1,\mathrm{A}} / c_{1,\mathrm{B}}} \tag{1.5}$$

However, when the permeate concentrations are not negligible, Eq. (1.6) provides a more general expression for the ratio of the permeability coefficients.

$$\frac{c_{4,\mathrm{A}} / c_{4,\mathrm{B}}}{(c_{1,\mathrm{A}} - c_{4,\mathrm{A}}) / (c_{1,\mathrm{B}} - c_{4,\mathrm{B}})} = \frac{P_A}{P_B} \tag{1.6}$$

In the case of gas separations Henry's law, Eq. (1.7), often replaces the partition coefficient expression in Eq. (1.3) to afford a description of flux as a function of feed and permeate vapor pressures. Figure (1.5) describes the specific symbols in Henry's law.

$$\begin{aligned} c_{2,\mathrm{A}} &= S_{\mathrm{A}} p_{1,\mathrm{A}} \\ c_{3,\mathrm{A}} &= S_{\mathrm{A}} p_{4,\mathrm{A}} \end{aligned} \tag{1.7}$$

Substitution of Eq. (1.7) into Eq. (1.2) yields

$$J_A = \frac{D_A S_A (p_{1,A} - p_{4,A})}{l} = \frac{P_A (p_{1,A} - p_{4,A})}{l} \tag{1.8}$$

where the permeability is a product of the diffusion coefficient, D_A, and the Henry's law solubility constant, S_A, as shown in Eq. (1.9).

$$P_A = S_A \times D_A \qquad (1.9)$$

The solubility is a thermodynamic quantity that depends on the interaction of the gas molecule with the membrane polymer, whereas the diffusion coefficient reflects the kinetics of gas movement through the polymer. An increase in the intermolecular interactions between the penetrant and the membrane causes an increase in solubility and, hence, an increase in permeability. Similarly, an increase in diffusivity due to greater free volume in the polymer also causes an increase in permeability. In the case of Eq. (1.9), permeability has SI units of ($m^3 \times m \times m^{-2} \times s^{-1} \times Pa^{-1}$), but the most common engineering unit for P is the Barrer (10^{-10} $cm^3 \times cm \times cm^{-2} \times s^{-1} \times cmHg^{-1}$).

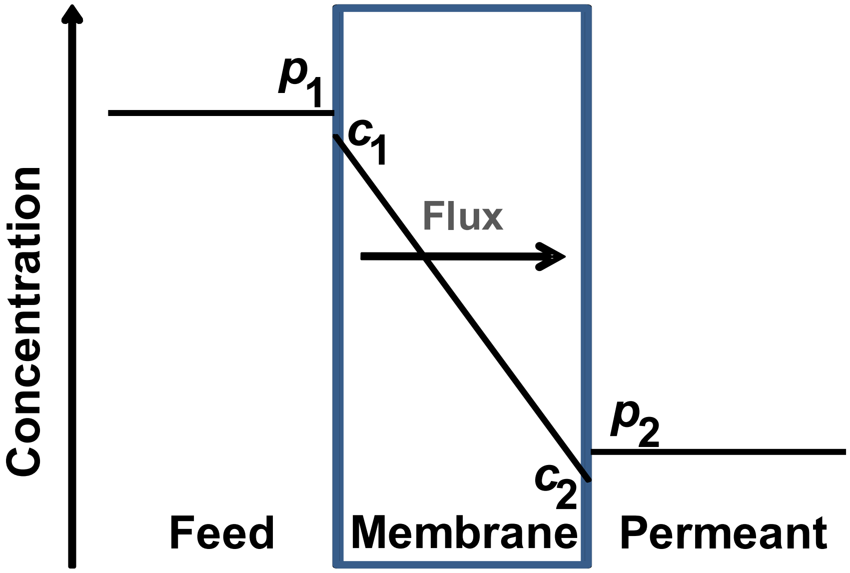

Figure 1.5: Concentration profile of a penetrant gas in a membrane from c_1 at the feed face to c_2 at the permeant face. The partial pressure levels are shown for the feed (p_1) and permeant (p_2) gas.

Eq. (1.10) defines the ideal selectivity (negligible permeant partial pressure) for gas molecule (A) over (B) where

$$\alpha_{A/B} = \frac{P_A}{P_B} = \frac{S_A \times D_A}{S_B \times D_B} \qquad (1.10)$$

the ratio of permeabilities is the product of solubility selectivity $\left(\frac{S_A}{S_B}\right)$ and diffusivity selectivity $\left(\frac{D_A}{D_B}\right)$. By convention component *A* is the more permeable species. There are three possible causes for a given selectivity, $\alpha_{\frac{A}{B}}$,: 1) *A* has a larger diffusivity, 2) *A* has a larger solubility, or 3) *A* has both a larger solubility and diffusivity. Table 1.3 presents these scenarios for several different gas separations.

Table 1.3: The three possible combinations of solubility and diffusivities that lead to selective gas transport, along with gas separations that employ these scenarios. Adapted from Pinnau and Freeman.[10]

Scenario	Examples	Membrane type
$S_B > S_A$, $D_A >> D_B$	H_2/N_2, H_2/CO, H_2/CH_4	size sieving/size selective
$S_A >> S_B$, $D_B > D_A$	CO_2/H_2, H_2S/H_2	reverse selective
$S_A \geq S_B$, $D_A \geq D_B$	O_2/N_2, H_2O/Air, CO_2/CH_4, H_2S/CH_4, CO_2/N_2	either size selective or reverse selective

The diffusivity selectivity-dominated scenario, row 1 in Table 1.3, employs traditional size-selective membranes to achieve a higher permeability of gas A than gas B, as shown in Figure 1.6. Diffusivity selectivity nearly always favors the smaller gas. In contrast, the solubility selectivity-dominated case, row 2 in Table 1.3, uses a "reverse selective" membrane to allow passage of the larger of two gases (Figure 1.7). The third scenario, row 3 in Table 1.3, represents a very desirable situation where both solubility and diffusivity selectivity favor the overall selectivity.

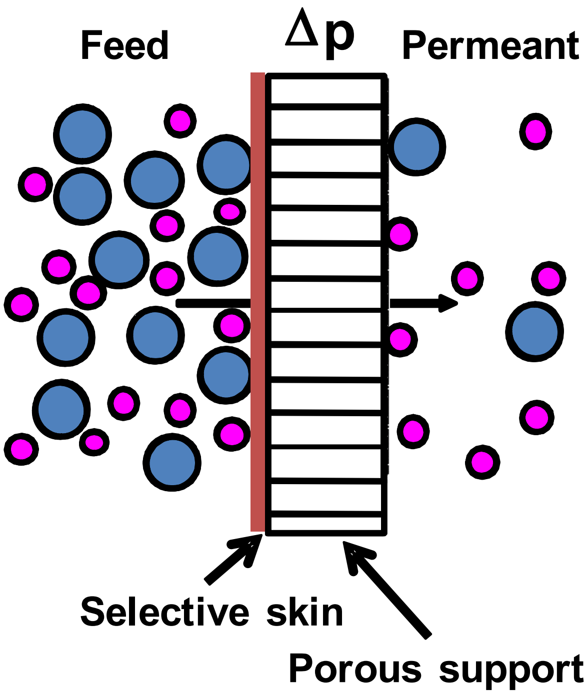

Figure 1.6: Schematic diagram of a size-selective separation with a composite membrane. The membrane has higher permeability for the smaller molecules due to diffusivity selectivity or molecular sieving. The low pressure side (right) of the membrane contains a higher fraction of small molecules than the feed side.

.

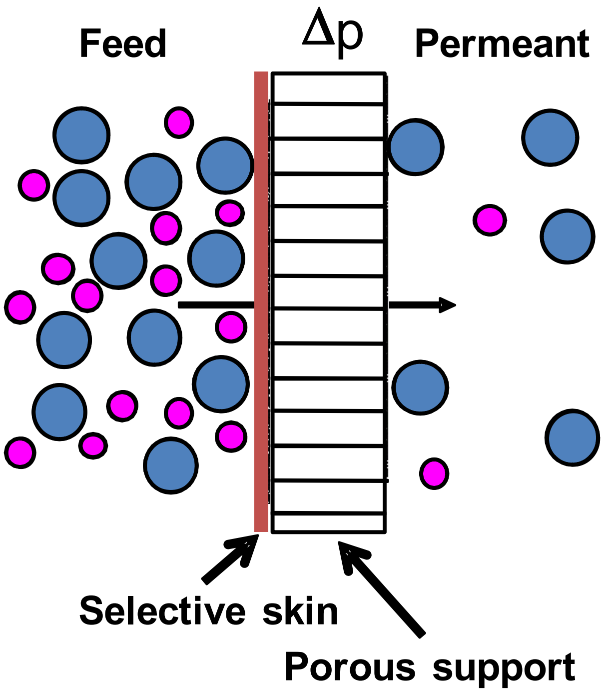

Figure 1.7: Schematic diagram of reverse selectivity. In this case, the membrane has higher permeability for larger molecules due to solubility selectivity. The lower pressure permeate side (right) of the membrane contains a higher fraction of the larger molecules than the feed side.

As an example of different selectivity mechanisms, CO_2/CH_4 separations can utilize both diffusivity and solubility selectivity. Cellulose acetate membranes exhibit CO_2/CH_4 selectivities of 20-30 in natural gas purification primarily because of the high solubility of CO_2 in cellulose acetate.[11] In contrast, the high diffusivity selectivity of glassy polyimide membranes provides the same separation with a remarkable overall CO_2/CH_4 selectivity of about 90.[12] The high diffusivity selectivity of the polyimide membranes exploites a size difference of only 0.5 Å (Table 1.4). In fact, Table 1.4 shows that a size range of 2.6 to 3.8 Å covers many common gases.

Typically, glassy polymers are effective in size-selective separations, whereas rubbery polymers may show reverse selectivity. Glassy polymers have an “unrelaxed” volume (Figure 1.8) that stems from polymer chains trapped in nonequilibrium conformations upon quenching below T_g. This “unrelaxed” volume leads to two types of sorption: Henry’s law adsorption in areas of dense polymer (similar to adsorption in rubbery polymers) and Langmuir adsorption in the “holes” between the polymer chains.

Table 1.4: Kinetic diameters[a] and critical temperatures of various gases.[13]

Molecule	Kinetic Diameter[a] (Å)	Critical Temperature (°C)
He	2.6	-268
H_2	2.89	-240
CO_2	3.3	31
O_2	3.46	-119
N_2	3.64	-147
CO	3.76	-140
CH_4	3.8	-82

[a] The Kinetic diameter is the minimum zeolite window diameter that permits sorption.

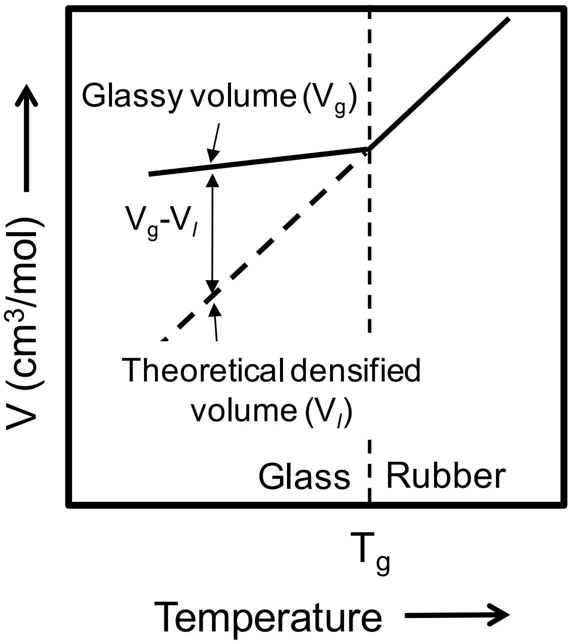

Figure 1.8: Polymer volume relative to temperature. Modified from Zolandz and Fleming.[14]

Thus, Eq. (1.11) describes the total concentration, c, of adsorbed gas as the sum of

$$c = c_D + c_H \tag{1.11}$$

the sorbed concentration in dense regions of the polymer, c_D, and the sorbed concentration in holes, c_H, between the dense regions.[14] The concentration in the dense region follows Henry's law, Eq. (1.7), and the concentration of adsorbed gas in preexisting holes follows the Langmuir isotherm in Eq. (1.12) [14]

$$c_H = \frac{c'_H bp}{1 + bp} \tag{1.12}$$

where c'_H is the capacity constant, b is the ratio of the rate constants for adsorption and desorption, and p is the pressure of a single gas. This additional sorption mode results in glassy polymers typically possessing higher permeabilities than rubbery polymers.[10] (The main exception is poly(dimethyl siloxane), which is a rubbery polymer with a CO_2 permeability over 3,000 Barrer.)

One important consideration when using glassy polymer membranes that rely on diffusivity selectivity is whether extensive sorption of a condensable gas such as CO_2 will plasticize the membrane and alter the selectivity. For example, in poly(vinyl chloride), a highly selective glassy polymer, the diffusivities of gases with critical volumes ranging from 65 – 370 cm^3/mol (hydrogen to *n*-hexane) vary by ten orders of magnitude.[15, 16] However, in plasticized poly(vinyl chloride) membranes, the same molecules have diffusivities that vary by only two orders of magnitude.[15]

Penetrant Solubility

Gas condensability, as reflected by critical temperatures, strongly correlates with penetrant solubility in gas separations. Low critical temperatures indicate strong intermolecular interactions among gas molecules, and such gases also interact strongly with polymers. Several studies suggest that at a given temperature the solubilities of different gases in a particular polymer vary logarithmically with the critical temperature (T_c) of the gas according to Eq. (1.13),[17, 18]

$$\ln S = M + NT_c \tag{1.13}$$

where M and N are constants. Table 1.4 shows that the critical temperatures of common gases vary tremendously, from -268 to 31°C, and solubility selectivity can easily reach values of 100.[19] More recently, Freeman and coworkers presented data indicating that the logarithm of solubility is proportional to the square of the critical temperature, shown in Eq. (1.14).[20-22] They suggested that solubility is influenced by both entropy and enthalpy

$$\ln S_A = M + N\left(T_c\right)^2 \tag{1.14}$$

which causes a deviation from the linear behavior in Eq. (1.13).[23] Larger penetrant species require larger cavities, which leads to an entropic penalty opposing solubility. However, polymer-penetrant interactions are stronger for larger species, so enthalpy changes favor the solubility of larger gases. These conflicting contributions may explain why trends in solubility for certain gases follow Eq. (1.13), whereas other groups of gases follow Eq. (1.14).

The solubility can be expressed in terms of the energy required to transfer one mole of penetrant gas from the bulk gas phase into the membrane according to Eq. (1.15)[23]

$$S = \frac{T_0}{TP_0}\exp[-\Delta G_M / RT] \tag{1.15}$$

where S is solubility, T_0 is 273.15 K, T is the temperature, P_0 is 1 atm, and ΔG_M is the Gibbs' free energy of mixing. The following section examines the thermodynamic parameters that give rise to the Gibbs' free energy of mixing and influence the solubility of a penetrant in a polymer.

Once a penetrant approaches a membrane surface, the probability of dissolution into the membrane matrix depends on the Gibbs free energy of mixing (G_M). Mixing spontaneously occurs when the change in energy is negative ($\Delta G_M \leq 0$). For the mixing reaction $A + B \rightarrow AB$ the change in Gibbs free energy is

$$\Delta G_M = G_{AB} - (G_A + G_B) \tag{1.16}$$

where G_{AB} is the Gibbs free energy of the mixture of *A* and *B*, and G_A and G_B are the Gibbs free energies of pure *A* and pure *B*, respectively. Of course the Gibbs free energy, has both enthalpic and entropic contribution as shown in Eq. (1.17),

$$\Delta G_M = \Delta H_M - T\Delta S_M \tag{1.17}$$

where H_M is the enthalpy of mixing, T is temperature, and S_M is the entropy of mixing. The entropy change upon mixing is not ideal due to the different sizes of polymer and solvent molecules, as well as chain connectivity. The most accurate derivation of the entropy of mixing considers all distinguishable spatial arrangements of the penetrant and polymer molecules. Boltzmann's equation, Eq. (1.18)[24]

$$\Delta S_{mix} = k \ln\left(\frac{\Omega_{AB}}{\Omega_B}\right) \tag{1.18}$$

considers a lattice model which relates the entropy to the number of distinguishable arrangements of pure polymer molecules (Ω_B) and mixture of penetrant and polymer molecules (Ω_{AB}) in the lattice, where k is Boltzmann's constant. The expression for Ω_{AB} is a continuous product of all possible conformations of polymer molecules, and the expression has been simplified by Flory to yield the following Eq. (1.19)[24]

$$\Delta S_M = -k[N_1 \ln \phi_1 + N_2 \ln \phi_2] \tag{1.19}$$

where k is Boltzmann's constant, N_A and N_B are the number of solvent species A and polymer species B respectively, and ϕ_A and ϕ_B are the volume fraction of component A and B, respectively. The volume fraction is given by the fraction of lattice points occupied, Eq. (1.20)

$$\begin{aligned} \phi_A &= \frac{N_A}{\left(N_A + \sigma N_B\right)} \\ \phi_B &= \frac{\sigma N_B}{\left(N_A + \sigma N_B\right)} \end{aligned} \tag{1.20}$$

Where N_B polymer molecules contain σ segments in the polymer chain. This assumes that each segment, σ, is equal in size to a penetrant molecule. Eq. (1.19) can be rewritten in terms of moles, n, as shown in Eq. (1.21)[24]

$$\Delta S_{mix} = -R[n_A \ln \phi_A + n_B \ln \phi_B] \tag{1.21}$$

Having derived an expression for entropy, the second stage is to derive an expression for enthalpy. The enthalpy of pure gases is shown in Eq. (1.22)

$$\begin{aligned} H_{AA} &= \frac{zN_A\omega_{AA}}{2} \\ H_{BB} &= \frac{zN_B\omega_{BB}}{2} \end{aligned} \tag{1.22}$$

where *H_{AA}* and *H_{BB}* are the enthalpies of pure *A* and pure *B*, respectively, z is the coordination number, N is the number of molecules, and ω_{AA} and ω_{BB} are the interaction energy between two A molecules and two B molecules, respectively. The 2 accounts for the fact that one interaction involves two species. The enthalpy for species A adjacent to species B is

$$H_{AB} = N_{AB}\omega_{AB} + \frac{(zN_A - N_{AB})\omega_{AA}}{2} + \frac{(zN_B - N_{AB})\omega_{BB}}{2} \tag{1.23}$$

where *H_{AB}* is the enthalpy of an *AB* mixture and ω_{AB} is the interaction energy between A and B. To calculate the enthalpy of mixing, Eq. (1.22)and (1.23) are inserted into Eq. (1.24),

$$\Delta H_{mix} = H_{AB} - H_{AA} - H_{BB} \tag{1.24}$$

which gives the difference in the enthalpy of the products and reactants to generate Eq. (1.25)

$$\Delta H_{mix} = N_{AB}\omega_{AB} + \frac{(zN_A - N_{AB})\omega_{AA}}{2} + \frac{(zN_B - N_{AB})\omega_{BB}}{2} - \frac{zN_A\omega_{AA}}{2} - \frac{zN_B\omega_{BB}}{2} \tag{1.25}$$

Simplification of Eq. (1.25) yields the following enthalpy of mixing,

$$\Delta H_{mix} = N_{AB}[\omega_{AB} - \frac{\omega_{AA} + \omega_{BB}}{2}] = N_{AB}\Delta\omega_{AB} \tag{1.26}$$

which states that the enthalpy of mixing is the number of interaction sites multiplied by the mixture interaction energy less the pure-substance interaction energy. The number of interaction sites N_{AB} is approximated below

$$N_{AB} = zN_A x_B \tag{1.27}$$

By multiplying the interaction sites around an A molecule (z), the number of A molecules (N_A), and the mole fraction of B molecules (x_B).

Having shown the enthalpy and entropy, substitution of Eq. (1.26) and Eq. (1.21) into Eq. (1.17) yields the expression for the Gibbs free energy of mixing in Eq. (1.28).

$$\Delta G_{mix} = RT[n_A \ln x_A + n_B \ln x_B + \tfrac{zn_A N_{Avo} x_B \Delta\omega_{AB}}{RT}] \tag{1.28}$$

This is usually rewritten in terms of the Flory-Huggins interaction parameter, χ, as defined below.

$$\chi_{AB} = \tfrac{zN_{Avo}\Delta\omega_{AB}}{RT} = \tfrac{z\Delta\omega_{AB}}{kT} \tag{1.29}$$

It follows from Eq. (1.29) that χ is a dimensionless ratio of interaction energy of the polymer with the penetrant to the kinetic energy RT. Now ΔG_{mix} is rewritten as Eq. (1.30).

$$\Delta G_{mix} = RT[n_A \ln x_A + n_B \ln x_B + n_A x_B \chi_{AB}] \tag{1.30}$$

This interaction parameter, χ, has the physical meaning of a measure of the affinity of a polymer for a penetrant.

The Flory-Huggins interaction parameter of the penetrant is useful in the selection of membrane materials for specific separations. Of particular relevance to this dissertation, the CO_2 interaction parameter provides some of the rationale for the selection of the CO_2-selective membrane materials described in chapters 2 and 3. Several studies determined CO_2 interaction parameters with different polymers, but there are substantial discrepancies in the reported χ values. The interaction parameter for a penetrant is usually determined by dissolving the penetrant in a series of solvents with known solubility parameters and plotting the solubility against these solvent parameters to find a maximum. The solubility parameters for liquids are defined as $\delta = \sqrt{(\Delta H_{vap} - RT)/V}$ where ΔH_{vap} is the enthalpy of vaporization and V is the molar volume at 25 °C. This definition is not valid near the critical temperature and therefore not appropriate for CO_2 near room temperature. Lawson and coworkers estimated the CO_2 interaction parameter to be 6.8 $MPa^{0.5}$ by separately measuring the solubility of CO_2 in a range of solvents with solubility parameters ranging from 12 to 20 $MPa^{0.5}$ and finding the maximum on a plot of solubility vs. solubility parameter.[25] This value of the interaction parameter is less than that of H_2 and N_2, which is counterintuitive given that CO_2 contains a quadrupole moment. In a different study, the CO_2 interaction parameter obtained by dissolving CO_2 in toluene was 12.2 $MPa^{0.5}$.[26] Two studies in 2005 from Benny Freeman *et al.* reported a χ value of 26.8 $MPa^{0.5}$ for CO_2 in cross-linked poly(ethyleneglycol)diacrylate from temperature studies,[27] and 21.8 $MPa^{0.5}$ from dissolving CO_2 in organic solvents with solubility parameters ranging from 15 to 30 $MPa^{0.5}$.[19] An accurate determination of the CO_2 solubility parameter is necessary to determine a membrane material with maximum CO_2 solubility.

Fractional free volume of the polymer also correlates with permeability because increases in free volume sometimes lead to higher solubilities and diffusivities. Introduction of side chains that disrupt polymer packing typically increases free volume and enhances permeability. For example, Benny Freeman introduced phenyl groups to disrupt chain packing of rigid polyamides and increased the fractional free volume by up to 7 %.[28] Additionally, cross-linking increases fractional free volume in PEG-based membranes, causing a modest CO_2 solubility increase from

1.3 cm^3(STP)/(cm^3atm) in amorphous PEO to 1.4 cm^3(STP)/(cm^3atm) in crosslinked PEO-diacrylates.[27] However, the major achievement of crosslinking is the prevention of PEO crystallization. Crystalline PEO has a very low fractional free volume and a CO_2 solubility of only 0.4 cm^3(STP)/(cm^3atm). Additionally, permeability can decrease with decreasing fractional free volume. Permeability decreased by a factor of three through decreases of fractional free volume by nitrating polysulfone membranes.[29]

Permeation through porous membranes

Permeation through a porous membrane occurs through either Knudsen diffusion or Poiseuille flow. In Knudsen diffusion, collisions of molecules with the pore walls control the rate of transport, whereas in Poiseuille flow the channel is large enough that laminar flow occurs. The relative contributions of these two transport mechanisms depend on the pore radius and the mean free path of the permeant (Figure 1.4). Specifically, when the ratio of the pore radius (r) to the mean free path (λ) is much less than one, Knudsen flow occurs; when r/λ is approximately two, the Knudsen and Poiseuille flows contribute equally to transport; and when r/λ is much larger than one, Poiseuille flow occurs (r/λ of 5 is >90% Pouiseuille flow).[5] Eq. (1.31) provides an expression for the mean free path, λ, of a gas as a function of

$$\lambda=\frac{3\eta}{2P}\sqrt{\frac{\pi RT}{2M}} \tag{1.31}$$

the molecular mass (M), pressure (P), viscosity (η), and temperature (T) of the permeating species, where R is the gas constant. At atmospheric pressure, the mean free path of gases is around 100-200 nm,[5] so if the membrane pore diameter is less than 50 nm, transport occurs primarily due to Knudsen flow.

The frequency of collisions between a gas and the pore wall varies with the molecular velocity, $\bar{u}$, which is a function of the gas molecular mass (Eq. 1.32).

$$\bar{u}=\sqrt{\frac{8RT}{\pi M}} \tag{1.32}$$

Eq. (1.33) describes Knudsen's diffusion coefficient, D_K,[5]

$$D_K = \frac{\bar{u}}{4\pi}\int_0^r\int_0^{2\pi}\int_{-\infty}^{\infty}\frac{x^2dx}{(s^2+x^2)^2}s^2d\beta ds / \int dS \tag{1.33}$$

in an infinitely long pore with radius r, where the position S is at a distance x along the pore, that is a distance s away from the pore wall at an angle (β) from the pore wall. Integration of Eq. (1.33) yields Eq. (1.34),[5]

$$D_K = \frac{2\bar{u}r}{3} \tag{1.34}$$

And substitution of Eq. (1.32) into Eq. (1.34) yields the final expression for D_K.

$$D_K = \frac{4r}{3}\sqrt{\frac{2RT}{\pi M}} \tag{1.35}$$

Eq. (1.35) is valid for a single cylindrical pore, but most membranes contain an assembly of pores that may offer a tortuous path through the membrane. In this case, Eq (1.36) describes the effective Knudsen diffusion coefficient,

$$D_K = \frac{4r\varepsilon}{3\tau}\sqrt{\frac{2RT}{\pi M}} \tag{1.36}$$

where ε is porosity and τ is tortuosity. Porosity, the fraction of the membrane volume occupied by pores, ranges from 0 to 1, whereas tortuosity is greater than 1. Unfortunately, tortuosity is difficult to calculate in complex membranes and frequently serves as a correction factor.

The combination of the Knudsen diffusion coefficient [Eq. (1.36)] and Fick's law [Eq. (1.1)] leads to Eq. (1.37), an expression for flux through the membrane

$$J = \frac{4r\varepsilon}{3\tau}\sqrt{\frac{2RT}{\pi M}}\left(\frac{n_0}{V} - \frac{n_1}{V}\right)\frac{1}{l} \tag{1.37}$$

where $\frac{n_0}{V}$ is the moles of gas per volume at the feed end of the pore and $\frac{n_1}{V}$ is the moles per volume at the permeate end of the pore. Using the ideal gas law, $pV = nRT$, Eq. (1.38) expresses flux

$$J = \frac{4r\varepsilon}{3\tau}\sqrt{\frac{2RT}{\pi M}}\,\frac{p_0 - p_1}{lRT} \tag{1.38}$$

in terms of the partial pressure at the feed side of the pore, p_o, and at the permeate side of the pore, p_1. Application of this equation to calculate the ideal selectivity for one gas over another, results in the cancellation of all variables except molecular mass, so selectivity is simply inversely proportional to the square root of molecular masses, Eq. (1.39).

$$\alpha_{\frac{A}{B}} = \sqrt{\frac{M_B}{M_A}} \tag{1.39}$$

Knudsen selectivity is relatively low, particularly, if H_2, which has the lowest mass of any gas, is not one of the gases. Even in this case, the Knudsen selectivity for H_2/CO_2 is only 4.7.

As the the ratio of r/λ becomes much larger than one, Poiseuille flow dominates transport, and Eq. (1.40) describes the total volume flux through the membrane.

$$J = \frac{r^2\left(P_0 - P_1\right)\left(P_0 + P_1\right)}{8\eta lRT} = \frac{r^2\left(P_0^2 - P_1^2\right)}{8\eta lRT} \tag{1.40}$$

In Poiseuille flow, separation of molecules no longer occurs because they interact with each other more than with the pore walls.

In the application of all selective membranes, whether porous or nonporous, there are several complications that cause deviations from ideality. Below I describe the most common complications, concentration polarization and fouling.

Non-Ideal Membrane Performance

In most membrane separations, particularly those that employ liquids, selectivity and flux decline with time. The pressure-driven convective flux can be written as[3]

$$J = \frac{\Delta p}{\eta R_{tot}} \tag{1.41}$$

where η is the viscosity and R_{tot} is the total resistance to mass transport. The value of R_{tot} is the sum in Eq. (1.42)

$$\mathrm{R_{tot}} = \mathrm{R_m} + \mathrm{R_c} + \mathrm{R_b} + \mathrm{R_{cp}} + \mathrm{R_a} \tag{1.42}$$

the ideal membrane resistance (R_m), and the non-ideal resistances due to cake layer formation (R_c), pore-blocking (R_b), concentration polarization (R_{cp}), and adsorption (R_a).[3] Figure 1.9 schematically shows the origin of these resistances, and a membrane system could contain any combination of these resistance types. Cake layer formation typically occurs with proteins, or other solutes such as colloids, that form gels at increased concentrations. In porous membranes a solute may physically block a pore and generate R_b or adsorb in a pore without complete blocking to give R_a. The next section discusses resistance due to the occurrence of concentration polarization, followed by the section which describes biofouling, or adsorption of microorganisms.

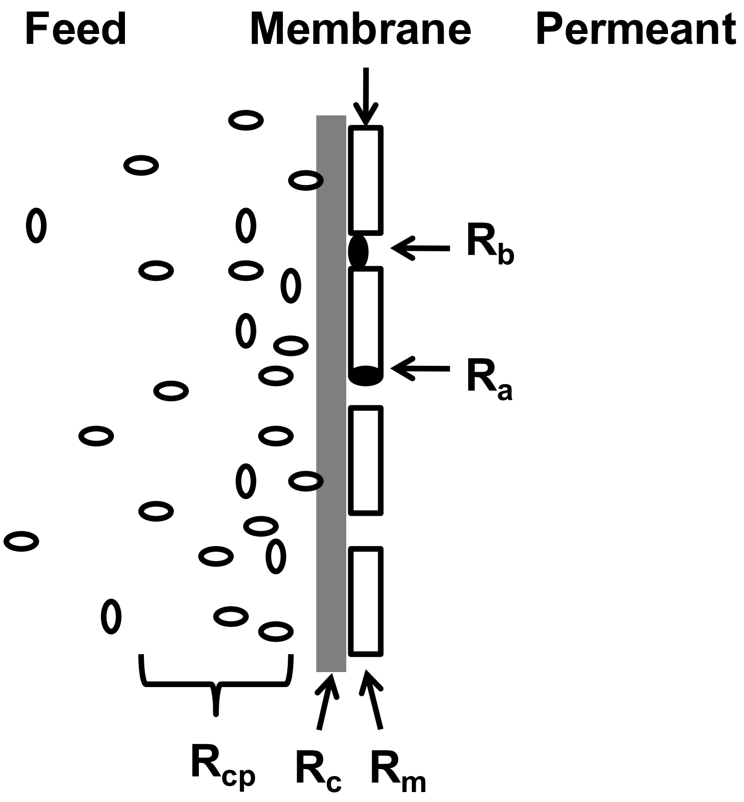

Figure 1.9: Overview of various phenomena that generate resistance to convective flux. The various resistances stem from the ideal membrane-R_m, cake layer formation-R_c, pore blocking-R_b, concentration polarization-R_{cp}, and adsorption-R_a.

Concentration Polarization. In many membrane separations, the accumulation of rejected species near the feed side of the membrane decreases both rejection and flux. This phenomenon, known as concentration polarization, is particularly problematic in liquid-based separations where diffusion coefficients are relatively low. In a typical membrane separation, convection moves all species toward the membrane where some of the species are rejected more than others.

During filtration, the concentrations of the rejected species at the membrane-feed interface initially increase until the flux due to permeation is equal to the sum of convective flux to the membrane and back diffusion from the membrane surface (Figure 1.10).

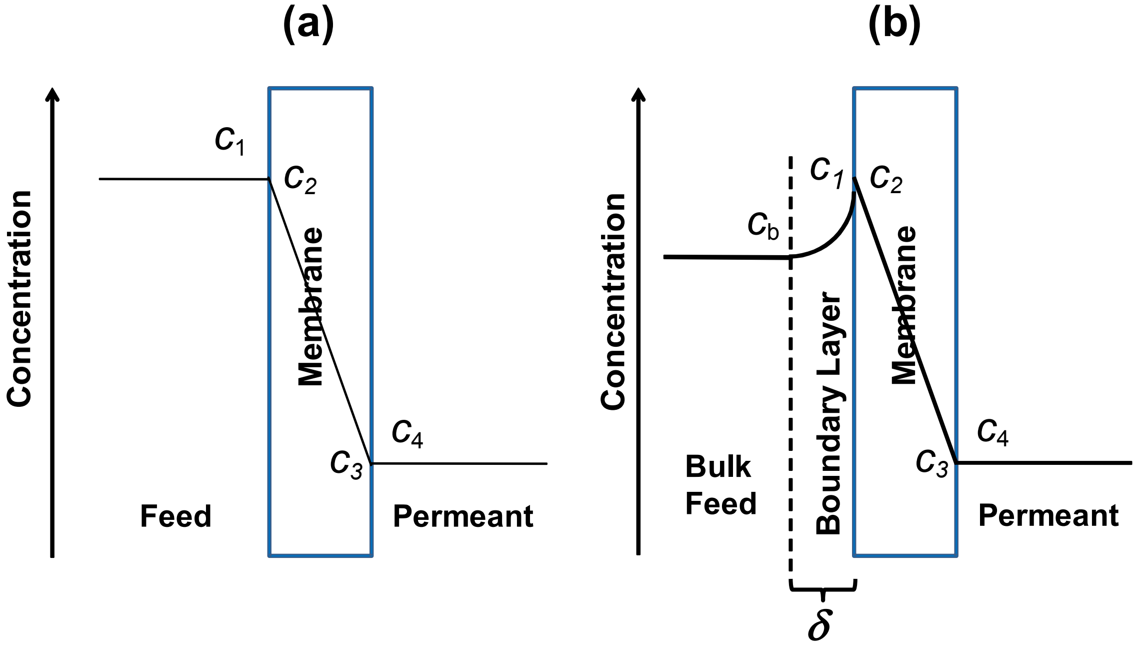

Figure 1.10: Simplified scheme of a concentration profile (a) under a concentration driven membrane separation with perfect mixing and (b) with concentration polarization at the feed interface under steady-state conditions. The concentration at c_1 does not necessarily equal c_2, and c_3 does not necessarily equal c_4. Note that in the case of concentration polarization the concentration begins to increase at a distance δ, along the x-axis, from the membrane surface.

Eq. (1.43) describes this mathematically

$$Jc - D\frac{dc}{dx} = Jc_4 \tag{1.43}$$

where J is the convective volume flow toward the membrane, c is the local concentration, $-D\frac{dc}{dx}$ is the diffusive backflow away from the feed face, and c_4 is the concentration in the permeate. The volume flux is assumed constant throughout the system. Integration of this equation over the stagnant layer thickness, δ, from $c=c_b$ to $c=c_1$ yields Eq. (1.44)

$$\ln\frac{c_1 - c_4}{c_b - c_4} = \frac{J\delta}{D} \tag{1.44}$$

where the ratio $\frac{D}{\delta}$ is often termed the mass transfer coefficient, k. (In fact, the mass-transfer coefficient is more general than $\frac{D}{\delta}$.) In the case of a theoretically perfect membrane where the solute is completely rejected by the membrane and the permeate concentration (c_4) is 0, Eq. (1.44) becomes

$$\frac{c_1}{c_b} = \exp\left(\frac{J}{k}\right) \tag{1.45}$$

This equation illustrates that the extent of concentration polarization depends on the solute diffusion coefficient and the hydrodynamic properties that determine k, as well as the flux, which varies with both pressure and the type of membrane. In general concentration polarization decreases rejection because of the high solute concentration at the surface.[3] (The consequences of concentration polarization can be quite complicated in certain applications, i.e. when retained macromolecules form a dynamic secondary membrane that increases rejection of lower molecular weight solutes.)[3] In the case of gas separations, the large diffusion coefficients of gases prevent significant concentration polarization, but microfiltration and ultrafiltration suffer large flux declines due to this phenomenon.

Partial remedies for concentration polarization include an increase in operating temperature or mixing near the surface to increase the mass transfer coefficient, k. A dead-end membrane module (Figure 1.11a) is the simplest separation design, but most membrane separations employ a cross-flow process (Figure 1.11b) to limit the thickness of the boundary layer and reduce concentration polarization. The cross-flow method generates both retentate and permeate streams, where the product can be either the concentrated solute in the retentate or the purified permeate.

Industrial applications typically utilize spiral wound modules or hollow fiber bundles to maximize the area of membrane per module volume.

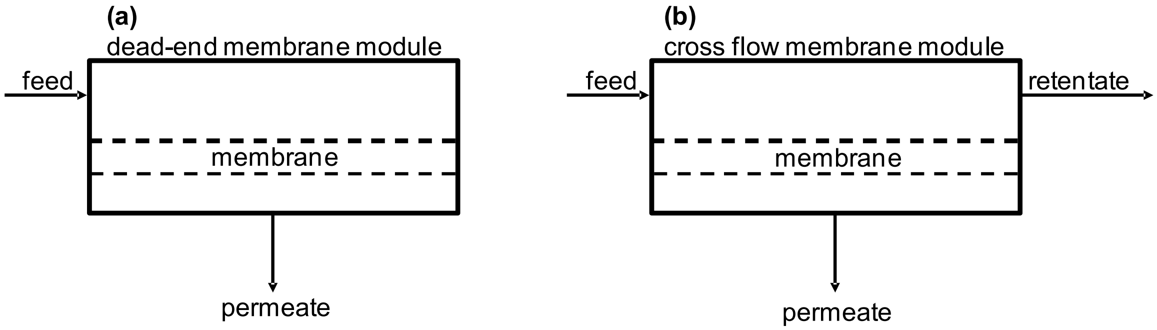

Figure 1.11: Schematic drawings of (a) a dead-end membrane and (b) a cross-flow membrane module. In the dead-end mode the concentrations of rejected species continually increase on the feed side of the membrane, whereas the cross-flow module allows for rejected species to flow along the membrane face and out of the module via the retentate path.

Biofouling. The decrease in membrane performance due to concentration polarization may reach a steady state, but fouling of leads to a continuous decline in flux (Figure 1.12). The two phenomena are often related, however, as the stagnant solution in the fouling layer may lead to increases in concentration polarization.

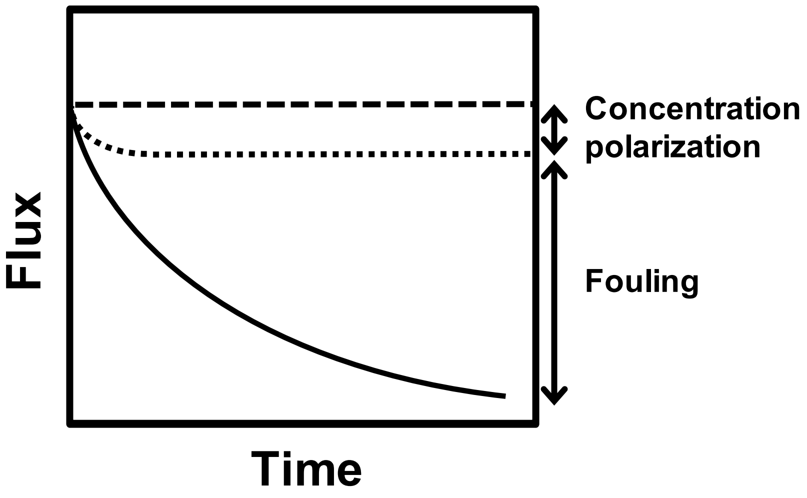

Figure 1.12: Decreases in transmembrane flux over time, due to concentration polarization and fouling.

Fouling mechanisms include cake or scale formation[3] and microorganism adsorption.[30] Fouling due to microorganisms, biofouling, is particularly problematic because bacteria multiply and cause significant decreases in membrane permeability.[30] Moreover, bacterial deposition of extracellular polysaccharides further decreases permeability and allows attachment of additional microorgranisms.[30] The initial step in biofouling, cell adhesion, depends on substrate properties such as roughness,[31-33] topography,[34] free energy,[35, 36] and polymer composition.[37-39] Methods to modify membranes to resist biofouling include incorporation of antibacterial metal particles,[40-42] and surface modification with ammonium groups.[43-47] Complementary methods to externally combat membrane fouling include pretreatment of the feed solution[48, 49] and intermittent membrane cleaning.[50, 51] Chapter 4 discusses our attempts to create antifouling membranes.

Synthesis of Selective, High-Flux Membranes

The inverse relationship between flux and thickness, Eq. (1.2), translates to lower operating pressures for thinner membranes, so commercial separation membranes consist of a thin, selective skin on a highly permeable porous support layer. The support provides mechanical strength, whereas the skin imparts selectivity while allowing a reasonable flux because of its small thickness. Methods for preparing such gas separation membranes with thin skins include casting,[52, 53] spin-coating,[54] spray-coating,[55, 56] phase-inversion,[57, 58] polyelectrolyte deposition,[59] interfacial polymerization,[60-62] and surface-initiated polymerization.[63] Surface-initiated polymerization, the main focus of this research, involves attachment of an initiator to a surface and subsequent polymerization from the immobilized initiator. The thickness of the membrane skin varies with polymerization time and can range from tens of nanometers to several microns. Initiator attachment typically occurs via reaction of a silane initiator with an oxide/oxidized surface or adsorption of a polyelectrolyte macroinitiator.[64] For research purposes, initiator layers can form through self assembly of thiol monolayers of initiators on Au-coated membranes.[65]

Growth of polymers from surfaces can occur via anionic,[66] cationic,[65, 67] free radical,[68-70] ring opening,[71] ring opening metathesis,[72-76] or controlled radical polymerization (CRP).[77-85] CRPs, which are discussed in a number of review articles[86, 87] and books,[88] include nitroxide mediated polymerization,[78-81] reversible addition fragmentation transfer,[82-84] and atom transfer radical polymerization (ATRP).[85] Surface-initiated ATRP is our preferred method of polymerization because it occurs at room temperature and provides minimal solution polymerization, control over thickness, and the ability to polymerize a wide range of functional polymers.

Atom transfer radical polymerization. Fig. 1.13, shows the reactions that constitute the ATRP mechanism. A number of transition metals including Ti,[89] Fe,[90-95] Co,[96] Ni,[97-99] Mo,[100-102] Ru,[103-107] Rh,[108, 109] Pd,[110] Re,[111] and Os,[112] can mediate ATRP, but Cu is the most common catalyst for this reaction.

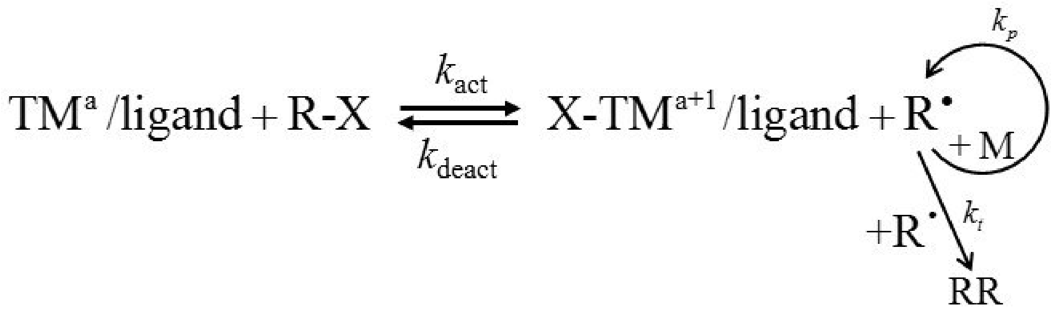

Figure 1.13: Reactions involved in ATRP. The ATRP mechanism contains an equilibrium where a dormant chain (R-X) activates at a rate of k_{act} to form a radical ($R^\bullet$) and deactivates at a rate of k_{deact} to return to the protected state. Transition metals (TM) at two different oxidation states ("a" and "a+1") complexed with ligand(s) mediate the process. The active radical reacts with monomer to form polymer with a rate constant of k_p or terminates with a neighboring radical with a rate constant of k_t.

The first step in the polymerization is transfer of a halide atom to the transition metal (TM) complex along with oxidation of the TM (Figure 1.13). The rate constant for the reverse reaction, k_{deact}, is much higher than the rate of activation, so growing chains are predominantly in the halogen-capped, dormant state. This decreases the rate of termination relative to polymerization because polymerization kinetics are first order with respect to radical concentration whereas termination is a second-order reaction. Minimal termination and the low radical concentrations lead to slow, controlled polymerization. In the case of Cu-mediated polymerization, Eq. (1.46) shows the equilibrium constant for the activation/deactivation reaction.

$$K_{ATRP} = \frac{k_{act}}{k_{deact}} = \frac{[Cu^{II}X/L][R^\bullet]}{[R\text{-}X][Cu^{I}/L]} \qquad (1.46)$$

Solving this equation for the radical concentration yields Eq. (1.47),

$$[R^\bullet]=K_{ATRP}[R\text{-}X]\left(\frac{[Cu^{I}/L]}{[Cu^{II}X/L]}\right) \qquad (1.47)$$

and substitution of the radical concentration into the polymerization rate equation yield the expression on the right of Eq. (1.48).

$$R_p = k_p[\mathrm{M}][\mathrm{R}^\bullet] = k_p[\mathrm{M}]\mathrm{K}_{\mathrm{ATRP}}[\mathrm{R\text{-}X}]\left(\frac{[\mathrm{Cu}^{\mathrm{I}}/\mathrm{L}]}{[\mathrm{Cu}^{\mathrm{II}}\mathrm{X}/\mathrm{L}]}\right) \qquad (1.48)$$

This expression shows that increasing the concentration of monomer or the Cu^{I} complex increases the rate of polymerization, whereas increasing the concentration of the $\mathrm{Cu}^{\mathrm{II}}$ complex should decrease the reaction rate and increase control over the polymerization.

Research Overview

The following chapters of this dissertation focus on developing new membrane materials that may enhance performance in existing separations, or increase applications of membranes for specific separations. Gas separations, including CO_2 removal from H_2 streams are performed in chapters 2 and 3 using surface-initiated atom transfer radical polymerization to generate thin poly(ethylene glycol)-based membranes. Chapter 4 focuses on the separation of ions using a membrane that resists biofouling in water purification.

REFERENCES

REFERENCES

(1) Favre, E. *J. Membr. Sci.* **2007,** 294, 50-59.

(2) Davison, J.; Thambimuthu, K. *Proc. Inst. Mech. Eng. A* **2009,** 223, 201-212.

(3) Mulder, M. *Basic Principles of Membrane Technology*. second ed.; Kluwer Academic Publishers: Boston, 1996.

(4) Ho, W. S. W.; Sirkar, K. K. Overview. In *Membrane Handbook*; Ho, W. S. W.; Sirkar, K. K., Eds.; Kluwer Academic Publishers: Norwell, MA, 1992; pp 1-25.

(5) Kesting, R. E.; Fritzsche, A. K. *Polymeric Gas Separation Membranes*. John Wiley and Sons, Inc.: New York City, NY, 1993.

(6) Zolandz, R. R.; Fleming, G. K. Economics. In *Membrane Handbook*; Ho, W. S. W.; Sirkar, K. K., Eds.; Kluwer Academic Publishers: Norwell, 1992.

(7) Hong, S. U.; Malaisamy, R.; Bruening, M. L. *Langmuir* **2007,** 23, 1716-1722.

(8) Farhat, T. R.; Schlenoff, J. B. *J. Am. Chem. Soc.* **2003,** 125, 4627-4636.

(9) Corp., A. P. E. Particle size removal range by filtration. http://www.freedrinkingwater.com/water-education/quality-water-filtration-method.htm#Anchor-Pulling-44867 (July 31).

(10) Freeman, B. D.; Pinnau, I. Gas and Liquid Separations Using Membranes: An Overview. In *Advanced Materials for Membrane Separations*; Freeman, B. D.; Pinnau, I., Eds.; Oxford University Press: Washington D.C., 2004; Vol. 876; pp 1-23.

(11) Sridhar, S.; Smitha, B.; Aminabhavi, T. M. *Sep. Purif. Rev.* **2007,** 36, 113-174.

(12) Bos, A.; Punt, I.; Strathmann, H.; Wessling, M. *AIChE J.* **2001,** 47, 1088-1093.

(13) Breck, D. W. *Zeolite Molecular Sieves*. Wiley: New York, 1974; p p. 636.

(14) Zolandz, R. R.; Fleming, G. K. Theory. In *Membrane Handbook*; Ho, W. S. W.; Sirkar, K. K., Eds.; Kluwer Academic Publishers: Norwell, MA, 1992; pp 25-53.

(15) Berens, A. R. *J. Appl. Polym. Sci.* **1989,** 37, 901-913.

(16) Prabhakar, R. S.; Freeman, B. D. Fluoropolymer-Hydrocarbon Polymer Composite Membranes for Natural Gas Separation. In *Advanced Materials for Membrane*

Separations; Pinnau, I.; Freeman, B. D., Eds.; American Chemical Society: Washington D.C., 2004; pp 106-128.

(17) Dhoot, S. N.; Freeman, B. D.; Stewart, M. E.; Hill, A. J. *J. Polym. Sci., Part B: Polym. Phys.* **2001,** 39, 1160-1172.

(18) Prabhakar, R. S.; Freeman, B. D.; Roman, I. *Macromolecules* **2004,** 37, 7688-7697.

(19) Lin, H.; Freeman, B. D. *J. Mol. Struct.* **2005,** 739, 57-74.

(20) Lin, H.; Freeman, B. D. *Macromolecules* **2005,** 38, 8394-8407.

(21) Stern, S. A.; Mullhaup.Jt; Gareis, P. J. *AIChE J.* **1969,** 15, 64-&.

(22) Bondar, V. I.; Freeman, B. D.; Yampolskii, Y. P. *Macromolecules* **1999,** 32, 6163-6171.

(23) van der Vegt, N. F. A.; Kusuma, V. A.; Freeman, B. D. *Macromolecules* **2010,** 43, 1473-1479.

(24) Chandra, M. *Introduction to Polymer Science and Chemistry: A Problem Solving Approach*. Taylor and Francis Group: Boca Raton, 2006.

(25) Lawson, D. D. *Appl. Energy* **1980,** 6, 241-255.

(26) Fogg, P. G. T.; Gerrard, W. *Solubility of Gases in Liquids*. Wiley: New York, 1991.

(27) Lin, H. Q.; Freeman, B. D. *Macromolecules* **2005,** 38, 8394-8407.

(28) Singh, A.; Ghosal, K.; Freeman, B. D.; Lozano, A. E.; de la Campa, J. G.; de Abajo, J. *Polymer* **1999,** 40, 5715-5722.

(29) Ghosal, K.; Chern, R. T.; Freeman, B. D.; Savariar, R. *J. Polym. Sci., Part B: Polym. Phys.* **1995,** 33, 657-666.

(30) Frank, B. P.; Belfort, G. *Langmuir* **1997,** 13, 6234-6240.

(31) Chambers, L. D.; Stokes, K. R.; Walsh, F. C.; Wood, R. J. K. *Surf. Coat. Technol.* **2006,** 201, 3642.

(32) Schumacher, J. F.; Carman, M. L.; Estes, T. G.; Feinberg, A. W.; Wilson, L. H.; Callow, M. E.; Callow, J. A.; Finlay, J. A.; Brennan, A. B. *Biofouling* **2007,** 23, 55.

(33) Hovgaard, M. B.; Rechendorff, K.; Chevallier, J.; Foss, M.; Besenbacher, F. *J. Phys. Chem. B* **2008,** 112, 8241.

(34) Genzer, J.; Efimenko, K. *Biofouling* **2006,** 22, 339.

(35) Callow, J. A.; Callow, M. E.; Ista, L. K.; Lopez, G.; Chaudhury, M. K. *J. R. Soc. Interface* **2005,** 2, 319.

(36) Schmidt, D. L.; Brady, R. F.; Lam, K.; Schmidt, D. C.; Chaudhury, M. K. *Langmuir* **2004,** 20, 2830.

(37) Krishnan, S.; Ayothi, R.; Hexemer, A.; Finlay, J. A.; Sohn, K. E.; Perry, R.; Ober, C. K.; Kramer, E. J.; Callow, M. E.; Callow, J. A.; Fischer, D. A. *Langmuir* **2006,** 22, 5075.

(38) Krishnan, S.; Wang, N.; Ober, C. K.; Finlay, J. A.; Callow, M. E.; Callow, J. A.; Hexemer, A.; Sohn, K. E.; Kramer, E. J.; Fischer, D. A. *Biomacromolecules* **2006,** 7, 1449.

(39) HoipkemeierWilson, L.; Schumacher, J.; Carman, M.; Gibson, A.; Feinberg, A.; Callow, M.; Finlay, J.; Callow, J.; Brennan, A. *Biofouling* **2004,** 20, 53.

(40) Grunlan, J. C.; Choi, J. K.; Lin, A. *Biomacromolecules* **2005,** 6, 1149-1153.

(41) Jansen, B.; Kohnen, W. *J. Ind. Microbiol.* **1995,** 15, 391-396.

(42) Lee, D.; Cohen, R. E.; Rubner, M. F. *Langmuir* **2005,** 21, 9651-9659.

(43) Fu, J.; Ji, J.; Yuan, W.; Shen, J. *Biomaterials* **2005,** 26, 6684-6692.

(44) Rabea, E. I.; Badawy, M. E. T.; Stevens, C. V.; Smagghe, G.; Steurbaut, W. *Biomacromolecules* **2003,** 4, 1457-1465.

(45) Cen, L.; Neoh, K. G.; Kang, E. T. *Langmuir* **2003,** 19, 10295-10303.

(46) Nakagawa, Y.; Hayashi, H.; Tawaratani, T.; Kourai, H.; Horie, T.; Shibasaki, I. *Appl. Environ. Microbiol.* **1984,** 47, 513-518.

(47) Tiller, J. C.; Liao, C.-J.; Lewis, K.; Klibanov, A. M. *Proc. Natl. Acad. Sci. U. S. A.* **2001,** 98, 5981-5985.

(48) Dudley, L. Y.; Darton, E. G. *Desalination* **1997,** 110, 11-20.

(49) Ma, W.; Zhao, Y.; Wang, L. *Desalination* **2007,** 203, 256-259.

(50) Kwak, S.-Y.; Kim, S. H.; Kim, S. S. *Environ. Sci. Technol.* **2001,** 35, 2388-2394.

(51) Zhao, Y.-J.; Wu, K.-F.; Wang, Z.-J.; Zhao, L.; Li, S.-S. *J. Env. Sci.* **2000,** 12, 241-251.

(52) Murali, R. S.; Sridhar, S.; Sankarshana, T.; Ravikumar, Y. V. L. *Ind. Eng. Chem. Res.* **2010,** 49, 6530-6538.

(53) Chafin, R.; Lee, J. S.; Koros, W. J. *Polymer* **2010,** 51, 3462-3471.

(54) Shen, Y.; Lua, A. C. *J. Appl. Polym. Sci.* **2010,** 116, 2906-2912.

(55) Krogman, K. C.; Lowery, J. L.; Zacharia, N. S.; Rutledge, G. C.; Hammond, P. T. *Nat. Mater.* **2009,** 8, 512-518.

(56) Bruening, M.; Dotzauer, D. *Nat. Mater.* **2009,** 8, 449-450.

(57) Pinnau, I.; Koros, W. J. *J. Appl. Polym. Sci.* **1991,** 43, 1491-1502.

(58) Clausi, D. T.; Koros, W. J. *J. Membr. Sci.* **2000,** 167, 79-89.

(59) Sullivan, D. M.; Bruening, M. L. *Chem. Mater.* **2003,** 15, 281-287.

(60) Lai, C. L.; Huang, S. H.; Lin, W. L.; Li, C. L.; Lee, K. R. *J. Membr. Sci.* **2010,** 361, 206-212.

(61) Hung, W. S.; De Guzman, M.; Huang, S. H.; Lee, K. R.; Jean, Y. C.; Lai, J. Y. *Macromolecules* **2010,** 43, 6127-6134.

(62) Jahanshahi, M.; Rahimpour, A.; Peyravi, M. *Desalination* **2010,** 257, 129-136.

(63) Grajales, S. T.; Dong, X.; Zheng, Y.; Baker, G. L.; Bruening, M. L. *Chem. Mater.* **2010,** 22, 4026-4033.

(64) Jain, P.; Dai, J.; Grajales, S.; Saha, S.; Baker, G. L.; Bruening, M. L. *Langmuir* **2007,** 23, 11360-11365.

(65) Jordan, R.; Ulman, A.; Kang, J. F.; Rafailovich, M. H.; Sokolov, J. *J. Am. Chem. Soc.* **1999,** 121, 1016-1022.

(66) Priftis, D.; Sakellariou, G.; Mays, J. W.; Hadjichristidis, N. *J. Polym. Sci., Part A: Polym. Chem.* **2010,** 48, 1104-1112.

(67) Coles, M. P.; Jordan, R. F. *J. Am. Chem. Soc.* **1997,** 119, 8125-8126.

(68) Schuh, K.; Prucker, O.; Ruhe, J. *Macromolecules* **2008,** 41, 9284-9289.

(69) Raghuraman, G. K.; Dhamodharan, R.; Prucker, O.; Ruhe, J. *Macromolecules* **2008,** 41, 873-878.

(70) Raghuraman, G. K.; Ruhe, J.; Dhamodharan, R. *J. Nano. Res.* **2008,** 10, 415-427.

(71) Priftis, D.; Sakellariou, G.; Hadjichristidis, N.; Penott, E. K.; Lorenzo, A. T.; Muller, A. J. *J. Polym. Sci., Part A: Polym. Chem.* **2009,** 47, 4379-4390.

(72) Trnka, T. M.; Grubbs, R. H. *Acc. Chem. Res.* **2001,** 34, 18-29.

(73) Grubbs, R. H.; Chang, S. *Tetrahedron* **1998,** 54, 4413-4450.

(74) Schrock, R. R. *Acc. Chem. Res.* **1990,** 23, 158-165.

(75) Grubbs, R. H. *Tetrahedron* **2004,** 60, 7117-7140.

(76) Nguyen, S. T.; Johnson, L. K.; Grubbs, R. H.; Ziller, J. W. *J. Am. Chem. Soc.* **1992,** 114, 3974-3975.

(77) Braunecker, W. A.; Matyjaszewski, K. *Prog. Polym. Sci.* **2007,** 32, 93-146.

(78) Hawker, C. J.; Bosman, A. W.; Harth, E. *Chem. Rev.* **2001,** 101, 3661-3688.

(79) Benoit, D.; Chaplinski, V.; Braslau, R.; Hawker, C. J. *J. Am. Chem. Soc.* **1999,** 121, 3904-3920.

(80) Hawker, C. J.; Barclay, G. G.; Orellana, A.; Dao, J.; Devonport, W. *Macromolecules* **1996,** 29, 5245-5254.

(81) Fukuda, T.; Terauchi, T.; Goto, A.; Ohno, K.; Tsujii, Y.; Miyamoto, T.; Kobatake, S.; Yamada, B. *Macromolecules* **1996,** 29, 6393-6398.

(82) Chong, Y. K.; Krstina, J.; Le, T. P. T.; Moad, G.; Postma, A.; Rizzardo, E.; Thang, S. H. *Macromolecules* **2003,** 36, 2256-2272.

(83) Coote, M. L. *J. Phys. Chem. A* **2005,** 109, 1230-1239.

(84) Achilleos, M.; Legge, T. M.; Perrier, S.; Patrickios, C. S. *J. Polym. Sci., Part A: Polym. Chem.* **2008,** 46, 7556-7565.

(85) Wang, J. S.; Matyjaszewski, K. *Macromolecules* **1995,** 28, 7901-7910.

(86) Kamigaito, M.; Ando, T.; Sawamoto, M. *Chem. Rec.* **2004,** 4, 159-175.

(87) Edmondson, S.; Osborne, V. L.; Huck, W. T. S. *Chem. Soc. Rev.* **2004,** 33, 14-22.

(88) Matyjaszewski, K., *Advances in Controlled/Living Radical Polymerization*. American Chemical Society: Washington, DC, 2003.

(89) Kabachii, Y. A.; Kochev, S. Y.; Bronstein, L. M.; Blagodatskikh, I. B.; Valetsky, P. M. *Polymer Bulletin* **2003,** 50, 271-278.

(90) Fuji, Y.; Ando, T.; Kamigaito, M.; Sawamoto, M. *Macromolecules* **2002,** 35, 2949-2954.

(91) Onishi, I.; Baek, K. Y.; Kotani, Y.; Kamigaito, M.; Sawamoto, M. *J. Polym. Sci., Part A: Polym. Chem.* **2002,** 40, 2033-2043.

(92) Kotani, Y.; Kamigaito, M.; Sawamoto, M. *Macromolecules* **1999,** 32, 6877-6880.

(93) Matyjaszewski, K.; Wei, M.; Xia, J.; McDermott, N. E. *Macromolecules* **1997,** 30, 8161-8164.

(94) O'Reilly, R. K.; Gibson, V. C.; White, A. J. P.; Williams, D. J. *Polyhedron* **2004,** 23, 2921-2928.

(95) Ishio, M.; Katsube, M.; Ouchi, M.; Sawamoto, M.; Inoue, Y. *Macromolecules* **2009,** 42, 188-193.

(96) Wang, B.; Zhuang, Y.; Luo, X.; Xu, S.; Zhou, X. *Macromolecules* **2003,** 36, 9684-9686.

(97) Granel, C.; Dubois, P.; Jerome, R.; Teyssie, P. *Macromolecules* **1996,** 29, 8576-8582.

(98) Uegaki, H.; Kamigaito, M.; Sawamoto, M. *J. Polym. Sci., Part A: Polym. Chem.* **1999,** 37, 3003-3009.

(99) Uegaki, H.; Kotani, Y.; Kamigaito, M.; Sawamoto, M. *Macromolecules* **1998,** 31, 6756-6761.

(100) Brandts, J. A. M.; van de Geijn, P.; van Faassen, E. E.; Boersma, J.; Van Koten, G. *J. Organomet. Chem.* **1999,** 584, 246-253.

(101) Le Grognec, E.; Claverie, J.; Poli, R. *J. Am. Chem. Soc.* **2001,** 123, 9513-9524.

(102) Maria, S.; Stoffelbach, F.; Mata, J.; Daran, J.-C.; Richard, P.; Poli, R. *J. Am. Chem. Soc.* **2005,** 127, 5946-5956.

(103) Baek, K. Y.; Kamigaito, M.; Sawamoto, M. *J. Polym. Sci., Part A: Polym. Chem.* **2002,** 40, 1937-1944.

(104) Baek, K. Y.; Kamigaito, M.; Sawamoto, M. *J. Polym. Sci., Part A: Polym. Chem.* **2002,** 40, 2245-2255.

(105) Kamigaito, M.; Watanabe, Y.; Ando, T.; Sawamoto, M. *J. Am. Chem. Soc.* **2002,** 124, 9994-9995.

(106) Terashima, T.; Ouchi, M.; Ando, T.; Sawamoto, M. *J. Polym. Sci., Part A: Polym. Chem.* **2010,** 48, 373-379.

(107) Yoda, H.; Nakatani, K.; Terashima, T.; Ouchi, M.; Sawamoto, M. *Macromolecules* **2010,** 43, 5595-5601.

(108) Percec, V.; Barboiu, B.; Neumann, A.; Ronda, J. C.; Zhao, M. *Macromolecules* **1996,** 29, 3665-3668.

(109) Moineau, G.; Granel, C.; Dubois, P.; Jerome, R.; Teyssie, P. *Macromolecules* **1998,** 31, 542-544.

(110) Lecomte, P.; Drapier, I.; Dubois, P.; Teyssie, P.; Jerome, R. *Macromolecules* **1997,** 30, 7631-7633.

(111) Kotani, Y.; Kamigaito, M.; Sawamoto, M. *Macromolecules* **2000,** 33, 6746-6751.

(112) Braunecker, W. A.; Itami, Y.; Matyjaszewski, K. *Macromolecules* **2005,** 38, 9402-9404.

Chapter Two

Effects of Monomer Composition on CO2-Selective Polymer Brush Membranes

This work was performed in collaboration with Xiaojie Dong and Ying Zhang and published in Chemistry of Materials: Grajales, S. T.; Dong, X.; Zheng, Y.; Baker, G. L.; Bruening, M. L. *Chem. Mater.* **2010,** 22, 4026-4033.

This chapter describes the formation of composite, PEG-containing membranes through atom transfer radical polymerization of poly(ethylene glycol methyl ether methacrylate) from initiator-modified, porous substrates. The resulting membrane skins are only 50-500 nm thick, and copolymers that contain a mixture of short and long PEG side chains do not readily crystallize. The smaller PEG chains (8-9 ethylene oxide units) prevent crystallization, while the presence of longer side chains (23-24 ethylene oxide units) allows the membranes to maintain a CO_2/H_2 selectivity of 12 at room temperature. This work examines the effect of side-chain length on polymerization rate as well as the permeability, selectivity, and crystallinity of copolymer films. Reflectance FTIR spectroscopy reveals the fraction of different monomers incorporated into copolymer films and demonstrates when crystallization occurs

Introduction

Selective removal of CO_2 from gas streams is becoming increasingly important for applications such as CO_2 sequestration,[1] fuel cell operation,[2] and H_2 synthesis.[3] In the case of H_2 production, steam reforming of methane produces 9 million tons of H_2 per year in the U.S. alone.[4] However, the product stream from steam reforming theoretically contains 20 mole% CO_2, so purification of the H_2 is an important and expensive part of the production process.[5] A number of studies examined membrane-based gas separation as a possible alternative, or as a pre-purification step, to the pressure swing adsorption process currently used in H_2 purification.[6, 7] The viability of membrane processes for purifying H_2 streams depends critically on achieving both high flux and high selectivity, and a recent review summarizes the types of membranes employed for H_2 purification.[8] Processes such as H_2 recycle in ammonia synthesis have employed H_2-selective membranes for several decades.[9] In the case of CO_2 removal from H_2 streams, however, CO_2-selective membranes are attractive because purified H_2 remains on the high pressure side of the membrane and does not need to be recompressed.

The solution diffusion model for transport through membranes Eq. (2.1) illustrates how the flux, J, of a gas through a membrane depends on the partial pressure drop across the membrane, Δp, the membrane thickness, l, and the gas permeability, P, which is the product of the solubility coefficient, S, and diffusivity, D, for the gas of interest.[10] Eq. (2.2) shows that the ideal selectivity of gas A over gas B, $\alpha_{A/B}$, depends on the solubility coefficients and diffusivities of the two gases. Because of its small size, H_2 has a greater diffusivity than CO_2, so CO_2/H_2 selectivity requires high solubility selectivity for CO_2 over H_2. Fortunately, CO_2 is the more condensable of the two gases, and solubility selectivity typically favors CO_2 transport.[10]

$$J = \frac{P\Delta p}{l} \qquad P = SD \tag{2.1}$$

$$\alpha_{A/B} = \frac{P_A}{P_B} = \frac{S_A \times D_A}{S_B \times D_B} \tag{2.2}$$

Membrane materials employed for selective passage of CO_2 over H_2 should thus have a higher affinity for CO_2 than H_2 along with a relatively high free volume that minimizes the difference between CO_2 and H_2 diffusivities. One method of increasing CO_2 solubility is the incorporation of protonated amines within the membrane.[11, 12] In this case, facilitated transport can lead to CO_2/H_2 selectivities over 100, but carrier saturation often limits the application of these systems to low feed pressures (less than 0.05 bar).[13-15] At room temperature, amorphous poly(ethylene glycol) (PEG)-containing membranes exhibit CO_2/H_2 selectivities ranging from 5 to 12, presumably because of quadrupole-dipole interactions between CO_2 and the ether functional groups of PEG.[16-19] Unfortunately, however, crystallization of PEG chains decreases both the permeability and selectivity of such membranes. To overcome this challenge, several studies employed cross-linked, solution-cast, PEG-containing membranes to maintain a high free volume, decrease crystallinity, and increase chemical stability.[7, 20-22] In the best case, the cross-linked membranes show CO_2 permeabilities of up to 600 Barrers [1 Barrer = 10^{-10} cm^3 (STP) $\cdot$cm / ($cm^2\cdot s\cdot cmHg$) = 7.5×10^{-18} m^3 (STP) $\cdot m/(m^2\cdot s\cdot Pa)$] and CO_2/H_2 selectivities of approximately 12 at room temperature.[23]

Nevertheless, the high thickness (>100 μm) of solution-cast membranes yields a permeance (permeance is defined as flux/Δp) that is too low for practical separations. This work examines the use of atom transfer radical polymerization (ATRP) from porous substrates to create composite membranes with thin (50-500 nm) skins of PEG-containing films that allow selective removal of CO_2 from H_2 streams. ATRP is attractive for synthesizing these membrane skins because it often affords control over film thickness along with polymer chains with relatively low polydispersity.[24, 25] Scheme 2.1 shows two permutations of the ATRP process for forming membranes on porous alumina substrates, and similar processes on porous polymer supports are also possible. Initiator attachment occurs either via adsorption of a disulfide initiator to gold-coated alumina to generate A (scheme 2.1), or attachment of a silane directly to the alumina to generate B. Subsequent atom transfer radical polymerization with a Cu^+/1,1,4,7,10,10-hexamethyltriethylenetetramine

(HMTETA) catalyst yields the membrane skin. Because of the small thickness of the membrane skins, the permeances of the modified alumina membranes are several orders of magnitude greater than those of solution-cast membranes.[8]

Additionally, this work examines the use of copolymers prepared from poly(ethylene glycol methyl ether methacrylate) (PEGMEMA) monomers with different PEG chain lengths (Scheme 2.2) to inhibit the crystallization of the PEG side chains. The combination of monomers with 8-9 and 23-24 ethylene oxide repeat units yields films that do not crystallize over many months and membrane skins with a room temperature CO_2/H_2 selectivity of around 12.

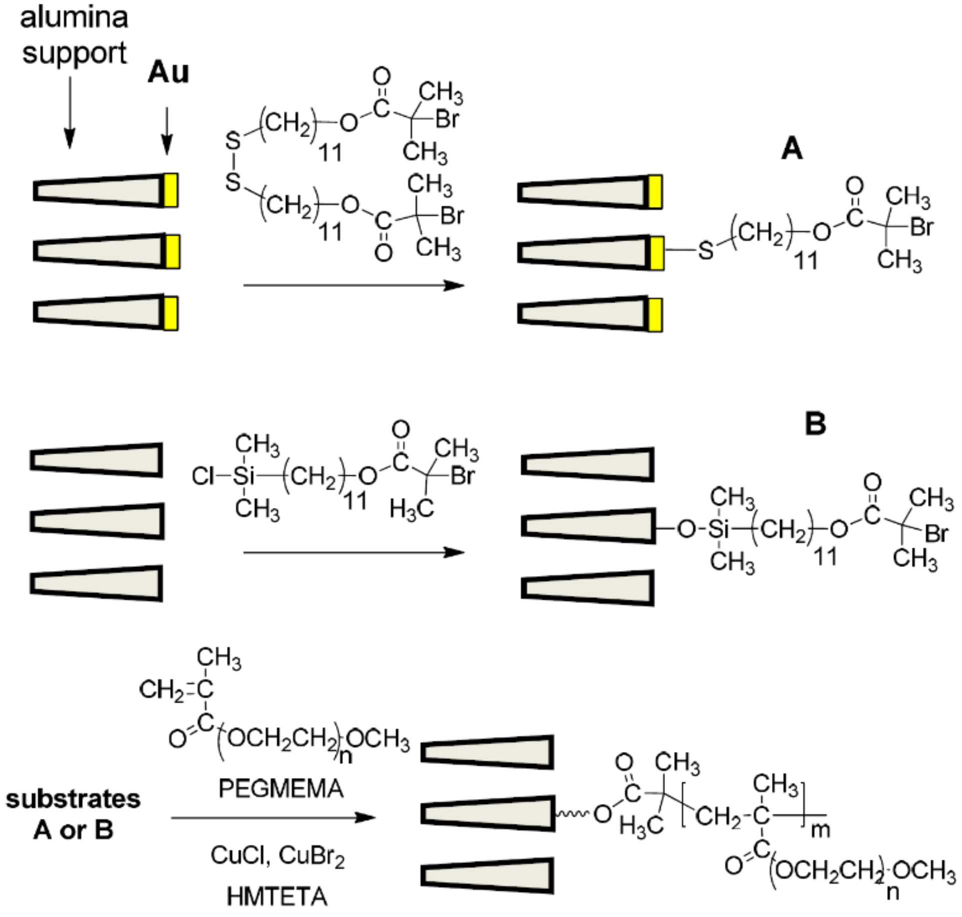

Scheme 2.1: Methods for growth of a poly(PEGMEMA) membrane from porous alumina.

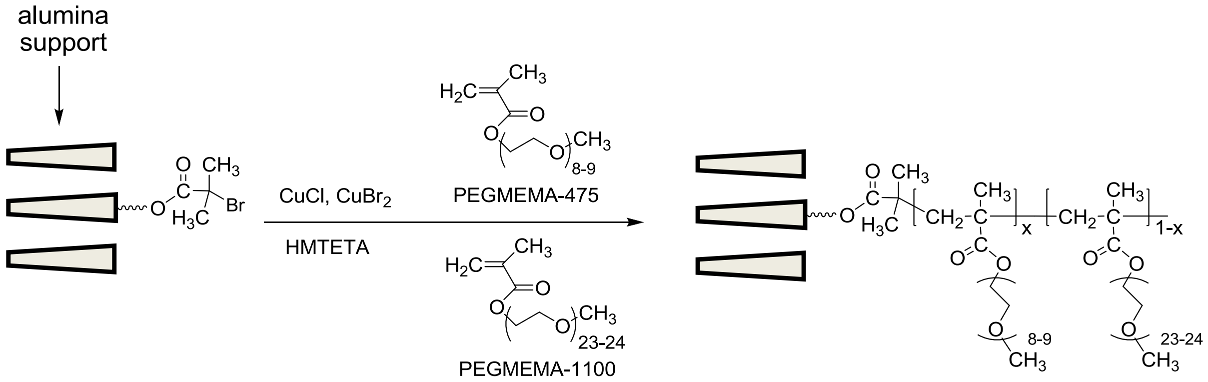

Scheme 2.2: Copolymerization of PEGMEMA-475 and PEGMEMA-1100 to provide a membrane skin.

Experimental

Chemicals. PEGMEMA monomers with M_n = 300 Da (PEGMEMA-300), M_n = 475 Da (PEGMEMA-475), and M_n = 1,100 Da (PEGMEMA-1100) were obtained from Aldrich. These monomers contain both 100 ppm 4-methoxyphenol and 300 ppm 2,6-di*tert*-butyl-4-methylphenol as inhibitors. Proton NMR spectra (see Appendix A) show that the average numbers of ethylene oxide units in PEGMEMA-300, PEGMEMA-475, and PEGMEMA-1100 are 4.4, 8.8, and 23.1, respectively. In some cases, the inhibitors were removed from the monomers using flash column chromatography with basic alumina, but this did not have a significant effect on polymerizations, so in most reactions the monomers were used as received. The CuCl, $CuBr_2$, and 1,1,4,7,10,10-hexamethyltriethylenetetramine (HMTETA) were purchased from Aldrich, and deionized water was obtained using a Millipore system (Milli-Q, 18.2 MΩ·cm). THF was distilled over sodium metal with benzophenone, and DMF was distilled over 4 Å molecular sieves. Silicon(100) wafers were obtained from NOVA Electronic Materials and sputter-coated with 20 nm of chromium followed by 200 nm of gold by LGA Thin Films (Santa Clara, CA). The porous alumina substrates were Anodisc membrane filters (25 mm disks with 0.02 µm surface pores) purchased from

Whatman, and the disulfide, $[Br\text{-}C(CH_3)_2\text{-}COO(CH_2)_{11}S]_2$, and silane, $SiCl(CH_3)_2(CH_2)_{11}OCOC(CH_3)_2Br$, initiators were synthesized as described previously.[26-29]

Polymerization. Porous alumina substrates were initially rinsed with ethanol, dried with N2, UV/O3 cleaned (Boekel UV-Clean Model 135500) for 15 min, and sputter coated with 5 nm of gold in a Pelco SC-7 sputter coater. The thickness of the gold coating was monitored with a Pelco FTM-2 quartz crystal microbalance. Attachment of a monolayer of the disulfide initiator to gold-coated Si wafers or porous alumina occurred during an overnight immersion of the substrate in an ethanolic solution containing 1 mM disulfide initiator. The resulting sample was rinsed with 5 mL of ethanol and dried in a N2 stream. Attachment of the silane initiator occurred during overnight immersion of an uncoated, UV/ozone-cleaned porous alumina substrate in a solution containing 8 mM silane in THF. The resulting sample was rinsed with 5 mL THF and dried in a N2 stream. The two different types of initiator-modified membranes were handled identically in the ensuing polymerization steps.

Following a previous procedure, the catalyst stock solution was prepared by first dissolving 0.06 g (0.6 mmol) of CuCl and 0.04 g (0.2 mmol) of $CuBr_2$ in 30.0 mL of distilled, degassed DMF.[30, 31] This solution was further degassed via three freeze, pump, thaw cycles. In a N_2-filled glove bag, 490 μL (1.8 mmol) of degassed 1,1,4,7,10,10-hexamethyltriethylenetetramine (HMTETA) ligand was added to this solution, which subsequently turned a dark green color during several hours of stirring. During this initial stirring, a small amount of material precipitated, but the resulting catalytic activity of the solution remained constant for at least several weeks. The nominal mole ratio of Cu^{+}:Cu^{2+}:HMTETA was 3:1:9.

The monomer solution, which contained 0.75 M PEGMEMA in water, was initially degassed via three freeze, pump, thaw cycles. (When different molecular weight monomers were used, the total monomer concentration was maintained at 0.75 M). The polymerization solution was prepared in a N_2-filled glove bag by combining degassed monomer and catalyst solutions in a 9:1 volume ratio to produce a blue-green solution containing 0.67 M monomer, 2.0 mM CuCl, 0.60 mM $CuBr_2$, and 6.0 mM HMTETA. The initiator-modified membranes or wafers were immersed in the polymerization solution for designated periods of time, and the resulting polymer films were rinsed with 5 mL water and soaked in water for at least two hours before rinsing with 5 mL of ethanol and drying under a N_2 stream.

Characterization methods. Reflectance FT-IR spectroscopy was performed using a Nicolet Magna-IR 560 spectrometer with a Pike grazing angle (80°) attachment. A UV/ozone-cleaned, gold-coated Si wafer was used to obtain the background spectrum. Thicknesses of films formed on gold-coated Si were determined with a rotating analyzer ellipsometer (J.A. Woollam model M44) at an incident angle of 75°. A two-term Cauchy equation was employed to simultaneously fit film thickness and the Cauchy constants needed to model the wavelength-dependence of the film refractive index. Thicknesses were determined at a minimum of three locations on each substrate. Scanning electron microscopy was performed with the JEOL semi-in-lens cold cathode field-emission scanning electron microscope, model JSM-7500F, operating with a r-filter in signal maximum mode. Samples were sputter coated with 5 nm of gold prior to imaging.

Gas Permeation. Single gas permeation experiments were performed by exposing the membrane to individual gases at varying pressures in an Advantec/MFS UHP-25 cell with a pressure relief valve. The gas flow rate through the membrane was measured with either an Optiflow 420 electronic soap bubble meter or a manual soap bubble meter. Mixed-gas experiments were performed by loading the membrane into a custom membrane holder (all connections utilized

Swagelok fittings and were tested to ensure that they maintained pressure over a time-scale longer than the experiment) that allowed cross-flow of the feed gas as well as a sweep gas on the permeant side. A backpressure valve was employed to sustain the feed gas pressure, and the feed flow rate was high enough to maintain constant composition at the face of the membrane (the stage-cut, or ratio of permeant flow to feed flow, was <1%). The N_2 sweep gas/permeant stream was connected to an automated six-port injector valve on a Hewlett-Packard 6890 GC equipped with a thermal conductivity detector (TCD) and an Agilent GS-CarbonPLOT capillary column (i.d. = 0.53 mm, length = 30 m, 3 μm coating). The mixed gas permeances as well as pure gas permeances were calculated from GC results using Eq. (2.3),

$$\text{Permeance} = \frac{\chi_{\mathrm{B}} \times \Phi_{\mathrm{N_2}}}{\chi_{\mathrm{N_2}} \times \mathrm{A} \times \Delta p} \tag{2.3}$$

where χ_B is the mole fraction of a particular permeate gas, *B*, in the gas mixture injected into the GC column, Φ_{N_2} is the sweep gas flow rate, χ_{N_2} is the mole fraction of N_2 in the gas injected into the GC column, Δp is the transmembrane partial pressure difference for the gas of interest, and A is the membrane area. (Φ_{N_2} / χ_{N_2} is the sum of the permeate and sweep gas flow rate, and χ_{N_2} was determined by subtracting the mole fractions of the permeates from unity. This assumes that the amount of N_2 passing from permeate to feed was negligible.) The sweep gas flow rate was programmed into a mass flow controller, pressure and area were measured, and the mole fractions were determined from the integrated GC spectra and a calibration curve.

Results and Discussion

Polymerization Rates as a Function of Monomer Composition. The first step in developing surface-initiated ATRP for creating membrane skins, especially for forming copolymer skins, is examination of polymerization from model flat substrates such as gold-coated Si wafers.[32] Such substrates facilitate ellipsometric and spectroscopic characterization of polymer growth and composition. We are particularly interested in the relative film growth rates for PEGMEMA-475, PEGMEMA-1100, and their mixtures because the short side chains of PEGMEMA-475 do not crystallize, whereas the long chains of PEGMEMA-1100 should promote CO_2/H_2 selectivity.[33] As Figure 2.1 shows, polymerization of PEGMEMA-475 by itself gives the most rapid initial growth in film thickness, but the growth rate decreases dramatically after 15 min of polymerization. In contrast, polymerization of PEGMEMA-1100 is slower, but the film growth rate is essentially constant for 120 min. Interestingly, surface-initiated polymerizations of mixtures in which PEGMEMA-475 constitutes either 25 or 75 mole% of the total monomer show relatively high and steady growth rates.

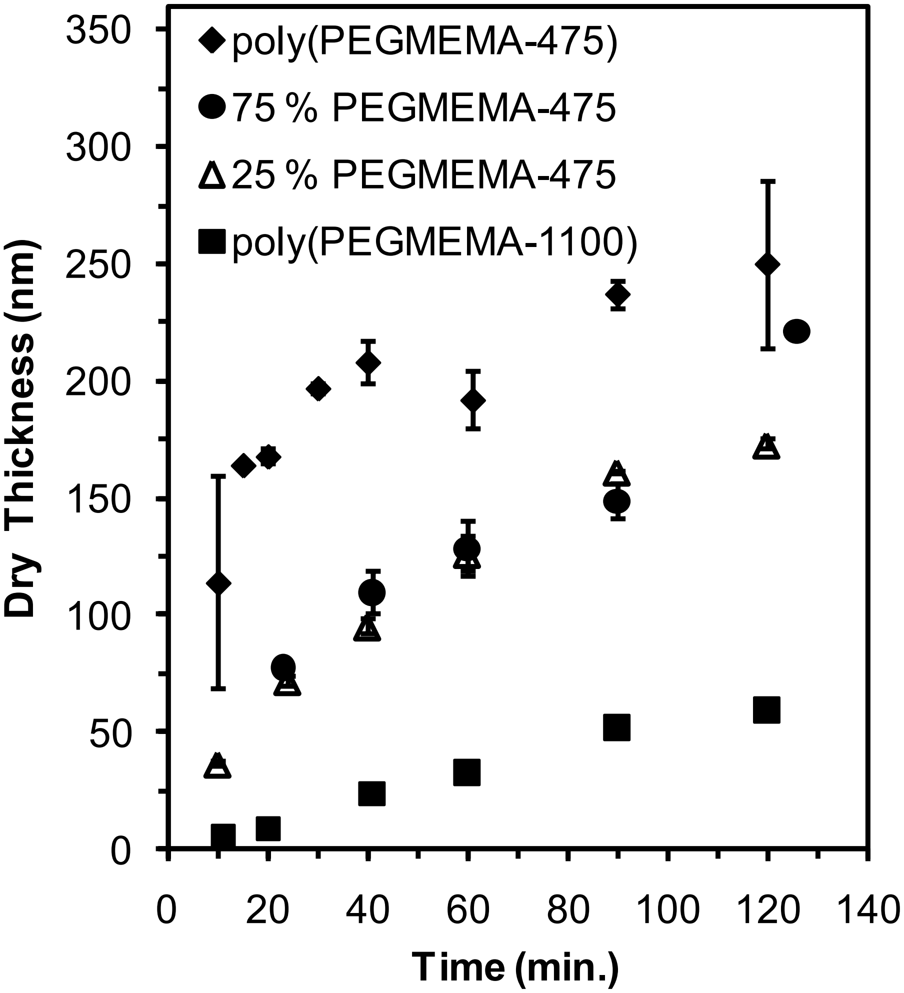

Figure 2.1: Evolution of film thickness with time in surface-initiated polymerization of pure and mixed monomer solutions. For copolymers, the legend shows the solution PEGMEMA-475 mole percentage with respect to the total monomer (PEGMEMA-475 plus PEGMEMA-1100). The overall monomer concentration was 0.67 M, and the catalyst system was 2.0 mM CuCl, 0.60 mM $CuBr_2$, and 6.0 mM HMTETA. The error bars, which in many cases are obscured by the symbols, represent one standard deviation.

Decreases in growth rates with polymerization time, particularly for poly(PEGMEMA-475), suggest that the HMTETA-$Cu^{+/2+}$ catalyst system gives a high concentration of radicals that results in significant termination by radical-radical coupling. The large side chains of PEGMEMA-1100 may provide steric hindrance to both polymerization and termination. In solution polymerization studies, Haddleton *et al.* attributed the high ATRP activity of

PEGMEMA-475 relative to PEGMEMA-1100 to ethylene oxide coordination with the Cu catalyst in close proximity to the double bond.[34] However, steric issues seem equally likely to affect polymerization.[33] In the case of homopolymerization from surfaces, the PEGMEMA-1100 solutions are also more viscous and contain less water than PEGMEMA-475 solutions, and both of these factors should also lead to lower polymerization rates for the PEGMEMA-1100. Mixtures of PEGMEMA-475 and PEGMEMA-1100 have intermediate polymerization rates, and the side chains are apparently still sufficiently large to reduce termination relative to pure PEGMEMA-475. For PEGMEMA-475, PEGMEMA-1100, and their mixtures, film growth is rapid compared to polymerization of most other monomers and non-aqueous polymerizations.[35-37] A number of studies demonstrated that the presence of water frequently enhances the rate of ATRP.[38, 39]

Determining the Composition of Copolymer Films. The molar ratio of PEGMEMA-475 to PEGMEMA-1100 in a film may not correspond to the monomer ratio in the polymerization solution. In particular, the smaller monomer may be more reactive because of faster diffusion to the surface or less steric hindrance to polymerization. In an attempt to determine the relative amounts of each monomer incorporated in poly(PEGMEMA-475-*co*-PEGMEMA-1100) films, we compared the intensities of carbonyl (1731 cm^{-1}) and C-O-C (1149 cm^{-1}) stretches in both homopolymer and copolymer films. The reflectance FTIR spectra in Figure 2.2 show that for amorphous homopolymer films, the intensity of the C-O-C stretch relative to the C=O stretch is much higher for poly(PEGMEMA-1100) than poly(PEGEMEMA-475), as would be expected because of the longer PEG chain in the higher molecular weight monomer.

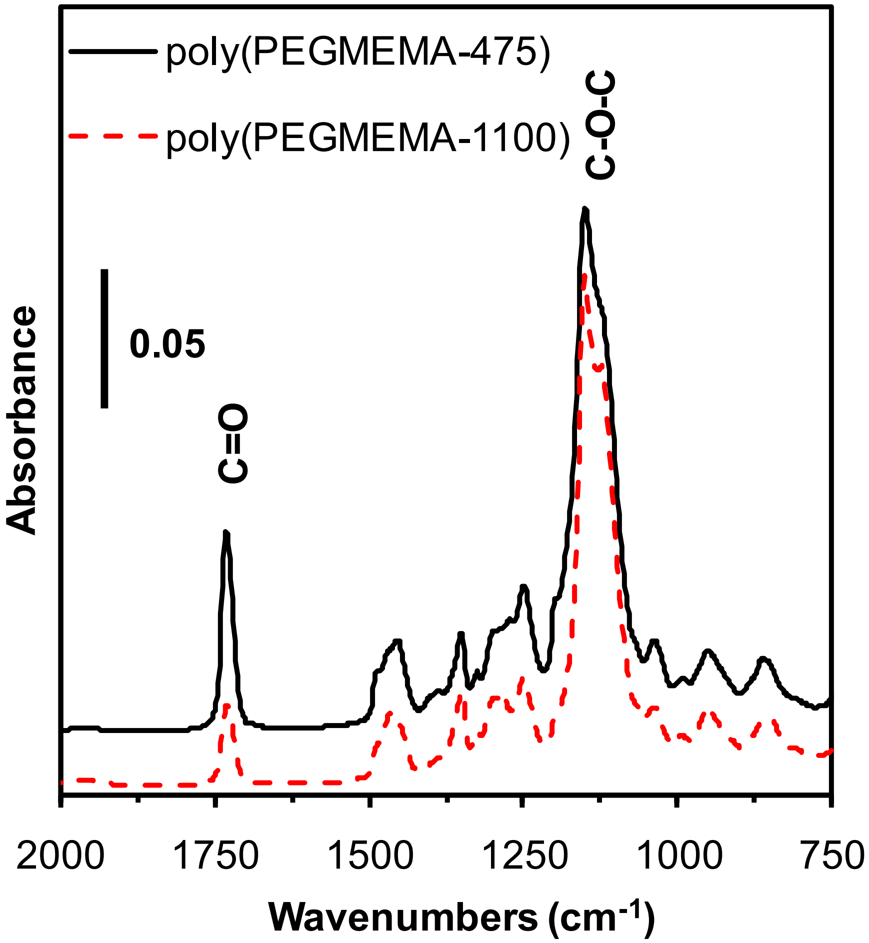

Figure 2.2: FTIR spectra of 152 nm-thick poly(PEGMEMA-475) (black line) and 118 nm-thick poly(PEGMEMA-1100) (dashed red line) films on gold-coated substrates. Spectra were taken immediately after polymerization before the PEG side chains in poly(PEGMEMA-1100) crystallized. The spectra are offset for clarity.

We initially planned to estimate the mole ratios of monomers incorporated into a copolymer film using Eq. 2.4, where x_{475} is the mole fraction of PEGMEMA-475 in a copolymer film and R_{co}, R_{1100}, and R_{475} are the ratios of the C-O-C peak height (1149 cm^{-1}) to the C=O peak height (1731 cm^{-1}) for copolymer, poly(PEGMEMA-1100), and poly(PEGMEMA-475) films, respectively.

$$R_{co} = x_{475} R_{475} + (1 - x_{475}) R_{1100} \tag{2.4}$$

However, Figure 2.3 suggests that in some cases peak height and peak area ratios for the C-O-C to C=O absorbance increase with film thickness for homopolymer and copolymer films. This increasing ratio of C-O-C to C=O absorbance likely occurs because reflectance measurements plot $\log(R_o/R)$, where R_o and R are the reflectivities of bare and film-covered substrates, respectively. These reflectivities are complicated functions of the film thickness and the complex refractive indices, $\tilde{n}$, of the substrate and the film. To account for these complications in reflectance FTIR spectroscopy, we performed Fresnel calculations to determine the absorption coefficient, *k*, for different films at the wavelengths of interest. Appendix A provides the details of these calculations and shows that the calculated absorption coefficients do not vary significantly with the thicknesses of the films (Figure A.2).

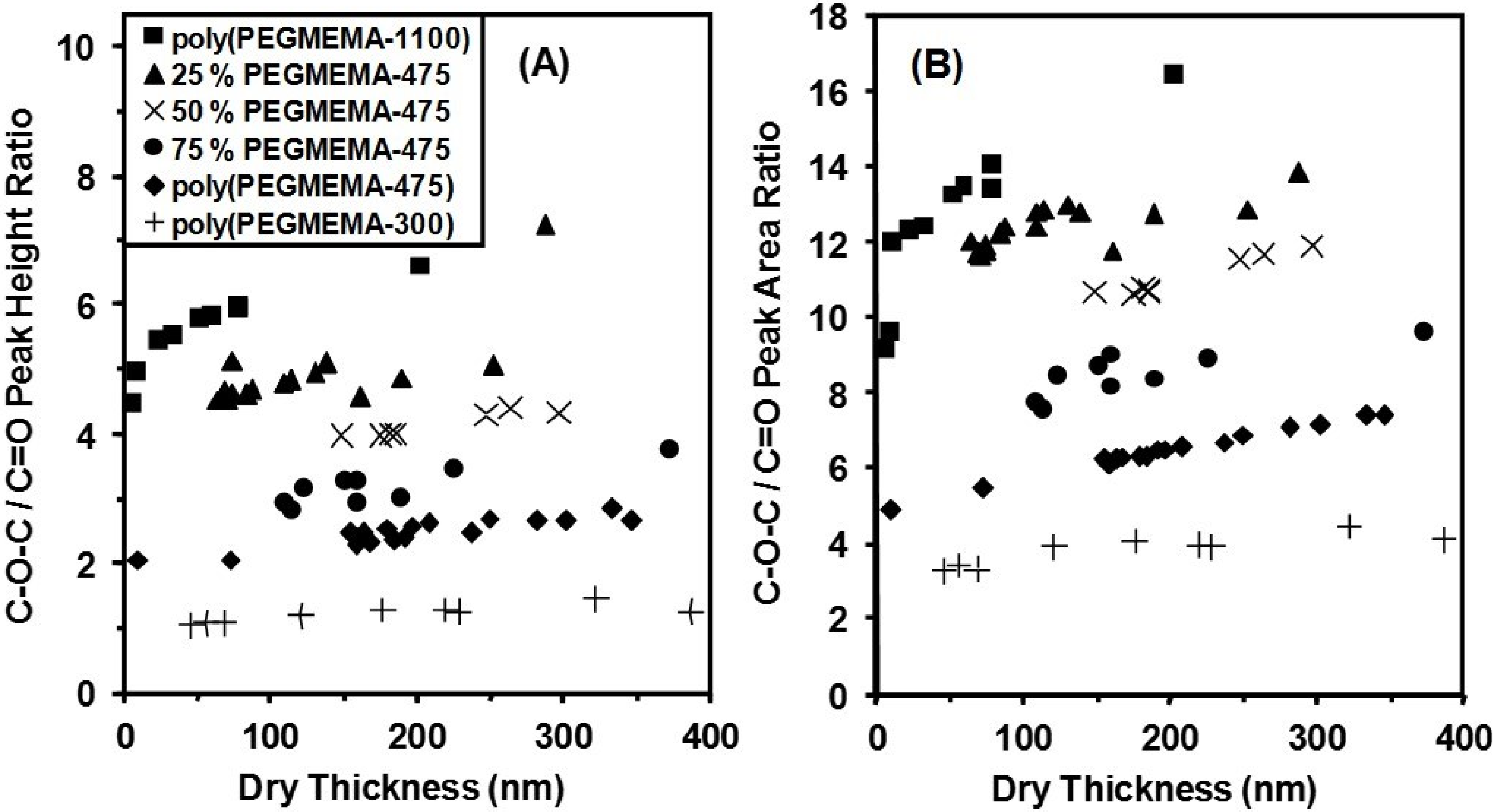

Figure 2.3: Ratios of C-O-C to C=O peak heights (A) and peak areas (B) in reflectance FTIR spectra of poly(PEGMEMA-1100), poly(PEGMEMA-475), poly(PEGMEMA-300) and poly(PEGMEMA-475-*co*-PEGMEMA-1100) films on gold-coated substrates. The ratios are plotted as a function of the ellipsometric thickness of the film, and for the copolymers, the legend shows the mole fraction of PEGMEMA-475 (relative to total monomer) in the polymerization solution. All polymerizations employed a total monomer concentration of 0.67 M, and the experimental section describes the polymerization conditions.

We used the k values for three homopolymer films, poly(PEGMEMA-300), poly(PEGMEMA-475), and poly(PEGMEMA-1100), to create a calibration curve (Figure 2.4) of the $k_{C\text{-}O\text{-}C}$ / $k_{C=O}$ ratio versus the average number of ethylene oxide units per repeat unit, EO_{avg}, and then calculated EO_{avg} in copolymer films.

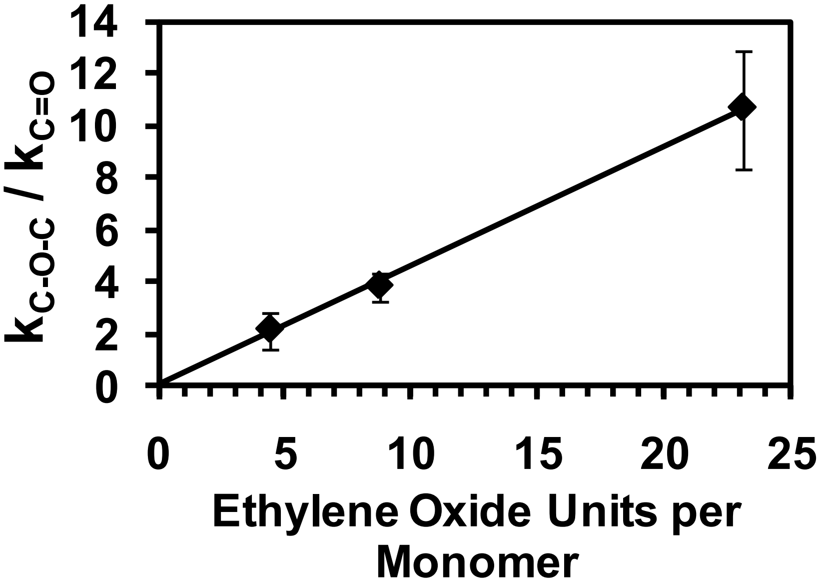

Figure 2.4: Ratios of C-O-C (1149 cm^{-1}) and C=O (1731 cm^{-1}) absorption coefficients, k, as a function of the average number of ethylene oxide units per repeat unit, EO_{avg}, in poly(PEGMEMA-300), poly(PEGMEMA-475), and poly(PEGMEMA-1100) films. The ethylene oxide units per monomer were calculated from ^{1}H-NMR spectra of monomers, and the standard deviations in the absorption coefficient ratios were determined using films with thicknesses ranging from 5 to 454 nm. The line is a fit to the data with a zero intercept.

For poly(PEGMEMA-475-*co*-PEGMEMA-1100), this EO_{avg} value is a direct function of the fraction of each monomer in the copolymer and the average number of ethylene oxide units in each monomer Eq. (2.5).

$$\mathrm{EO}_{\mathrm{avg}} = 8.8x_{475} + 23.1(1 - x_{475}) \tag{2.5}$$

The reflectance FTIR data and the Fresnel calculations show that the ratios of PEGMEMA-475 to PEGMEMA-1100 in poly(PEGMEMA-475-*co*-PEGMEMA-1100) films are approximately the same as those in the solutions from which they grow (Table 2.1). This is somewhat surprising considering the large differences in the initial growth rates as well as termination rates for surface-initiated homopolymerization of the two monomers (Figure 2.1). However, in the case of copolymers, solutions containing 25 mole% and 75 mole% PEGMEMA-475 give essentially the same initial growth rate (Figure 2.1), which is consistent with the similarity between solution and film compositions. This direct correlation between solution and film compositions affords straightforward control over the ratio of long and short side chains to minimize PEG crystallization and maximize CO_2/H_2 selectivity in membranes.

Table 2.1: Composition of poly(PEGMEMA-475-*co*-PEGMEMA-1100) films[a] as a function of the PEGMEMA-475 mole percentages in the polymerization solution.[b]

Feed Solution, mole% PEGMEMA-475	Polymer Composition, mole% PEGMEMA-475	EO_{avg}
0	0	23 ± 1
25	33 ± 2	18 ± 1
50	54 ± 3	15 ± 1
75	71 ± 7	13 ± 1
100	100	8.7 ± 0.6

[a] Film compositions were determined from reflectance FTIR spectra and Fresnel calculations (see text) and are expressed as both mole percent and the average number of ethylene oxide (EO_{avg}) groups per repeat unit. The uncertainties, which were calculated using propagation of error, represent one standard deviation. [b] The mole percentage in the feed solution is relative to the total amount of monomer in solution.

Crystallization of PEG Side Chains. PEG chains crystallize in helices that contain two turns per 7 EO units over a length of 19.3 Å,[40-42] and helix formation leads to splitting of the 1150 cm^{-1} C-O-C IR band into peaks at 1120 and 1148 cm^{-1} and a narrowing of the CH_2 wagging peak at 1360 cm^{-1}.[40, 41] In PEGMEMA films, long PEG side chains crystallize similarly, and Figure

2.5A demonstrates the changes in reflectance FTIR spectra that occur upon crystallization of a poly(PEGMEMA-1100) film.

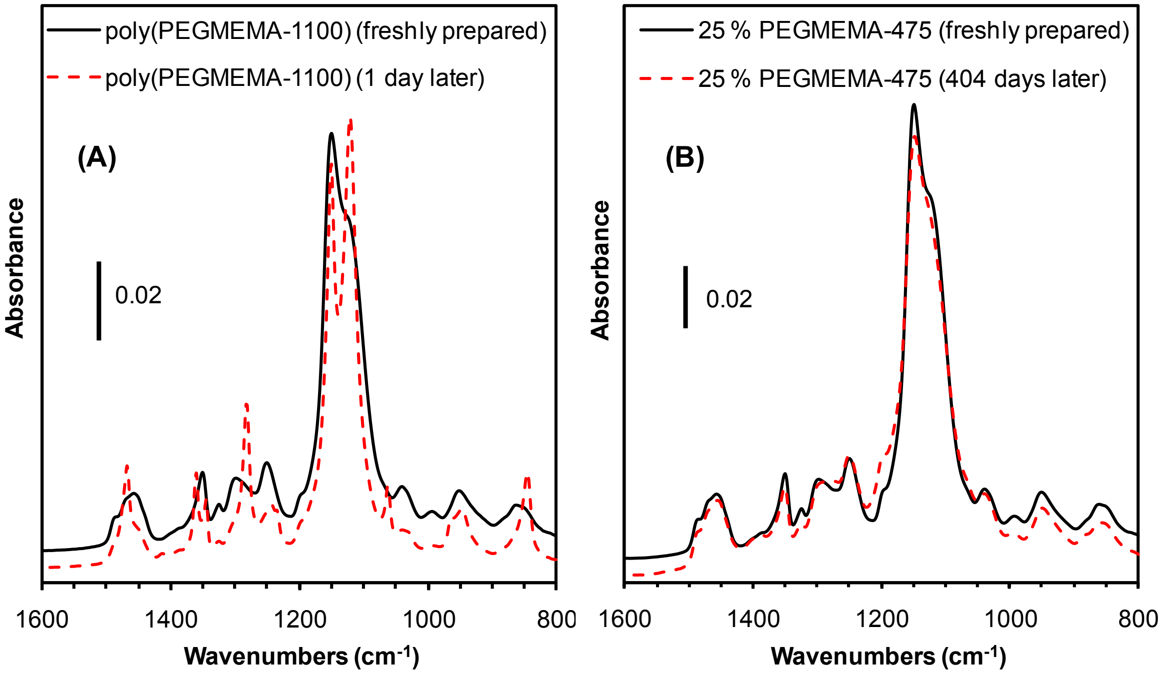

Figure 2.5: Reflectance FTIR spectra of (A) 60 nm-thick poly(PEGMEMA-1100) immediately after polymerization (solid black line) and 24 hours later (dashed red line) and (B) 97 nm-thick poly(PEGMEMA-475-*co*-PEGMEMA-1100) immediately after polymerization (solid black line) and 404 days later (dashed red line). The copolymer was prepared from a solution containing 25 mole% PEGMEMA-475 and 75 mole% PEGMEMA-1100.

Previous reports of PEG crystallization in related coatings suggest that the helical axis preferentially orients perpendicular to the surface in films less than 100 nm thick, and both perpendicular and parallel to the surface in thicker films.[27, 43-46]

However, the presence of crystallinity, rather than its orientation, is the primary concern for creating selective membranes with high permeabililties, and prior studies reveal that the PEG chain length, not film thickness, is the primary factor in determining whether crystallization occurs.[47, 48] In contrast to poly(PEGMEMA-1100), poly(PEGMEMA-475) films do not show any evidence of crystallization in reflectance FTIR spectra, presumably because neighboring PEG side chains are too short to crystallize in this environment.[49]

Importantly, copolymers prepared from PEGMEMA-1100 and PEGMEMA-475 show no sign of crystallization, even when the fraction of PEGMEMA-475 in the film is only ~25%. Figure 2.5B shows that the reflectance FTIR spectrum of a poly(PEGMEMA-475-*co*-PEGMEMA-1100) film remains unchanged even after more than a year at room temperature. The presence of the short chains is apparently sufficient to inhibit crystallization of the longer side chains, and this effect occurs for films prepared from solutions containing PEGMEMA-475 as 25, 50, and 75 mole% of the total monomer.

Formation of Gas-Separation Membranes by ATRP. Composite membranes are attractive for gas separations because the minimal thickness of the thin, selective skin allows for high flux, and the underlying support provides mechanical strength. Hence, the goal in using ATRP to create a membrane skin is to completely cover a porous substrate with a thin film without filling the underlying pores. The first step in the formation of membranes by ATRP is attachment of an initiator to the surface. To be consistent with our work on gold wafers, we sputtered 5 nm of gold on porous alumina and subsequently adsorbed a monolayer of the disulfide initiator on the surface (Scheme 2.1A). In a separate procedure, to avoid the deposition of gold on the membrane surface, we also attached a silane initiator directly to the alumina (Scheme 2.1B). Because alumina membranes are expensive and fragile, we are also working on growing membrane skins on polymeric ultrafiltration membranes. This is more challenging, however, because the solvents employed in initiator attachment may damage the underlying membrane. Aqueous adsorption of macroinitiators may overcome this problem.[38]

Subsequent polymerization of PEGMEMA from initiators on alumina yields the desired composite membranes. Figure 2.6 shows a SEM image of a composite membrane containing a poly(PEGMEMA-475-*co*-PEGMEMA-1100) skin on a porous alumina support. The film is thin (130 nm) and clearly covers the pores without filling them. However, selective gas permeation studies are needed to demonstrate that the films are defect-free and non-crystalline.

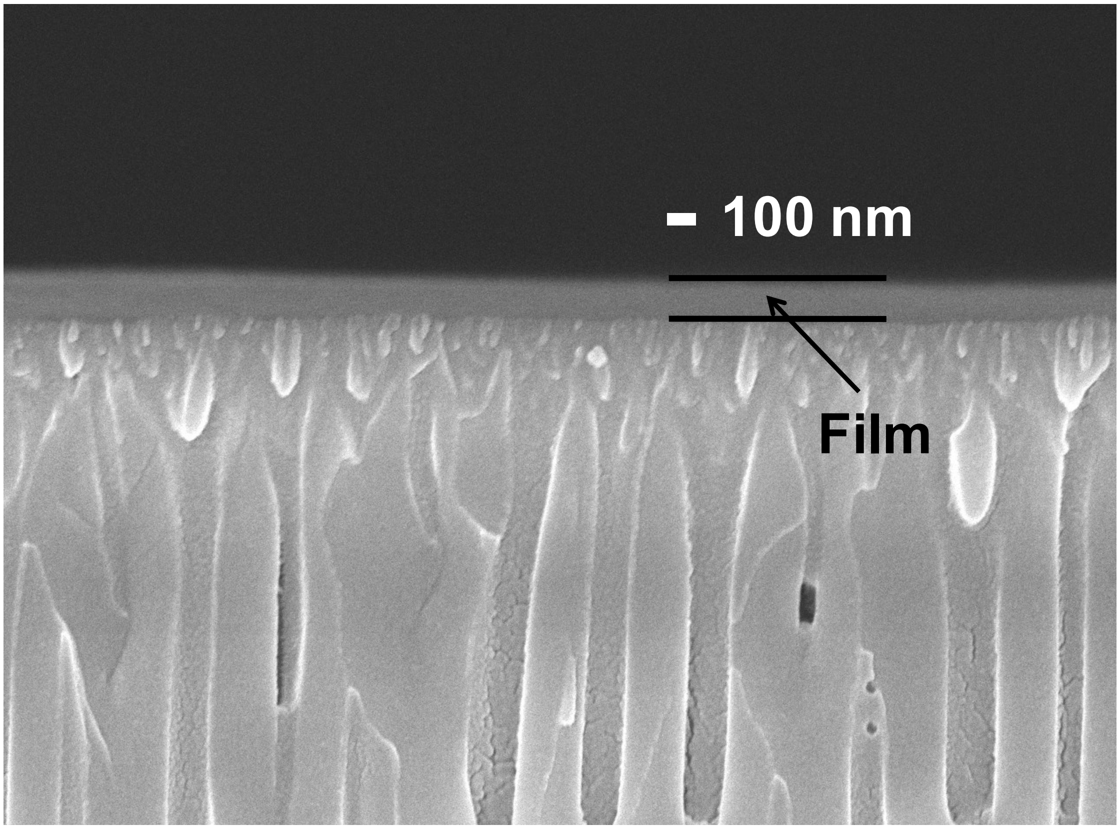

Figure 2.6. SEM image of the cross section of a gold-coated porous alumina membrane modified with a poly(PEGMEMA-475-*co*-PEGMEMA-1100) film. The alumina exhibits unfilled vertical pores covered by a 130 nm-thick film that was grown from an aqueous solution containing 25 mole% PEGMEMA-475 and 75 mole% PEGMEMA-1100.

Gas Permeation through Poly(PEGMEMA) Membranes. Figure 2.7 shows the CO_2 and H_2 fluxes through porous alumina membranes coated with either a poly(PEGMEMA-1100) film or a copolymer film grown from a solution containing a 1:1 mole ratio of PEGMEMA-475 and PEGMEMA-1100. For poly(PEGMEMA-1100), the initial CO_2/H_2 selectivity is 12 ± 1. The highest room-temperature CO_2/H_2 selectivity of PEG-containing membranes in the literature is also 12.[7, 21-23] However, the CO_2/H_2 selectivity of the poly(PEGMEMA-1100) film drops to less than 1 within a day because the CO_2 flux decreases 12-fold (Figure 2.7A). This drop in CO_2 flux is almost certainly due to crystallization of the PEG side chains, which as noted above occurs within one day of synthesis of poly(PEGMEMA-1100) films.

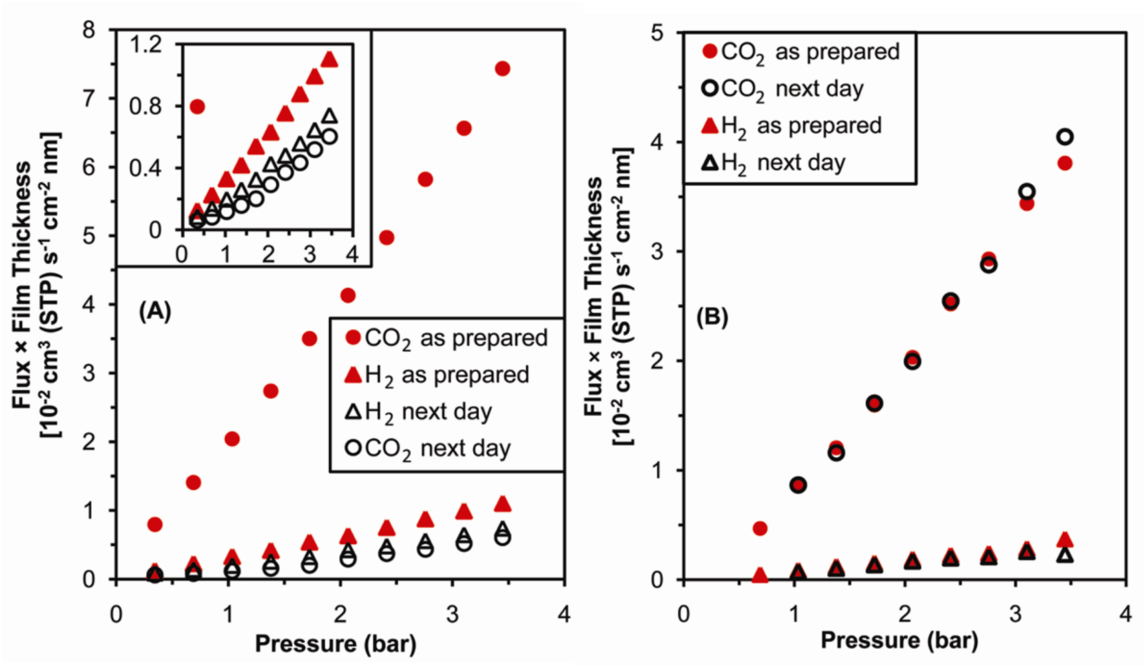

Figure 2.7: Single-gas fluxes through gold-coated porous alumina membranes capped with (A) poly(PEGMEMA-1100) or (B) poly(PEGMEMA-475-*co*-PEGMEMA-1100) grown from a solution containing 50 mole% PEGMEMA-475. (Fluxes are normalized by multiplying by the SEM thickness of the membrane skin.) The circles represent CO_2 data, and the triangles represent H_2 data; filled symbols represent measurements taken immediately after synthesis, and open symbols represent data obtained 24 h later. The inset in Figure A shows the data on an expanded ordinate for clarity.

By comparison, poly(PEGMEMA-475) films exhibit an initial CO_2/H_2 selectivity of 9 ± 2. On silylated supports, poly(PEGMEMA-1100) and poly(PEGMEMA-475) films show selectivities of 13 ± 1 and 5.8 ± 0.5, respectively, demonstrating that there is a significant difference between the gas selectivities of these two polymers. The poly(PEGMEMA-475) films contain a smaller overall fraction of PEG than poly(PEGMEMA-1100), which likely explains their lower selectivity. However, the selectivity of the poly(PEGMEMA-475) does not decrease with time because the shorter chains do not crystallize.

The goal of using copolymers as membranes is to achieve the initial selectivity of poly(PEGMEMA-1100) films while avoiding decreases in selectivity and flux due to film crystallization. Figure 2.7B shows that a poly(PEGMEMA-475-*co*-PEGMEMA-1100) film (prepared on gold-coated alumina using a solution containing 50 mole% PEGMEMA-475) has an initial CO_2/H_2 selectivity of 12-13, which is essentially the same as that of the pure poly(PEGMEMA-1100). Moreover, the selectivity of the copolymer membranes is constant over at least several weeks at room temperature, again presumably because the side chains of PEGMEMA-475 inhibit crystallization. Figure 8 shows the dependence of CO_2/H_2 selectivity on the mole fraction of PEGMEMA-475 in poly(PEGMEMA-475-*co*-PEGMEMA-1100) films. As long as there is 75 mole% or less PEGMEMA-475 in the polymerization solution, membranes formed on gold-coated alumina maintain average CO_2/H_2 selectivities of 12 at room temperature. The films grown from silylated alumina show a maximum CO_2/H_2 selectivity of 17 ± 2 with copolymers generated from a 50 mole% PEGMEMA-475 polymerization solution, but a selectivity of only 7 when using 75 mole% PEGMEMA-475. Silanization is more likely to produce initiators within the pores of the alumina, which might somewhat alter film structure at the support surface and change selectivity relative to films on gold-coated alumina. Moreover, the initiator packing densities might be different for the gold-coated and silylated surfaces.

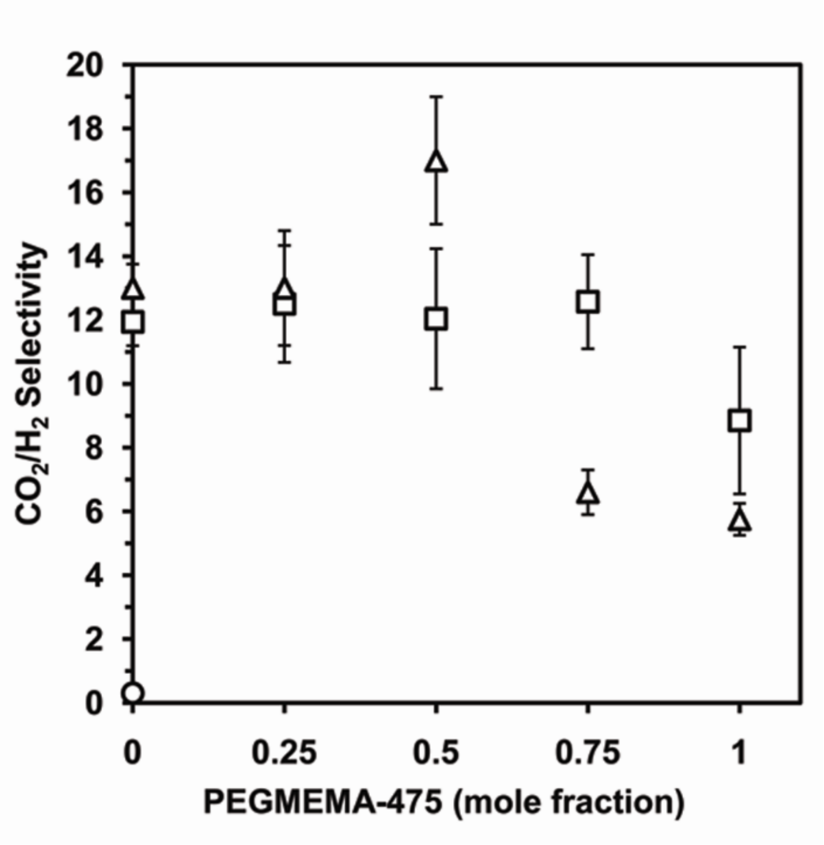

Figure 2.8: Single-gas CO_2/H_2 selectivity vs. mole fraction of PEGMEMA-475 in the monomer solution used to create amorphous poly(PEGMEMA-475-*co*-PEGMEMA-1100) films on porous alumina membranes. The triangles represent films grown from silylated alumina, and the squares represent films grown from initiators on gold-coated alumina. For the poly(PEGMEMA-1100) homopolymer on silylated alumina, the open circle near the origin represents selectivity after crystallization. Error bars are one standard deviation.

Determination of the permeability, *P*, of the films on porous alumina is challenging because of the difficulty in obtaining accurate values for film thickness [Eq. (2.1)]. Film thicknesses in multiple cross-sectional SEM images of a given membrane typically show a relative standard deviation (rsd) of 10-30%, although sometimes we see even larger variations. Based on SEM images of membranes with a rsd in thickness <25%, the H_2 permeability of poly(PEGMEMA-475-*co*-PEGMEMA-1100) films ranges from 2 to 6 Barrers, and the CO_2 permeability ranges from 20 to 60 Barrers. (Given the uncertainty in thickness, we could not differentiate among permeabilities of films with different compositions.) Typical CO_2 permeabilities of PEG-containing films range from 12 Barrers in pure PEG[50] to 570 Barrers in cross-linked PEG-based acrylates.[49, 51] This wide range of permeabilities in different PEG-containing polymers stems from differences in fractional free volume and the presence of different polar groups that alter the solubility of gases in the membrane.[23, 52, 53] Although the poly(PEGMEMA-475-*co*-PEGMEMA-1100) films do not exhibit as high a permeability as some cross-linked films, the ultrathin skin maximizes permeance for a given permeability. To improve permeability, future studies will examine cross-linking to increase flux in these films.

Selectivities in gas mixtures can differ significantly from those with single gases, particularly when absorption of a gas such as CO_2 plasticizes the membranes.[54] In mixed-gas experiments, plasticization may increase the flux of H_2 and decrease CO_2/H_2 selectivity relative to single-gas measurements. With feed gas streams of 79.7 mole% H_2 and 20.3 mole% CO_2, the CO_2/H_2 selectivity was only 13% lower on average than the pure gas CO_2/H_2 selectivities.

Summary

In their amorphous state, composite poly(PEGMEMA-1100) membranes provide high CO_2 permeances and CO_2/H_2 selectivities, but crystallization can decrease flux by an order of magnitude and reduce CO_2/H_2 selectivity to below 1. Copolymerization of two PEGMEMA monomers, one containing 8-9 and the other 23-24 ethylene oxide units per side chain, avoids the problem of crystallization and yields films that maintain an amorphous state for more than a year. Reflectance FTIR spectra indicate that the ratio of the PEGMEMA-475 and PEGMEMA-1100 incorporated into copolymer films is within 8% of the ratio of the monomers in the polymerization solution. Membranes consisting of porous alumina supports coated with copolymer films exhibit stable single-gas CO_2/H_2 selectivities around 12 at room temperature, which is attractive for CO_2 removal from H_2 streams.

Acknowledgements

We thank the U.S. Department of Energy Office of Basic Energy Sciences for funding and S. Koszalka and Dr. Kathryn Severin for their assistance.

APPENDIX

APPENDIX

Effects of Monomer Composition on CO2-Selective Polymer Brush Membranes

Determination of absorption coefficients in reflectance IR spectra

We plot reflectance IR spectra as $\log(R_o/R)$, where R_o is the fraction of the incident light intensity reflected by a bare gold substrate (Figure A.1A) and R is the fraction of incident light intensity reflected by a film-coated substrate (Figure A.1B).

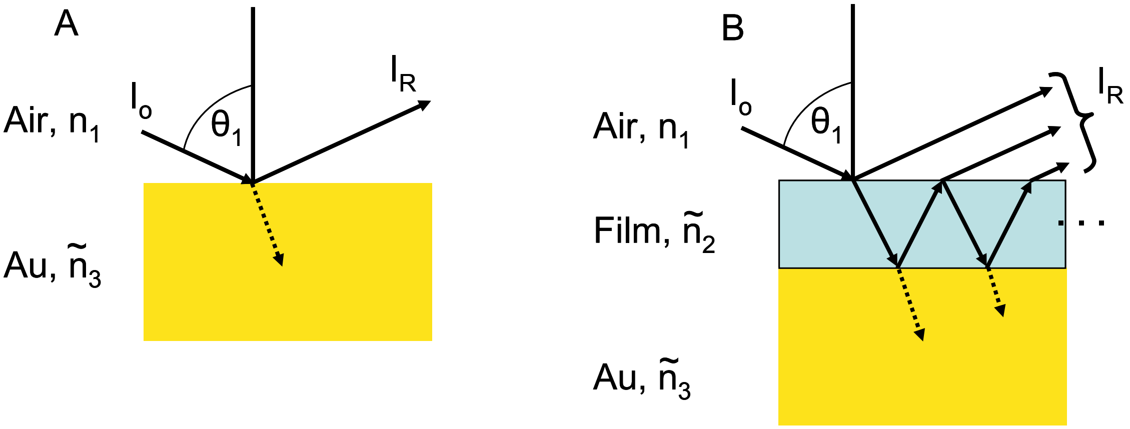

Figure A.1: Schematic drawing of the reflection of light from (A) a bare gold surface and (B) a film-covered gold surface.

The value of R_o is simply the Fresnel reflection coefficient, r_{13}, multiplied by its complex conjugate Eq. (A.1), where the Fresnel coefficient is given by Eq. (A.2). In equation S2, $\tilde{n}_3$ is the complex refractive index of gold, *n-ik*, (assumed to be 3-30*i*), θ_1 is the angle of incidence (80 º), n_1 is the refractive index of air (assumed to be 1.000), and $\tilde{\theta}_{Au}$ is the complex angle of refraction in the gold film. The value of $\tilde{\theta}_{Au}$ was calculated using Snell's law, Eq. (A.3). (Tilda superscripts indicate a complex number.)

$$R_o = \tilde{r}_{13}\tilde{r}_{13}^{\ *} \tag{A.1}$$

$$r_{13} = \frac{\tilde{n}_3 \cos\theta_1 - n_1 \cos\tilde{\theta}_{Au}}{\tilde{n}_3 \cos\theta_1 + n_1 \cos\tilde{\theta}_{Au}} \tag{A.2}$$

$$n_1 \sin\theta_1 = \tilde{n}_3 \sin\tilde{\theta}_{Au} \tag{A.3}$$

Eq. (A.4) allows calculation of the reflectance, R, of the film-covered substrate, where the * represents the complex conjugate. In this equation, $\tilde{r}_{12}$ is the Fresnel reflection coefficient for the air-film interface, Eq. (A.5), $\tilde{r}_{23}$ is the Fresnel reflection coefficient for the film-gold interface Eq. (A.6), λ is the wavelength of the incident light in air, $\tilde{n}_2$ is the complex refractive index of the film, l is the film thickness, and $\cos\tilde{\theta}_2$ and $\cos\tilde{\theta}_3$ can be calculated using Snell's law for the appropriate interfaces.

$$\begin{gathered} R = \left(\frac{\tilde{r}_{12} + \tilde{r}_{23}e^{-2i\delta}}{1 + \tilde{r}_{12}\tilde{r}_{23}e^{-2i\delta}}\right)\left(\frac{\tilde{r}_{12} + \tilde{r}_{23}e^{-2i\delta}}{1 + \tilde{r}_{12}\tilde{r}_{23}e^{-2i\delta}}\right)^{*} \\ \delta = \frac{2\pi\tilde{n}_2}{n_1\lambda} l \cos\tilde{\theta}_2 \end{gathered} \tag{A.4}$$

$$r_{12} = \frac{\tilde{n}_2 \cos\theta_1 - n_1 \cos\tilde{\theta}_2}{\tilde{n}_2 \cos\theta_1 + n_1 \cos\tilde{\theta}_2} \tag{A.5}$$

$$r_{23} = \frac{\tilde{n}_3 \cos\tilde{\theta}_2 - n_2 \cos\tilde{\theta}_3}{\tilde{n}_3 \cos\tilde{\theta}_2 + n_2 \cos\tilde{\theta}_3} \tag{A.6}$$

To calculate the absorption coefficient, *k*, for a specific polymer film, we determined the absorbance peak heights at 1731 cm^{-1} (C=O stretch) and at 1149 cm^{-1} (C-O-C stretch) from reflectance IR spectra. It is important to note that the presence of a film on the gold substrate changes the reflectivity of the surface even in the absence of absorption (when k=0), meaning that the film-covered gold gives rise to a baseline shift that must be taken into consideration when calculating peak heights. Specifically, this correction was made by calculating the absorbance when k=0 and subtracting this from the calculated peak absorbance to generate a corrected peak height. This correction was used along with the above equations to iteratively calculate the absorption coefficient, *k*, which gives rise to the measured peak height value for a particular film. The ratios of calculated absorption coefficients, $k_{\text{C-O-C}}/k_{\text{C=O}}$, were independent of thickness for a given film composition, as Figure A.2 shows below.

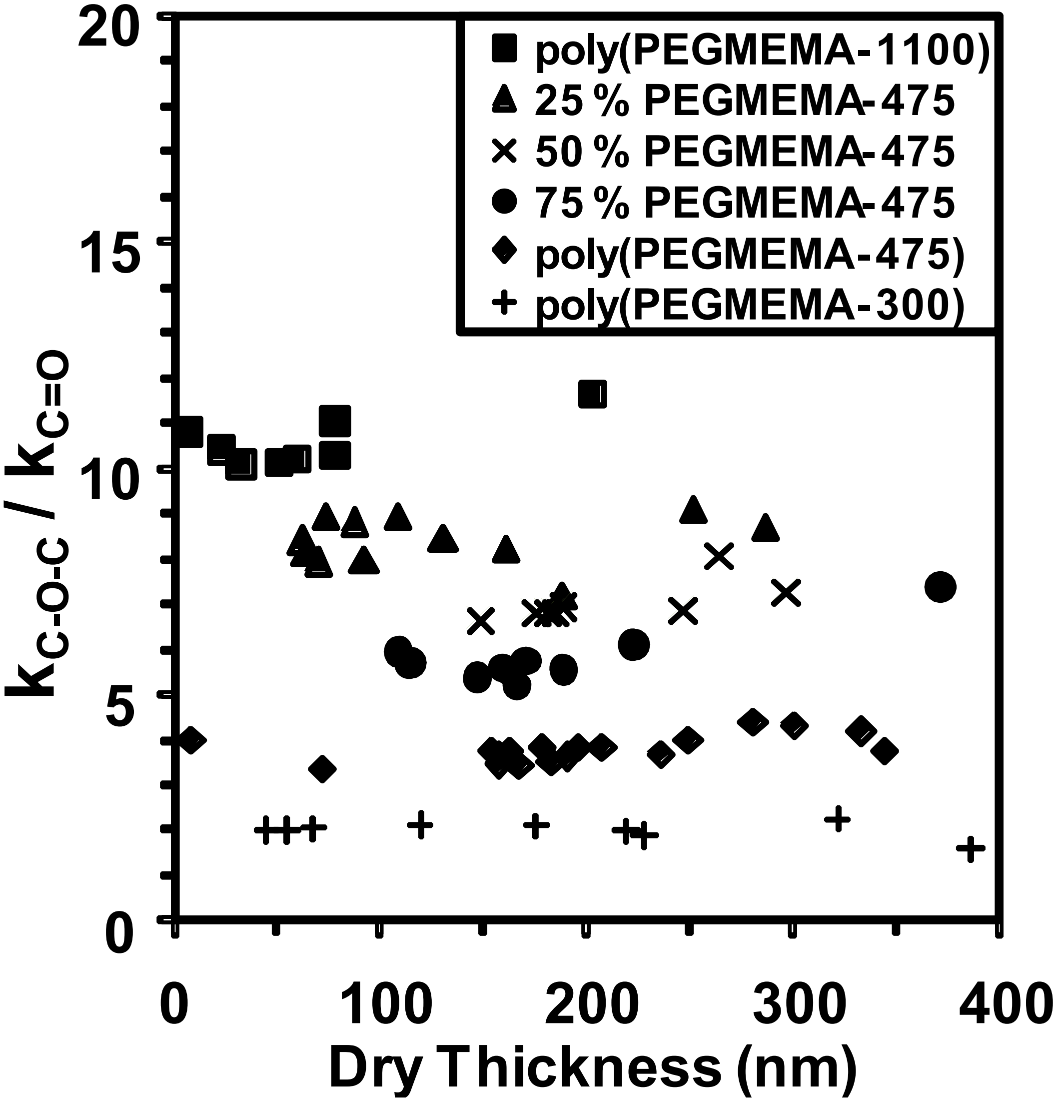

Figure A.2: Ratios of the C-O-C (1149 cm^{-1}) and C=O (1731 cm^{-1}) absorption coefficients in poly(PEGMEMA) homo and copolymer films as a function of film thickness. In the case of copolymer films, the legend shows the PEGMEMA-475 mole percentage of total monomer in the polymerization solution, and the rest of the monomer was PEGMEMA-1100. The polymerization was performed as described in the experimental section.

We averaged the ratios of calculated absorption coefficients for homopolymer films of different thicknesses (see Table A.1) to plot the dependence of $k_{C\text{-}O\text{-}C}/k_{C=O}$ on the average ethylene oxide units per monomer (Figure A.4). This calibration curve allows the thickness-independent conversion from $k_{C\text{-}O\text{-}C}/k_{C=O}$ to the average number of EO groups per repeat unit in copolymer films.

Table A.1: Absorption coefficients, k, of homopolymer films. The k values were calculated using Eq. (A.1-A.5) and the peak absorbances corresponding to C-O-C and C=O stretches. The uncertainty is one standard deviation of the values obtained from films with a range of thicknesses.

Homopolymer	Wavenumber, cm^{-1}	Bond Stretch	Absorption Coefficient, *k*
PEGMEMA-300	1149	C-O-C	0.30±.08
	1731	C=O	0.14±0.03
PEGMEMA-475	1149	C-O-C	0.42±0.05
	1731	C=O	0.11± 0.01
PEGMEMA-1,100	1149	C-O-C	0.48±0.08
	1731	C=O	0.045± 0.006

Average numbers of ethylene oxide units in each of the different monomers (PEGMEMA-300, -475, and -1100) were determined from NMR spectra (Figure A.3). Averaging three NMR spectra of each monomer, the integrals of the peaks with a chemical shift between 3.4 ppm and 4.5 ppm (arising from the four hydrogen atoms on the ethylene oxide repeat units) were summed and divided by 4 to give the average number of EO units per monomer. (The intensity of the alkene protons was set to 1 for normalization.)

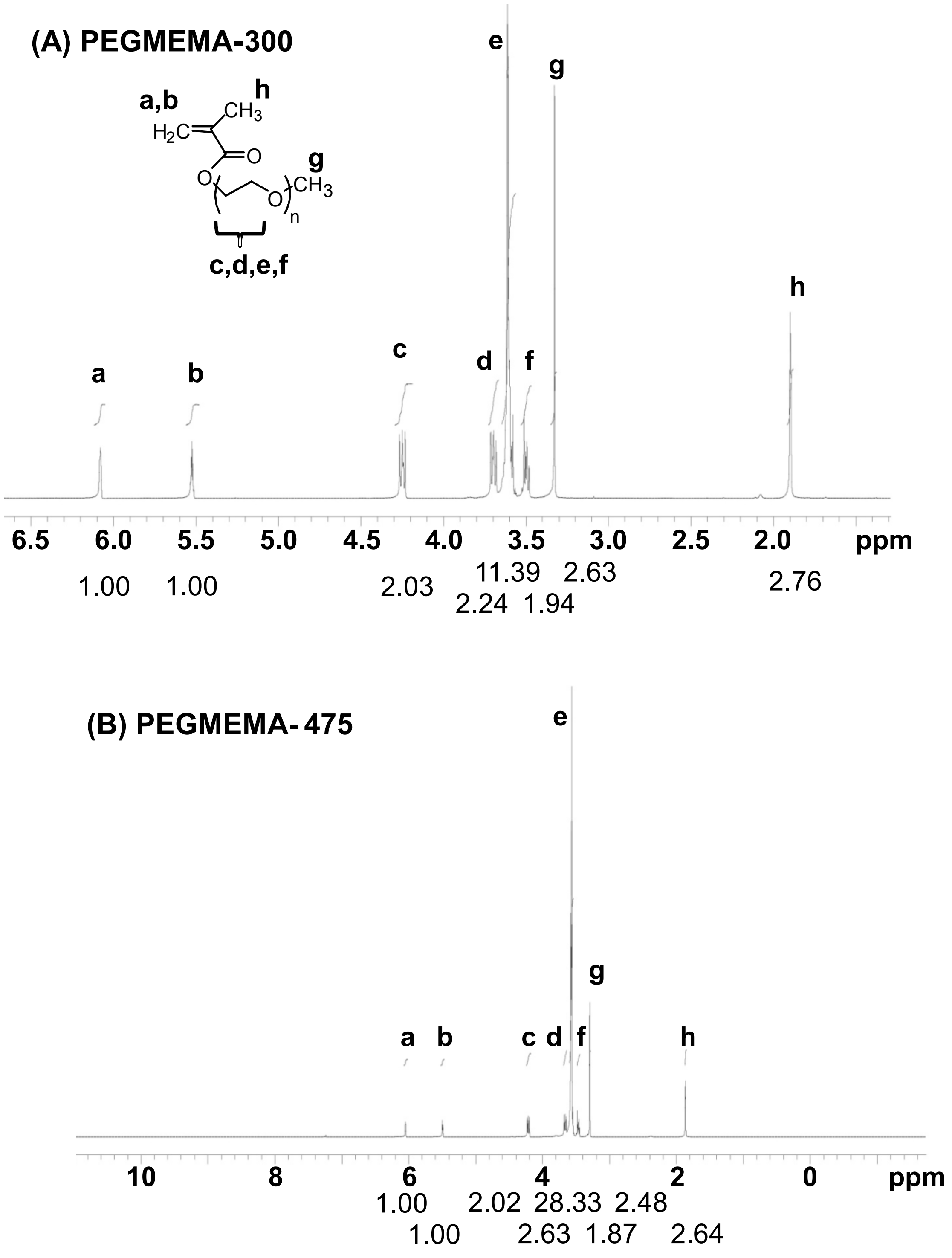

Figure A.3: Proton NMR spectra of (A) PEGMEMA-300, (B) PEGMEMA-475, and (C) PEGMEMA-1100. Peak areas in these spectra were averaged with areas from two additional replicate spectra to generate values for the number of average ethylene oxide units per monomer.

Figure A.3 (cont'd)

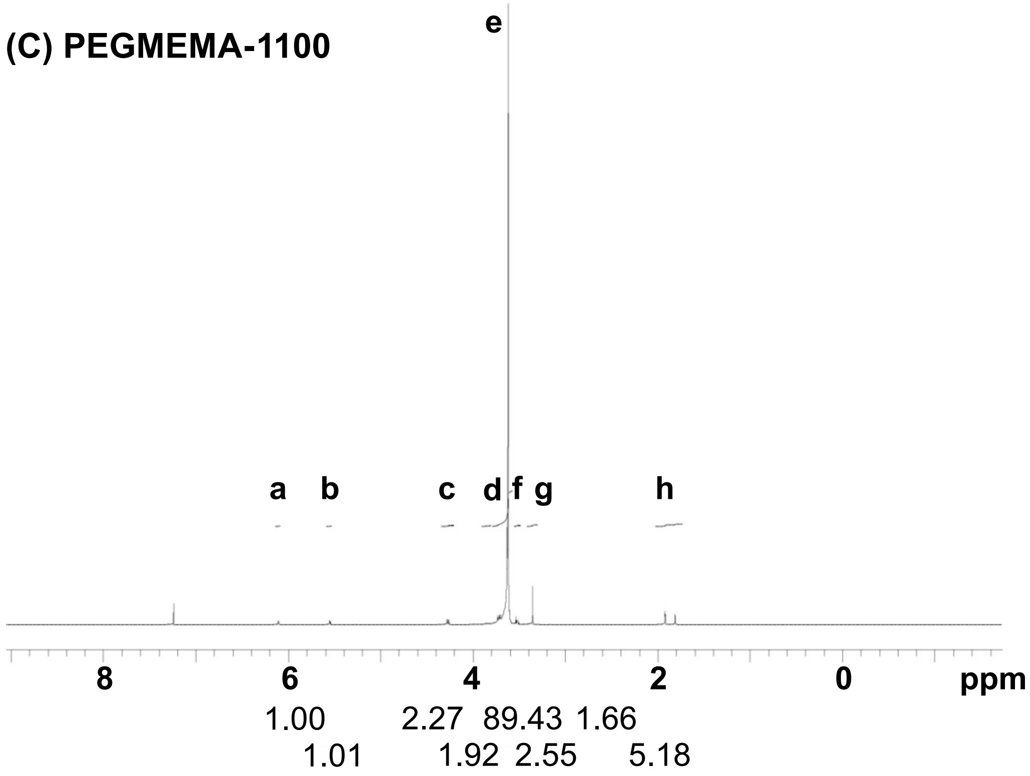

Conclusions

We performed Fresnel calculations to determine the absorption coefficient, *k*, for different films at the wavelengths of interest. We used the *k* values for three homopolymer films, poly(PEGMEMA-300), poly(PEGMEMA-475), and poly(PEGMEMA-1100), at two different IR absorptions, one corresponding to the carbonyl stretch on the monomer unit in the polymer backbone and one corresponding to the ether stretch along the PEG side chain, to enable the determination of the average number of ethylene oxide units per monomer unit.

REFERENCES

REFERENCES

(1) Scholes, C.; Kentish, S.; Stevens, G. *Sep. Purif. Rev.* 2009, 38, 1-44.

(2) Prakash, S.; Kohl, P. A. *J. Power Sources* 2009, 192, 429-434.

(3) Shao, L.; Low, B. T.; Chung, T. S.; Greenberg, A. R. *J. Membr. Sci.* 2009, 327, 18-31.

(4) U.S. Department of Energy, Energy Information Administration. The Impact of Increased Use of Hydrogen on Petroleum Consumption and Carbon Dioxide Emissions. **http://www.eia.doe.gov/oiaf/servicerpt/hydro/pdf/oiafcneaf%2808%2904.pdf** (accessed May 10, 2010).

(5) Molburg, J. C.; Doctor, R. D. *Proc. Ann. Int. Pitt. Coal Conf.* 2003, 20, 1388-1408.

(6) Favre, E. *J. Membr. Sci.* 2007, 294, 50-59.

(7) Lin, H. Q.; Van Wagner, E.; Freeman, B. D.; Toy, L. G.; Gupta, R. P. *Science* 2006, 311, 639-642.

(8) Ockwig, N. W.; Nenoff, T. M. *Chem. Rev.* 2007, 107, 4078-4110.

(9) Perry, E. Process for the Recovery of Hydrogen from Ammonia Purge Gases. U.S. Patent 4,172,885, Oct. 30, 1979.

(10) Kesting, R. E.; Fritzsche, A. K. *Polymeric Gas Separation Membranes*. John Wiley and Sons, Inc.: New York City, NY, 1993.

(11) Matsuyama, H.; Teramoto, M.; Matsui, K.; Kitaura, Y. *J. Appl. Polym. Sci.* 2001, 81, 936-942.

(12) Matsuyama, H.; Teramoto, M.; Sakakura, H.; Iwai, K. *J. Membr. Sci.* 1996, 117, 251-260.

(13) Kim, M.; Park, Y.; Youm, K.; Lee, K. *J. Membr. Sci.* 2004, 245, 79-86.

(14) Noble, R. D.; Pellegrino, J. J.; Grosgogeat, E.; Sperry, D.; Way, J. D. *Sep. Sci. Technol.* 1988, 23, 1595-1609.

(15) Way, J. D.; Noble, R. D. I. Facilitated Transport. In *Membrane Handbook*; Ho, W. S. W.; Sirkar, K. K., Eds.; Van Nostrand Reinhold: New York, 2001; pp 833-866.

(16) Koros, W. J. *J. Polym. Sci., Part B: Polym. Phys.* 1985, 23, 1611-1628.

(17) Zhong, J.; Lin, G.; Wen, W.-Y.; Jones, A. A.; Kelman, S.; Freeman, B. D. *Macromolecules* 2005, 38, 3754-3764.

(18) Bondar, V. I.; Freeman, B. D.; Pinnau, I. *J. Polym. Sci., Part B: Polym. Phys.* 2000, 38, 2051-2062.

(19) Kusuma, V. A.; Matteucci, S.; Freeman, B. D.; Danquah, M. K.; Kalika, D. S. *J. Membr. Sci.* 2009, 341, 84-95.

(20) Patel, N. P.; Miller, A. C.; Spontak, R. J. *Adv. Funct. Mater.* 2004, 14, 699-707.

(21) Kalakkunnath, S.; Kalika, D. S.; Lin, H.; Freeman, B. D. *Macromolecules* 2005, 38, 9679-9687.

(22) Priola, A.; Gozzelino, G.; Ferrero, F.; Malucelli, G. *Polymer* 1993, 34, 3653-3657.

(23) Lin, H.; Freeman, B. D.; Kalakkunnath, S.; Kalika, D. S. *J. Membr. Sci.* 2007, 291, 131-139.

(24) Balachandra, A. M.; Baker, G. L.; Bruening, M. L. *J. Membr. Sci.* 2003, 227, 1-14.

(25) Sun, L.; Baker, G. L.; Bruening, M. L. *Macromolecules* 2005, 38, 2307-2314.

(26) Shah, R. R.; Merreceyes, D.; Husemann, M.; Rees, I.; Abbott, N. L.; Hawker, C. J.; Hedrick, J. L. *Macromolecules* 2000, 33, 597-605.

(27) Zheng, Y.; Bruening, M. L.; Baker, G. L. *Macromolecules* 2007, 40, 8212-8219.

(28) Matyjaszewski, K.; Miller, P. J.; Shukla, N.; Immaraporn, B.; Gelman, A.; Luokala, B. B.; Siclovan, T. M.; Kickelbick, G.; Vallant, T.; Hoffmann, H.; Pakula, T. *Macromolecules* 1999, 32, 8716-8724.

(29) Bao, Z.; Bruening, M. L.; Baker, G. L. *Macromolecules* 2006, 39, 5251-5258.

(30) Kim, J.-B.; Huang, W.; Miller, M. D.; Baker, G. L.; Bruening, M. L. *J. Polym. Sci., Part A: Polym. Chem.* 2003, 41, 386-394.

(31) Cheng, N.; Azzaroni, O.; Moya, S.; Huck, W. T. S. *Macromol. Rapid Commun.* 2006, 27, 1632-1636.

(32) Zhou, F.; Zheng, Z.; Yu, B.; Liu, W.; Huck, W. T. S. *J. Am. Chem. Soc.* 2006, 128, 16253-16258.

(33) Brown, A. A.; Khan, N. S.; Steinbock, L.; Huck, W. T. S. *Eur. Polym. J.* 2005, 41, 1757-1765.

(34) Lad, J.; Harrisson, S.; Haddleton, D. M., *Mechanistic Aspects of Copper-mediated Living Radical Polymerization*. American Chemical Society: Washington, DC, 2003; Vol. 854, p 148-160.

(35) Huang, W.; Kim, J.-B.; Bruening, M. L.; Baker, G. L. *Macromolecules* 2002, 35, 1175-1179.

(36) Wang, X. S.; Armes, S. P. *Macromolecules* 2000, 33, 6640-6647.

(37) Wang, X. S.; Lascelles, S. F.; Jackson, R. A.; Armes, S. P. *Chem. Commun.* 1999, 1817-1818.

(38) Jain, P.; Dai, J.; Grajales, S.; Saha, S.; Baker, G. L.; Bruening, M. L. *Langmuir* 2007, 23, 11360-11365.

(39) Tsarevsky, N. V.; Matyjaszewski, K. *Chem. Rev.* 2007, 107, 2270-2299.

(40) Miyazawa, T.; Ideguchi, Y.; Fukushima, K. *J. Chem. Phys.* 1962, 37, 2764-2776.

(41) Yoshihara, T.; Murahashi, S.; Tadokoro, H. *J. Chem. Phys.* 1964, 41, 2902-2911.

(42) Takahashi, Y.; Tadokoro, H. *Macromolecules* 1973, 6, 672-675.

(43) Li, X.; Hsu, S. L. *J. Polym. Sci., Part B: Polym. Phys.* 1984, 22, 1331-1342.

(44) Schönherr, H.; Frank, C. W. *Macromolecules* 2003, 36, 1188-1198.

(45) Schönherr, H.; Frank, C. W. *Macromolecules* 2003, 36, 1199-1208.

(46) Wang, H. P.; Keum, J. K.; Hiltner, A.; Baer, E.; Freeman, B.; Rozanski, A.; Galeski, A. *Science* 2009, 323, 757-760.

(47) Bitter, J. G. A. *Desalination* 1984, 51, 19-35.

(48) Preston, W. E.; Barlow, J. W.; Paul, D. R. *J. Appl. Polym. Sci.* 1984, 29, 845-852.

(49) Lin, H.; Kai, T.; Freeman, B. D.; Kalakkunnath, S.; Kalika, D. S. *Macromolecules* 2005, 38, 8381-8393.

(50) Lin, H.; Freeman, B. D. *J. Membr. Sci.* 2004, 239, 105-117.

(51) Lin, H.; Freeman, B. D. *Macromolecules* 2005, 38, 8394-8407.

(52) Lin, H.; Freeman, B. D. *J. Mol. Struct.* 2005, 739, 57-74.

(53) Kelman, S. D.; Raharjo, R. D.; Bielawski, C. W.; Freeman, B. D. *Polymer* 2008, 49, 3029-3041.

(54) White, L. S.; Blinka, T. A.; Kloczewski, H. A.; Wang, I.-f. *J. Membr. Sci.* 1995, 103, 73-82.

Chapter Three

The effect of nanoparticles on CO_2-selective polymer membranes

Introduction

Dispersion of nanoparticles in polymers began in 1987 when the Toyota group exchanged the surface cations of montmorillonite with quaternary ammonium surfactants, causing the hydrophilic clay to become compatible with hydrophobic polymers.[1] Compared to traditional inorganic polymer fillers (particle sizes on the micron and larger scale), nanoscale fillers provide significantly higher increases in transition temperatures (glass transition, melting, and critical temperatures), toughness, stiffness, and strength, at lower loadings. A series of studies show that loading of <5 wt% clay nanoparticles in a polymer composite can double the modulus and strength, increase the heat distortion temperature by almost 100˚C, and enhance barrier properties and flame retardancy compared to the pristine polymer.[2-7] Table 3.1 summarizes some of the property enhancements and potential applications available with nanocomposites, and several review articles examined this subject.[8-11]

With respect to the focus of this dissertation on separation membranes, incorporation of high aspect ratio (high anisotropy) nanoparticles into films can enhance barrier properties,[12, 13] or, conversely incorporation of low aspect ratio (low anisotropy) nanoparticles into rigid, high free-volume polymers can enhance permeation and selectivity.[14, 15] These seemingly contradictory effects of nanoparticles on permeation properties stem from the size and shape of the particle filler as well as the rigidity of the polymer chain.

Table 3.1: Selected nanoscale fillers in polymer materials and their corresponding applications. POSS is polyhedral oligomeric silsesquioxane.

Nanofiller	Property enhancement(s)	Application	Refs.
Exfoliated clay	Flame retardancy, gas barriers	Coatings	16-19
SiO_2, MgO	Viscosity modification, permeability	Paint, adhesives, membranes	14, 20-23
Ag	Antimicrobial activity	Coatings	24-31
Carbon nanotubes	Electrical conductivity, charge transport	Electronics, optoelectronics	32-35
CdSe, CdTe, TiO_2	Charge transport	Photovoltaic cells	36-42
Graphene	Electrical conductivity, gas barriers, charge transport	Electronics	43-46
POSS	Improved stability, flammability resistance	Sensors, LEDs	47-50
HfO_2	Refractive index	Photoresists, optics	51, 52
Zeolite, mol. sieve	Permselectivity	Mixed matrix membranes	15

Barrier enhancement occurs when impermeable, long particles in a film create tortuous paths for permeation through the membrane (Figure 3.1). Several models were used to describe penetrant diffusion in composite membranes, some of which consider particle dimension and dispersion.[53, 54]

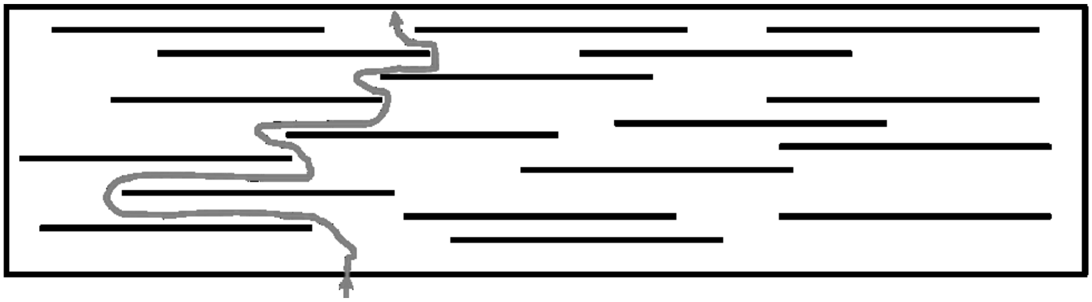

Figure 3.1: Cross-sectional scheme of the tortuous path of a permeant molecule traversing a polymer film containing dispersed, impermeable 2-D nanoparticles.

The most common models rely on the Maxwell equation (Eq. 3.1), which relates the particle loading to the change in permeability.[20] In this equation,

$$P_C = P_M \left(\frac{1-\phi_F}{1+\left(\phi_F / 2\right)} \right) \tag{3.1}$$

P_C and P_M are composite and matrix permeabilities, respectively, and ϕ_F is the filler volume fraction when the filler consists of dispersed, impermeable, spherical particles. Figure 3.2 plots the permeability of the composite as a function of filler loading for a completely impermeable filler and a polymer matrix with a permeability of 1 Barrer.

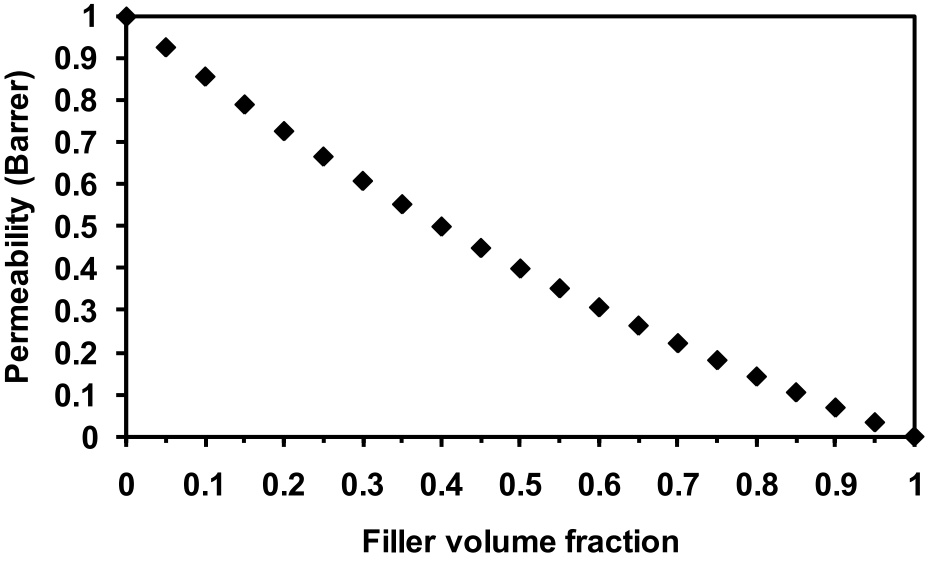

Figure 3.2: Permeability of a composite film as a function of filler volume fraction as predicted by the Maxwell equation. The polymer matrix has a permeability of 1 Barrer, and the filler is impermeable.

The Maxwell model effectively describes permeation through composite membranes that contain traditional fillers, but it does not work for many nanocomposite films. Contradictory to Maxwell's equation, incorporation of nanoparticles into a rigid polymer matrix can increase permeability, probably because the filler disrupts polymer chain packing to increase fractional free volume.[20-23] Freeman and coworkers incorporated MgO nanoparticles into poly(1-trimethylsilyl-1-propyne) to increase CO_2 permeability by a factor of 17 and H_2 permeability by a factor of 40, which decreased CO_2/H_2 selectivity by a factor of 2.[20] In addition to the effects that nanoparticles have on fractional free volume, they may also interfere with polymer crystallization. Inhibition of the room temperature crystallization of poly(ethylene glycol) (PEG) side chains in gas separation membranes was previously reported by cross-linking[55-57] and by copolymerizing two monomers with different PEG chain lengths as described in Chapter 2.[58, 59] Several studies showed that incorporation of montmorillonite, saponite, TiO_2, or Al_2O_3 in bulk PEG inhibits crystallization.[60,

[61] Additionally, PEG crystal morphology changed from spherical to disk-like upon incorporation of 1 wt.% carbon nanotubes.[62]

This chapter examines the effects of titania nanoparticles on polymer films and membranes generated using atom transfer radical polymerization (ATRP) of poly(ethylene glycol) methyl ether methacrylate (PEGMEMA). ATRP is attractive for synthesizing thin (50-500 nm) membrane skins from porous substrates because it affords control over film thickness along with polymer chains with relatively low polydispersity.[63, 64] Moreover, as Chapter 2 demonstrates, poly(PEGMEMA) membranes selectively remove CO_2 from H_2 streams if crystallization of PEG chains can be prevented. This chapter explore whether the presence of TiO_2 nanoparticles in PEGMEMA films can inhibit PEG crystallization to maintain high selectivities in PEGMEMA membranes. The ATRP process for forming membranes on porous alumina substrates, and similar processes on porous polymer supports are discussed in Chapters 1 and 2.

Figure 3.3 shows the method we employ to generate titania in the poly(PEGMEMA) grown from porous supports. The tetraisopropoxytitanate (TPOT) adsorbs into the polymer brush and subsequent exposure to humidity generates a nanocomposite polymer brush with TiO_2 nanoparticles. Yuan and coworkers described the use of polymer brushes as templates to generate titania nanowires,[65] but to our knowledge this is the first example of a nanocomposite polymer brush membrane. (With regard to terminology, composite membranes consist of multiple layers, typically a support layer with large pores and a selective layer. Composite films contain a mixture of two species, in this case polymer and TiO_2. In this chapter the term nanocomposite will only apply to a polymer/TiO_2 film, which may serve as the skin layer of a membrane.)

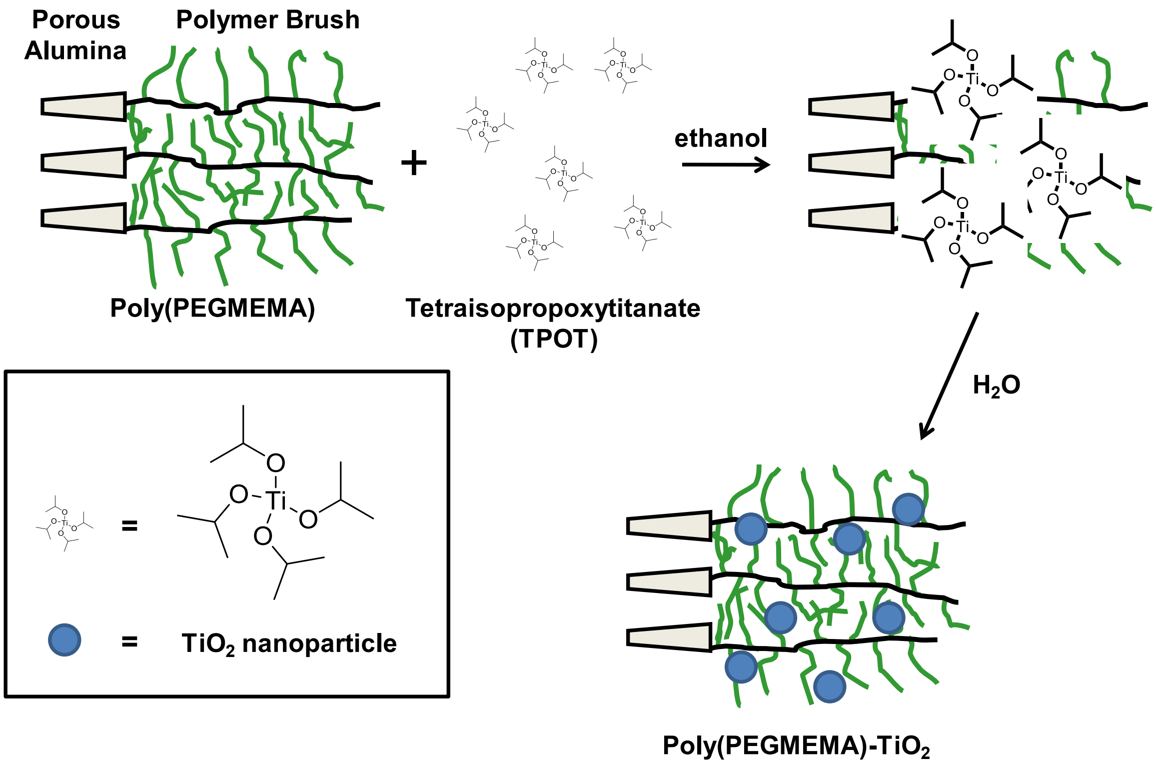

Figure 3.3: Schematic drawing of the formation of nanoparticles to generate a nanocomposite polymer brush.

Experimental

Chemicals. PEGMEMA with M_n = 1,100 Da (PEGMEMA) was obtained from Aldrich and used as received. This monomer contains both 100 ppm 4-methoxyphenol and 300 ppm 2,6-di*tert*-butyl-4-methylphenol as inhibitors. Proton NMR spectra (see Appendix A) show that the average number of ethylene oxide units in PEGMEMA is 23.1. The CuCl, $CuBr_2$, and 1,1,4,7,10,10-hexamethyltriethylenetetramine (HMTETA) were purchased from Aldrich, and deionized water was obtained using a Millipore system (Milli-Q, 18.2 MΩ·cm). Toluene was used as received. Silicon(100) wafers were obtained from NOVA Electronic Materials and sputter-coated with 20 nm of chromium followed by 200 nm of gold by LGA Thin Films (Santa Clara, CA). The porous alumina substrates were Anodisc membrane filters (25 mm disks with 0.02 µm surface pores) purchased from Whatman, and the disulfide, $[Br\text{-}C(CH_3)_2\text{-}COO(CH_2)_{11}S]_2$, and silane, $SiCl(CH_3)_2(CH_2)_{11}OCOC(CH_3)_2Br$, initiators were synthesized as described previously.[66-69]

Polymerization. Porous alumina substrates were initially rinsed with ethanol, dried with N_2, and cleaned with UV/O_3 (Boekel UV-Clean Model 135500) for 15 min. Attachment of a monolayer of the disulfide initiator to gold-coated Si wafers or porous alumina occurred during an overnight immersion of the substrate in an ethanolic solution containing 1 mM $[Br\text{-}C(CH_3)_2\text{-}COO(CH_2)_{11}S]_2$. The resulting sample was rinsed with 5 mL of ethanol and dried in a N_2 stream. Attachment of the silane initiator to alumina occurred during overnight immersion of the uncoated, cleaned porous alumina substrates in a solution containing 8 mM silane in THF. The resulting sample was rinsed with 5 mL THF and dried in a N_2 stream. The two different types of initiator-modified membranes were handled identically in the ensuing polymerization steps.

Following a previous procedure, the catalyst stock solution was prepared by dissolving 0.06 g (0.6 mmol) CuCl and 0.04 g (0.2 mmol) $CuBr_2$ in 30.0 mL of distilled, degassed DMF.[70, 71] The solution was further degassed via three freeze, pump, thaw cycles. In a N_2-filled glove bag, 490 μL (1.8 mmol) of degassed 1,1,4,7,10,10-hexamethyltriethylenetetramine (HMTETA) ligand was added to this solution, which subsequently turned a dark green color during several hours of stirring. During this initial stirring, a small amount of precipitation occurred, but the resulting catalytic activity of the solution remained constant for at least several weeks. The mole ratio of Cu^+:Cu^{2+}:HMTETA was 3:1:9.

The monomer solution, which contained 0.75 M PEGMEMA in water, was initially degassed via three freeze, pump, thaw cycles. The polymerization solution was prepared in a N_2-filled glove bag by combining degassed monomer and catalyst solutions in a 9:1 volume ratio to produce a blue-green solution containing 0.67 M monomer, 2.0 mM CuCl, 0.60 mM CuBr2, and 6.0 mM HMTETA. The initiator-modified membranes or wafers were immersed in the polymerization solution for designated periods of time, and the resulting polymer films were rinsed with 5 mL of water and soaked in water for at least two hours before rinsing with 5 mL of ethanol and drying under a N_2 stream.

Formation of the Polymer-nanoparticle Composite Film. Preparation of the ethanolic TPOT solution at predetermined concentrations was performed in a N_2-filled glove bag. PEGMEMA-modified alumina membranes were immersed in ethanol overnight to ensure that the polymer film was completely swollen, and the membrane was then rinsed with the TPOT solution three times, and immersed in this solution for one hour. After removing the membrane from solution and allowing it to dry in the glove bag for approximately 10 minutes (without rinsing), it was placed in air for several hours to generate TiO_2. Once the hydrolysis of TPOT was completed the membrane could be rinsed with ethanol without changing its properties.

Characterization methods. Reflectance FT-IR spectroscopy was performed using a Nicolet Magna-IR 560 spectrometer with a Pike grazing angle (80°) attachment. A UV/ozone-cleaned, gold-coated Si wafer was used to obtain the background spectrum. Thicknesses of films formed on gold-coated (100) silicon were determined with a rotating analyzer ellipsometer (J.A. Woollam model M44) at an incident angle of 75°. A two-term Cauchy equation was employed to simultaneously fit film thickness as well as the A and B Cauchy constants used to model the wavelength-dependence of the refractive index. Thicknesses were determined at a minimum of three locations on each substrate. Scanning electron microscopy was performed using the JEOL semi-in-lens cold cathode field-emission scanning electron microscope, model JSM-7500F, operating with a r-filter in signal maximum mode. Samples were sputter coated with 5 nm of gold prior to imaging. Cross-polarized microscope images were obtained with a Nikon Optiphot 2-POL polarizing optical microscope equipped with a Mettler FP82HT hot stage and a Sony DXC-151A CCD camera.

Gas Permeation. Mixed-gas permeation experiments were performed by loading the membrane into a custom holder (all connections utilized Swagelok fittings and were tested to ensure that they maintained pressure over a time-scale longer than the experiment) that allowed cross-flow of the feed gas as well as a sweep gas on the permeant side. A backpressure valve was employed to maintain the feed gas pressure, and the feed flow rate was high enough to maintain constant composition at the face of the membrane (the stage-cut, or ratio of permeant flow to feed flow, was < 1%). The feed gas streams used for CO_2 permeances were either pure CO_2 or 20% CO_2, 80% H_2, and the H_2 permeances were measured using a feed gas stream of 80% H_2, 20% CO_2 to simulate an industrially realistic gas stream. The gas flow rates were measured with either an Optiflow 420 electronic soap bubble meter or a manual soap bubble meter. The N_2 sweep gas/permeant stream was connected to an automated six-port injector valve on a Hewlett-Packard 6890 GC equipped with a thermal conductivity detector (TCD) and an Agilent GS-CarbonPLOT capillary column (i.d. = 0.53 mm, length = 30 m, 3 μm coating). The mixed gas permeances as well as pure gas permeances were calculated from GC results using Eq. (3.2),

$$\text{Permeance} = \frac{\chi_{\mathrm{B}} \times \Phi_{\mathrm{N_2}}}{\chi_{\mathrm{N_2}} \times \mathrm{A} \times \Delta p} \qquad (3.2)$$

where χ_B is the mole fraction of a particular permeate gas, B, in the gas mixture injected into the GC column, Φ_{N_2} is the sweep gas flow rate, χ_{N_2} is the mole fraction of N_2 in the gas injected into the GC column, Δp is the transmembrane partial pressure difference for the gas of interest, and A is the membrane area. (Φ_{N_2} / χ_{N_2} is the sum of the permeate and sweep gas flow rate, and χ_{N_2} was determined by subtracting the mole fractions of the permeates from unity. This assumes that the amount of N_2 passing through the membrane was negligible.) The sweep gas flow rate was programmed into a mass flow controller, pressure and area were measured, and the mole fractions were determined from the integrated GC spectra and a calibration curve.

Results and Discussion

Membrane Synthesis. The properties of composite polymer films depend on the filler shape and loading, interfacial interactions between the filler and polymer, and the extent of dispersion of filler particles. Dispersion of the particles in the polymer often requires modification of the nanoparticle surface or addition of compatibilizers to the polymer matrix. For example, dispersion of montmorillonite clays in nylon occurs only after surface exchange of Na^+ ion with anionic surfactants,[1] and blending of maleic anhydride grafted polymers with polyethylene aids in the nanoparticle dispersion in polyethylene.[72, 73] The use of either of these techniques in a polymer film that is less than 500 nm thick poses the added complication that the surface-modifier or compatibilizer might contribute to the film properties.

Incorporation of nanoparticles in a polymer can occur through (1) polymerization of a monomer mixture that contains inorganic nanoparticles, (2) simultaneous condensation of inorganic precursors and polymerization of monomer, or (3) polymerization of monomer to generate a film followed by incorporation of the inorganic nanoparticles in the film.[74] The different approaches have specific benefits and drawbacks for different applications. Typically, method (1) is appropriate when filler particles disperse well in the monomer. The second case is not common because nanoparticle synthesis often occurs at high temperatures and pressures that are incompatible with polymerization. The third method is common when the filler particles disperse in the polymer matrix and is attractive because the nanoparticle and polymer syntheses are independent.

In the case of high-flux gas separation membranes, in addition to the requirement of nanoparticle dispersion, the nanocomposite film must form a defect free skin layers to maintain reverse selectivity. Preliminary experiments suggested that the presence of inorganic precursors or particles in the polymerization solution changes the rate of ATRP and increases the probability of generating defects. Thus, the synthesis strategy that we employ in this work is a variation of (3), generation of the polymer skin prior to incorporation of inorganic precursor into the film and subsequent hydrolysis to produce dispersed nanoparticles, as shown in Figure 3.19.

Inhibition of Crystallization by TiOx Nanoparticles. Immediately after preparation, poly(PEGMEMA) membranes are amorphous and exhibit a CO_2/H_2 selectivity of 13. However, even after one day, crystallization of PEG side chains decreases the CO_2 permeance by >85% and the CO_2/H_2 selectivity by >70%. (The CO_2 flux drops below the detection limit of the GC, which is optimized for H_2 detection.) PEG crystallizes in helices containing seven CH_2CH_2O repeat units in two turns (a 7_2 helix) over a length of 19.3 Å, and helix formation causes a notable splitting of the PEG C-O-C IR band (1150 cm^{-1}) into peaks at 1120 and 1148 cm^{-1} as well as a narrowing of the CH_2 wagging peak at 1360 cm^{-1}.[75, 76] In PEGMEMA films, PEG side chains can also crystallize in this manner, and reflectance infrared spectra taken after storage of films overnight at room temperature reveal the crystallization of homopolymers when PEG chains contain more than 9 CH_2CH_2O repeat units. Figure 3.4 demonstrates the changes in reflectance FTIR spectra that occur upon crystallization of a 44 nm thick poly(PEGMEMA) film.[67, 77, 78]

Table 3.2: Permeation properties of poly(PEGMEMA) membranes and poly(PEGMEMA) membranes containing TiO_2 nanoparticles, poly(PEGMEMA)-TiO_2. Transport measurements were made immediately after membrane preparation and one day later.

Membrane	CO_2/H_2 selectivity	Std. dev.	H_2 permeance ($/cm^3\ cm^{-2}\ s^{-1}\ cmHg^{-1} \times 10^{-8}$)	Std. dev. ($/1 \times 10^{-8}$)	CO_2 permeance ($/cm^3\ cm^{-2}\ s^{-1}\ cmHg^{-1} \times 10^{-8}$)	Std. dev. ($/1 \times 10^{-8}$)
poly(PEGMEMA)	13	2	11.5	0.4	150	20
poly(PEGMEMA) after one day	<2*	-	3.2	0.1	<6*	-
poly(PEGMEMA)-TiO_2	13	1	8.6	1	110	30
poly(PEGMEMA)-TiO_2 after one day	6	1	3.2	0.07	17	2

* The CO_2 signal was below the limit of detection.

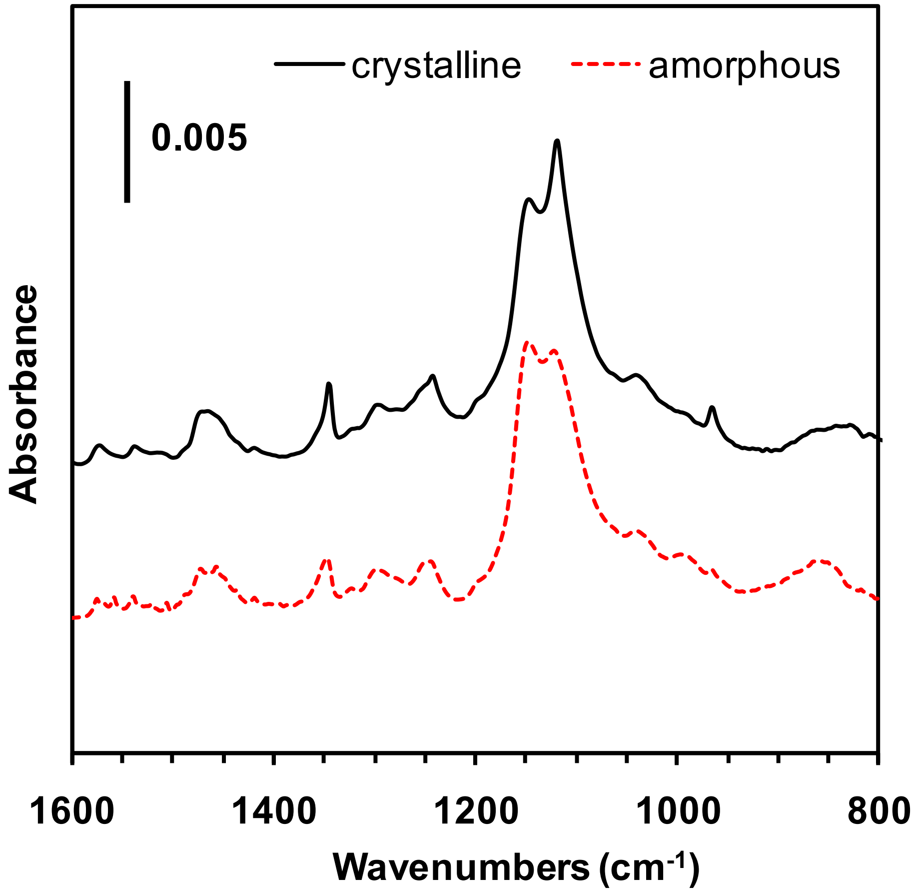

Figure 3.4: Reflectance FTIR of poly(PEGMEMA) immediately after synthesis (dashed red line) and after 24 hours at room temperature (black line).

Cross-polarized microscopy provides an additional method of qualitatively identifying the presence of crystalline polymer because only the crystalline material rotates light prior to its passage through the second polarizer. The appearance of “maltese-cross” patterns in crystallized poly(PEGMEMA) films indicates the formation of circular crystalline domains similar to slices of spherulites. After one day the cross-polarized microscopy image of a poly(PEGMEMA) film is completely covered with Maltese cross patterns, shown in Figure 3.5.

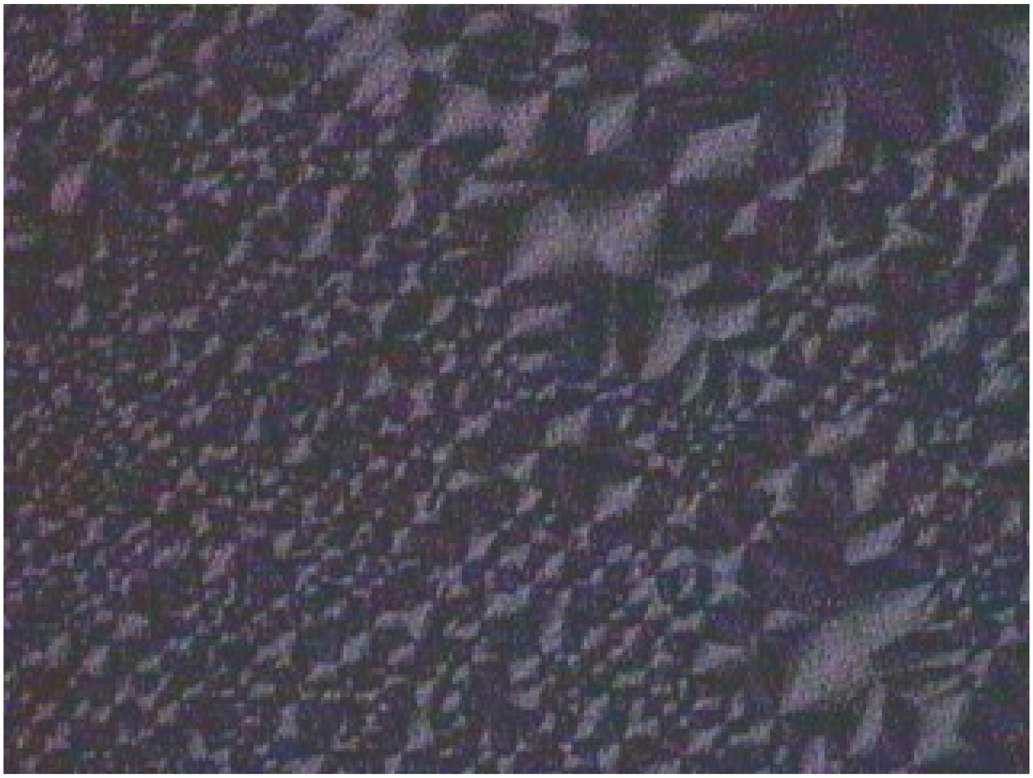

Figure 3.5: Surface of poly(PEGMEMA) after a day at room temperature viewed through a cross-polarized optical microscope.

FTIR spectra of poly(PEGMEMA) and poly(PEGMEMA)-TiO_2 films on gold-coated silicon confirm the presence of TiO_2 nanoparticles in the film after treatment with TPOT and hydrolysis (Figure 3.6). After the film was soaked in THF with TPOT overnight, a broad peak from 880 to 1084 cm^{-1} appears. This stems from Ti-O stretching and confirms the presence of TiO_x nanoparticles.

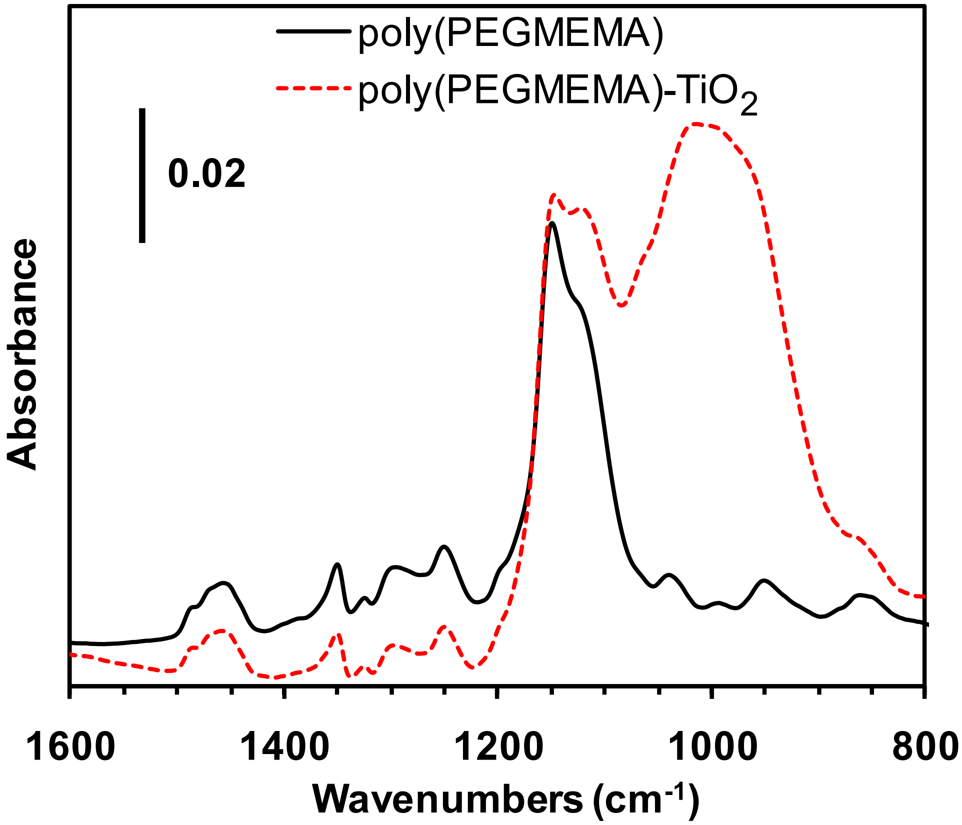

Figure 3.6: Reflectance FTIR spectra of a 44 nm-thick poly(PEGMEMA) film before and after treatment with TPOT to form nanoparticle films. Spectra were obtained immediately after film formation before crystallization could occur.

After crystallization of poly(PEGMEMA) films, the peak height at 1120 cm^{-1} typically increases relative to that at 1148 cm^{-1} (Figure 3.4). Comparison of the spectra in Figure 3.6 shows that the ratio of these two peak heights changes only marginally for poly(PEGMEMA)-TiO_2 films, indicating that the presence of the nanoparticles retards crystallization of PEG chains. (In fact, the small increase in the 1120 cm^{-1} peak relative to the 1148 cm^{-1} peak may be due to further formation of TiO_2 due to hydrolysis.)

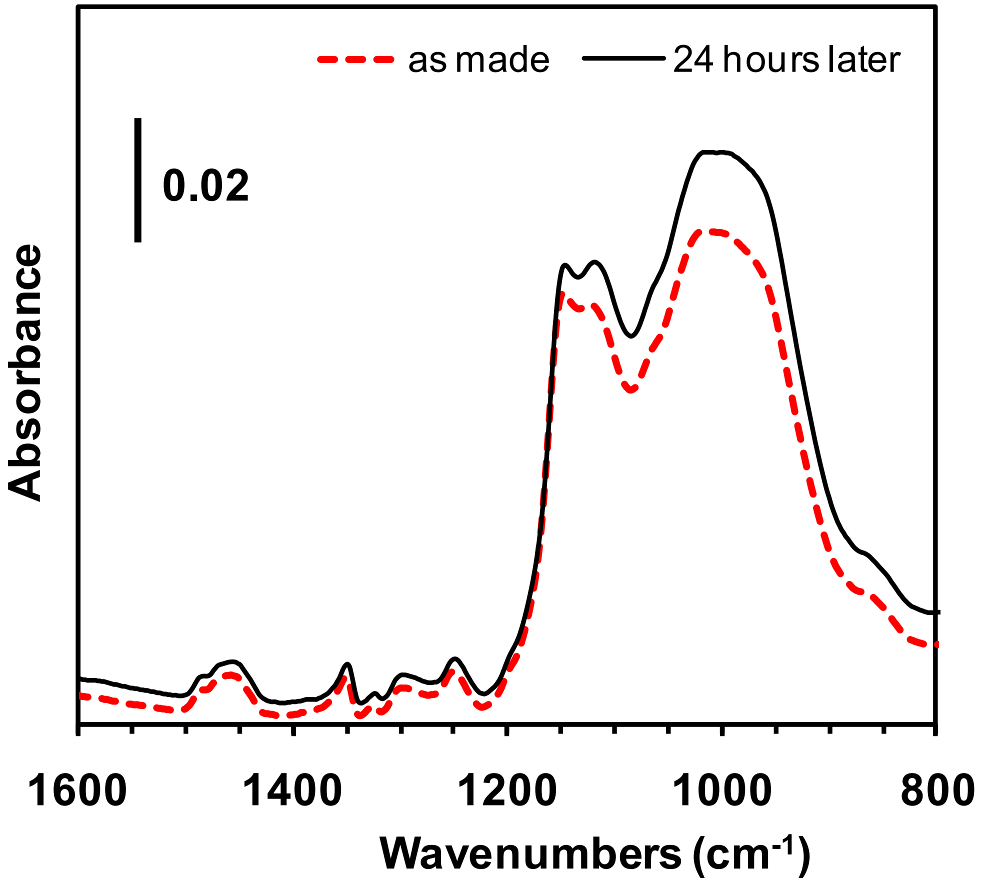

Figure 3.7: Reflectance FTIR spectra of a 44 nm-thick poly(PEGMEMA)-TiO_2 film generated by soaking in 0.1 M TPOT solution overnight. The spectra taken immediately upon removal from the TPOT solution (dashed red) and 24 hours later (black) showed little difference.

Changes in Membrane Permeability due to Nanoparticle Formation. In addition to inhibiting PEG crystallization, the presence of TiO_2 in poly(PEGMEMA) membranes alters their permeability. However, membrane properties vary with the concentration of TPOT used to introduce the Ti. As Figure 3.6 shows, the H_2 and CO_2 permeances of day-old poly(PEGMEMA)-TiO_2 membranes are relatively constant when forming nanoparticles using TPOT concentrations ranging from 0.01 to 0.05 M. Most importantly, the CO_2 permeance is at least 5-fold greater than the corresponding permeance through day-old poly(PEGMEMA), suggesting that the presence of TiO_2 inhibits crystallization. (After one day, the CO_2 permeance of poly(PEGMEMA) membranes is $<6\times10^{-8}$ cm^3 (STP) cm^{-2} s^{-1} $cmHg^{-1}$. This value is <4% of the permeance through a fresh membrane.)

If the TPOT concentration in the modification solution is 0.7 or 1 M, the membrane permeance increases by several orders of magnitude, and selectivity drops to 1. The TPOT treatment and hydrolysis presumably lead to an increase in the free volume until defects form in the presence of high TPOT concentrations.

For nanocomposite films made from deposition solutions containing less than 0.05 M TPOT, the CO_2 permeances of the as-prepared membrane is similar to that of a freshly prepared, untreated poly(PEGMEMA) membrane. After one day of aging, the CO_2 permeance of membranes modified with 0.01 to 0.05 M TPOT declines by 85% due to some crystallization, but the CO_2 permeance of untreated membranes declines by > 96%. Thus low amounts of TiO2 nanoparticles are likely insufficient to inhibit crystallization.

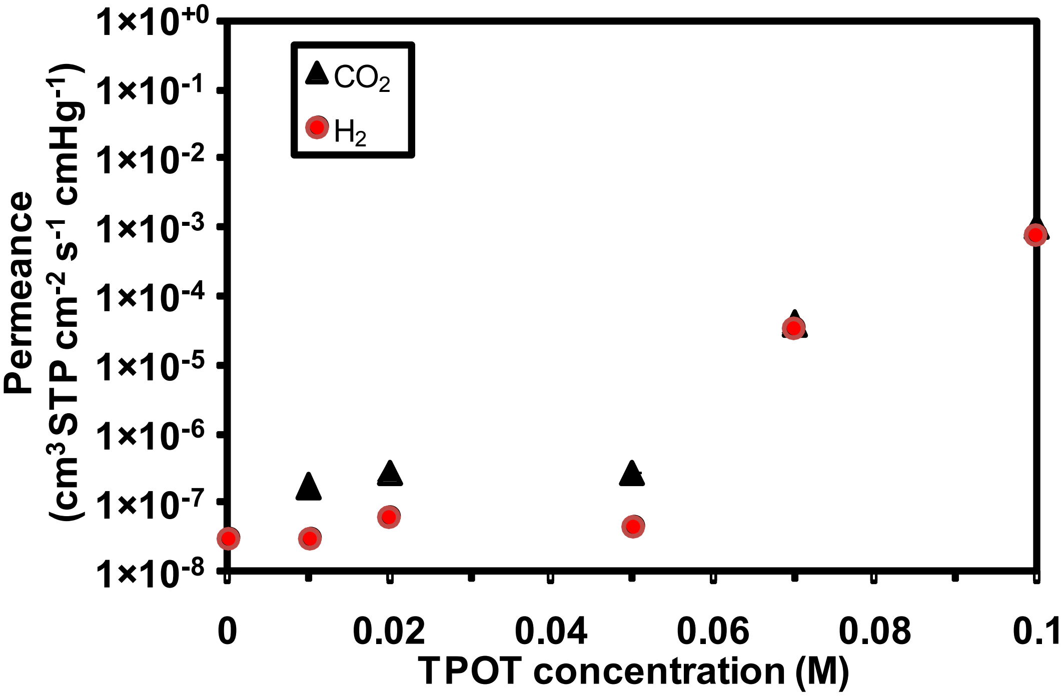

Figure 3.8: Permeances of poly(PEGMEMA)-TiO_2 membranes as a function of the TPOT concentration employed for nanoparticle formation. The measurements were taken after membrane aging overnight at room temperature. The black triangles correspond to CO_2 and the red circles to H_2. (The CO_2 permeance of the unmodified membrane, 0 M TPOT, was below the detection limit of the system.)

The initial CO_2/H_2 selectivity was 12-13 for all the membranes prior to crystallization or treatment with TPOT. Immediately after formation of TiO_2 the membrane selectivity remains at values of 12-13 for samples made using a modification solution containing less than 0.05 M TPOT. In contrast, for the membranes modified using solutions containing 0.07 and 1 M TPOT, the CO_2/H_2 selectivities decrease to ~1 immediately after TPOT treatment, showing the formation of defects. Thus, effective membrane modification is limited to solutions containing ≤0.05 M TPOT.

After storage at room temperature for one day, the selectivity of the pristine polymer drops to less than 1 due to crystallization, but the TiO_2-loaded nanocomposites maintain selectivities of around 6 if the TPOT concentration in the modification solution is 0.05 M or less (Figure 3.8).

Thus the TiO_2 nanoparticles likely reduce the rate of crystallization, although they may not prevent it. Longer term studies are needed to address whether incorporation of nanoparticles can truly prevent most crystallization to retain some level membrane selectivity.

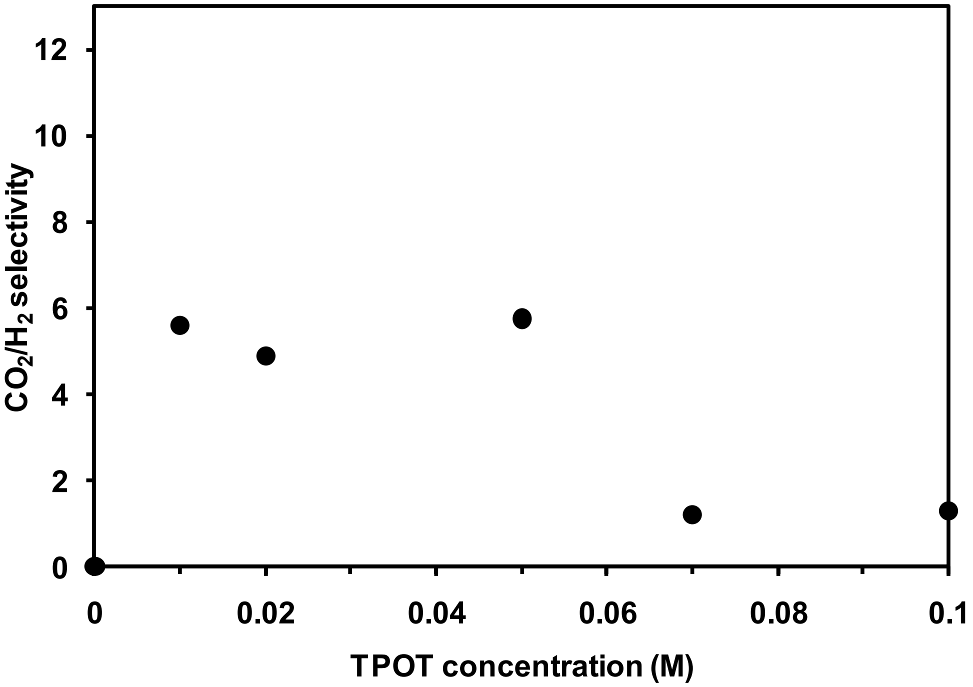

Figure 3.9: CO_2/H_2 selectivities of poly(PEGMEMA-1100) membranes as a function of the TPOT concentration used to modify the membranes prior to aging for one day at room temperature.

Conclusions

The PEG side chains in poly(PEGMEMA) films grown from porous alumina provide a high initial CO_2/H_2 selectivity of 12-13, but crystallization in less than a day at room temperature results in a drastic reduction of permeance and selectivity. The incorporation of TiO_2 nanoparticles frustrates some of the crystallization and allows the membrane to retain CO_2/H_2 selectivities of around 6 while maintaining the permeability typical of an amorphous film. With a TPOT deposition solution containing 0.01 M - 0.05 M TPOT, the loading of TiO_2 nanoparticles was high enough to stop some crystallization and low enough to avoid the formation of defects that negate selectivity.

REFERENCES

REFERENCES

(1) Fukushima, Y.; Inagaki, S. *Journal of Inclusion Phenomena* **1987,** 5, 473-482.

(2) Usuki, A.; Kojima, Y.; Kawasumi, M.; Okada, A.; Fukushima, Y.; Kurauchi, T.; Kamigaito, O. *J. Mater. Res.* **1993,** 8, 1179-1184.

(3) Usuki, A.; Kawasumi, M.; Kojima, Y.; Okada, A.; Kurauchi, T.; Kamigaito, O. *J. Mater. Res.* **1993,** 8, 1174-1178.

(4) Kojima, Y.; Usuki, A.; Kawasumi, M.; Okada, A.; Kurauchi, T.; Kamigaito, O. *J. Poly. Sci. Part A-Poly. Chem.* **1993,** 31, 983-986.

(5) Kojima, Y.; Usuki, A.; Kawasumi, M.; Okada, A.; Fukushima, Y.; Kurauchi, T.; Kamigaito, O. *J. Mater. Res.* **1993,** 8, 1185-1189.

(6) Kojima, Y.; Fukumori, K.; Usuki, A.; Okada, A.; Kurauchi, T. *J. Mater. Sci. Lett.* **1993,** 12, 889-890.

(7) Gilman, J. W.; Kashiwagi, T.; Lichtenhan, J. D. *Sampe Journal* **1997,** 33, 40-46.

(8) Paul, D. R.; Robeson, L. M. *Polymer* **2008,** 49, 3187-3204.

(9) Powell, C. E.; Beall, G. W. *Current Opinion in Solid State & Materials Science* **2006,** 10, 73-80.

(10) Ray, S. S.; Okamoto, M. *Prog. Polym. Sci.* **2003,** 28, 1539-1641.

(11) Pinnavaia, T.; Beall, G., *Polymer–clay Nanocomposites*. John Wiley & Sons Ltd.: 2000.

(12) Kim, S.; Kim, S. *J. Appl. Polym. Sci.* **2007,** 103, 1262–1271.

(13) Choi, W.; Kim, H.; Yoon, K.; Kwon, O.; Hwang, C. *J. Appl. Polym. Sci.* **2006,** 100, 4875–4879

(14) Merkel, T.; Freeman, B.; Spontak, R.; He, Z.; Pinnau, I.; Meakin, P. *Science* **2002,** 296, 519–522.

(15) Zimmerman, C.; Singh, A.; Koros, W. *J. Membr. Sci.* **1997,** 137, 145–154.

(16) Manias, E.; Touny, A.; Wu, L.; Strawhecker, K.; Lu, B.; Chung, T. C. *Chem. Mater.* **2001,** 13, 3516-3523.

(17) Morgan, A. B. *Polym. Adv. Technol.* **2006,** 17, 206-217.

(18) Peila, R.; Malucelli, G.; Lazzari, M.; Priola, A. *Polym. Eng. Sci.* 50, 1400-1407.

(19) Alexandre, B.; Colasse, L.; Langevin, D.; Mederic, P.; Aubry, T.; Chappey, C.; Marais, S. *J. Phys. Chem. B* 114, 8827-8837.

(20) Matteucci, S.; Kusuma, V. A.; Kelman, S. D.; Freeman, B. D. *Polymer* **2008,** 49, 1659-1675.

(21) Matteucci, S.; Kusuma, V. A.; Sanders, D.; Swinnea, S.; Freeman, B. D. *J. Membr. Sci.* **2008,** 307, 196-217.

(22) Matteucci, S.; Kusuma, V. A.; Swinnea, S.; Freeman, B. D. *Polymer* **2008,** 49, 757-773.

(23) Matteucci, S.; Raharjo, R. D.; Kusuma, V. A.; Swinnea, S.; Freeman, B. D. *Macromolecules* **2008,** 41, 2144-2156.

(24) Bryaskova, R.; Pencheva, D.; Kale, G. M.; Lad, U.; Kantardjiev, T. *J. Colloid Interface Sci.* **2010,** 349, 77-85.

(25) Dai, J.; Bruening, M. L. *Nano Lett.* **2002,** 2, 497-501.

(26) Gray, J. E.; Norton, P. R.; Alnouno, R.; Marolda, C. L.; Valvano, M. A.; Griffiths, K. *Biomaterials* **2003,** 24, 2759-2765.

(27) Grunlan, J. C.; Choi, J. K.; Lin, A. *Biomacromolecules* **2005,** 6, 1149-1153.

(28) Ignatova, M.; Labaye, D.; Lenoir, S.; Strivay, D.; Jerome, R.; Jerome, C. *Langmuir* **2003,** 19, 8971-8979.

(29) Jansen, B.; Kohnen, W. *J. Ind. Microbiol. Biotechnol.* **1995,** 15, 391-396.

(30) Lee, H. J.; Yeo, S. Y.; Jeong, S. H. *J. Mater. Sci.* **2003,** 38, 2199-2204.

(31) Shi, Z.; Neoh, K. G.; Kang, E. T. *Langmuir* **2004,** 20, 6847-6852.

(32) Collins, P. G.; Bradley, K.; Ishigami, M.; Zettl, A. *Science* **2000,** 287, 1801-1804.

(33) Huang, Y.; Duan, X. F.; Cui, Y.; Lauhon, L. J.; Kim, K. H.; Lieber, C. M. *Science* **2001,** 294, 1313-1317.

(34) Yao, Z.; Postma, H. W. C.; Balents, L.; Dekker, C. *Nature* **1999,** 402, 273-276.

(35) Poncharal, P.; Wang, Z. L.; Ugarte, D.; de Heer, W. A. *Science* **1999,** 283, 1513-1516.

(36) Kwong, C. Y.; Choy, W. C. H.; Djurisic, A. B.; Chui, P. C.; Cheng, K. W.; Chan, W. K. *Nanotechnology* **2004,** 15, 1156-1161.

(37) Katsaros, G.; Stergiopoulos, T.; Arabatzis, I. M.; Papadokostaki, K. G.; Falaras, P. *Journal of Photochemistry and Photobiology a-Chemistry* **2002,** 149, 191-198.

(38) He, J. A.; Mosurkal, R.; Samuelson, L. A.; Li, L.; Kumar, J. *Langmuir* **2003,** 19, 2169-2174.

(39) Huynh, W. U.; Dittmer, J. J.; Alivisatos, A. P. *Science* **2002,** 295, 2425-2427.

(40) Nozik, A. J. *Physica E-Low-Dimensional Systems & Nanostructures* **2002,** 14, 115-120.

(41) Leschkies, K. S.; Divakar, R.; Basu, J.; Enache-Pommer, E.; Boercker, J. E.; Carter, C. B.; Kortshagen, U. R.; Norris, D. J.; Aydil, E. S. *Nano Lett.* **2007,** 7, 1793-1798.

(42) Levy-Clement, C.; Tena-Zaera, R.; Ryan, M. A.; Katty, A.; Hodes, G. *Advanced Materials* **2005,** 17, 1512-1515.

(43) Kim, H.; Macosko, C. W. *Polymer* **2009,** 50, 3797-3809.

(44) Kim, H.; Macosko, C. W. *Macromolecules* **2008,** 41, 3317-3327.

(45) Verdejo, R.; Barroso-Bujans, F.; Rodriguez-Perez, M. A.; de Saja, J. A.; Lopez-Manchado, M. A. *J. Mater. Chem.* **2008,** 18, 2221-2226.

(46) Raghu, A. V.; Lee, Y. R.; Jeong, H. M.; Shin, C. M. *Macromol. Chem. Phys.* **2008,** 209, 2487-2493.

(47) Phillips, S. H.; Haddad, T. S.; Tomczak, S. J. *Current Opinion in Solid State & Materials Science* **2004,** 8, 21-29.

(48) Zheng, L.; Farris, R. J.; Coughlin, E. B. *Macromolecules* **2001,** 34, 8034-8039.

(49) Jeon, H. G.; Mather, P. T.; Haddad, T. S. *Polym. Int.* **2000,** 49, 453-457.

(50) Waddon, A. J.; Coughlin, E. B. *Chem. Mater.* **2003,** 15, 4555-4561.

(51) Bae, W. J.; Trikeriotis, M.; Sha, J.; Schwartz, E. L.; Rodriguez, R.; Zimmerman, P.; Giannelis, E. P.; Ober, C. K. *J. Mater. Chem.* **2010,** 20, 5186-5189.

(52) Zimmerman, P. A.; Rice, B.; Rodriguez, R.; Zettel, M. F.; Trikeriotis, M.; Wang, D. Y.; Yi, Y.; Bae, W. J.; Ober, C. K.; Giannelis, E. P. *J. Photopolym. Sci. Technol.* **2008,** 21, 621-629.

(53) Xue, L.; Borodin, O.; Smith, G. D. *J. Membr. Sci.* **2006,** 286, 293–300.

(54) Barrer, R. M.; Barrie, J. A.; Rogers, M. G. *J. Polym. Sci. A: Polym. Chem.* **1963,** 1, 2565–2586.

(55) Kalakkunnath, S.; Kalika, D. S.; Lin, H.; Freeman, B. D. *Macromolecules* **2005,** 38, 9679-9687.

(56) Patel, N. P.; Miller, A. C.; Spontak, R. J. *Adv. Funct. Mater.* **2004,** 14, 699-707.

(57) Priola, A.; Gozzelino, G.; Ferrero, F.; Malucelli, G. *Polymer* **1993,** 34, 3653-3657.

(58) Grajales, S. T.; Dong, X.; Zheng, Y.; Baker, G. L.; Bruening, M. L. *Chem. Mater.* **2010,** 22, 4026-4033.

(59) Grajales, S. T.; Dong, X.; Zheng, Y.; Baker, G. L.; Bruening, M. L. *Polymer Preprints* **2009,** 50, 757.

(60) Loyens, W.; Jannasch, P.; Maurer, F. H. J. *Polymer* **2005,** 46, 915-928.

(61) Croce, F.; Appetecchi, G. B.; Persi, L.; Scrosati, B. *Nature* **1998,** 394, 456-458.

(62) Jin, J.; Song, M.; Pan, F. *Thermochim. Acta* **2007,** 456, 25-31.

(63) Balachandra, A. M.; Baker, G. L.; Bruening, M. L. *J. Membr. Sci.* **2003,** 227, 1-14.

(64) Sun, L.; Baker, G. L.; Bruening, M. L. *Macromolecules* **2005,** 38, 2307-2314.

(65) Yuan, J.; Lu, Y.; FSchacher, F.; Lunkenbein, T.; Weiss, S.; Schmalz, H.; Muller, A. H. E. *Chem. Mater.* **2009,** 21, 4146-4154.

(66) Shah, R. R.; Merreceyes, D.; Husemann, M.; Rees, I.; Abbott, N. L.; Hawker, C. J.; Hedrick, J. L. *Macromolecules* **2000,** 33, 597-605.

(67) Zheng, Y.; Bruening, M. L.; Baker, G. L. *Macromolecules* **2007,** 40, 8212-8219.

(68) Matyjaszewski, K.; Miller, P. J.; Shukla, N.; Immaraporn, B.; Gelman, A.; Luokala, B. B.; Siclovan, T. M.; Kickelbick, G.; Vallant, T.; Hoffmann, H.; Pakula, T. *Macromolecules* **1999,** 32, 8716-8724.

(69) Bao, Z.; Bruening, M. L.; Baker, G. L. *Macromolecules* **2006,** 39, 5251-5258.

(70) Kim, J.-B.; Huang, W.; Miller, M. D.; Baker, G. L.; Bruening, M. L. *J. Polym. Sci., Part A: Polym. Chem.* **2003,** 41, 386-394.

(71) Cheng, N.; Azzaroni, O.; Moya, S.; Huck, W. T. S. *Macromol. Rapid Commun.* **2006,** 27, 1632-1636.

(72) Chiu, F. C.; Yen, H. Z.; Chen, C. C. *Polym. Test.* 29, 706-716.

(73) Koo, C. M.; Ham, H. T.; Kim, S. O.; Wang, K. H.; Chung, I. J.; Kim, D.-C.; Zin, W.-C. *Macromolecules* **2002,** 35, 5116-5122.

(74) Azzaroni, O.; Brown, A. A.; Cheng, N.; Wei, A.; Jonas, A. M.; Huck, W. T. S. *J. Mater. Chem.* **2007,** 17, 3433-3439.

(75) Miyazawa, T.; Ideguchi, Y.; Fukushima, K. *J. Chem. Phys.* **1962,** 37, 2764-2776.

(76) Yoshihara, T.; Murahashi, S.; Tadokoro, H. *J. Chem. Phys.* **1964,** 41, 2902-2911.

(77) Wang, H. P.; Keum, J. K.; Hiltner, A.; Baer, E.; Freeman, B.; Rozanski, A.; Galeski, A. *Science* **2009,** 323, 757-760.

(78) Li, X.; Hsu, S. L. *J. Polym. Sci., Part B: Polym. Phys.* **1984,** 22, 1331-1342.

Chapter Four

Guanidine-Based Antifouling, Ion-selective Membranes

This work was performed in collaboration with Dr. Viktoriya Konovalova of the Membrane Research Center at the Kiev-Mohyla Academy where she measured flux, solute rejections and antimicrobial activity.

Introduction

Reverse osmosis and nanofiltration are now commercially viable methods for desalination and water softening, respectively.[1, 2] Other membrane processes such as ultrafiltration and microfiltration have also emerged as standard methods in municipal water treatment.[3] Nevertheless, the formation of foulant layers on membrane surfaces is an ubiquitous problem in membrane-based water purification, and fouling reduction and remediation procedures add significant costs to these operations.[4] Biofouling, fouling due to microorganisms, is particularly problematic because even a few bacteria on a surface can multiply and cause significant decreases in membrane permeability.[5] The initial step in biofouling, cell adhesion, depends on substrate properties such as roughness,[6-8] topography,[9] free energy,[10, 11] and polymer composition.[12-14] However, even on carefully crafted surfaces, deposition of extracellular polysaccharides eventually allows attachment of microorgranisms.[5]

Existing measures to combat membrane fouling include pretreatment of the feed solution,[15, 16] intermittent membrane cleaning,[17, 18] incorporation of antibacterial metal particles in membranes,[19-21] and surface modification of membranes with ammonium groups.[22-26] Surface modification can in principle occur in existing membranes and avoid the need to reengineer a process. Of particular interest to this work, layer-by-layer adsorption of polycations and polyanions (Scheme 4.1) provides a simple, well-controlled method for membrane modification,[27-33] and adsorption of polycationic biocidal polymers, e.g. polyguanidines and polybiguanidines, creates films with antibacterial properties. These polycations exhibit low toxicity to humans along with high antibacterial activity in aqueous solutions[34,35] and on cotton.[36]

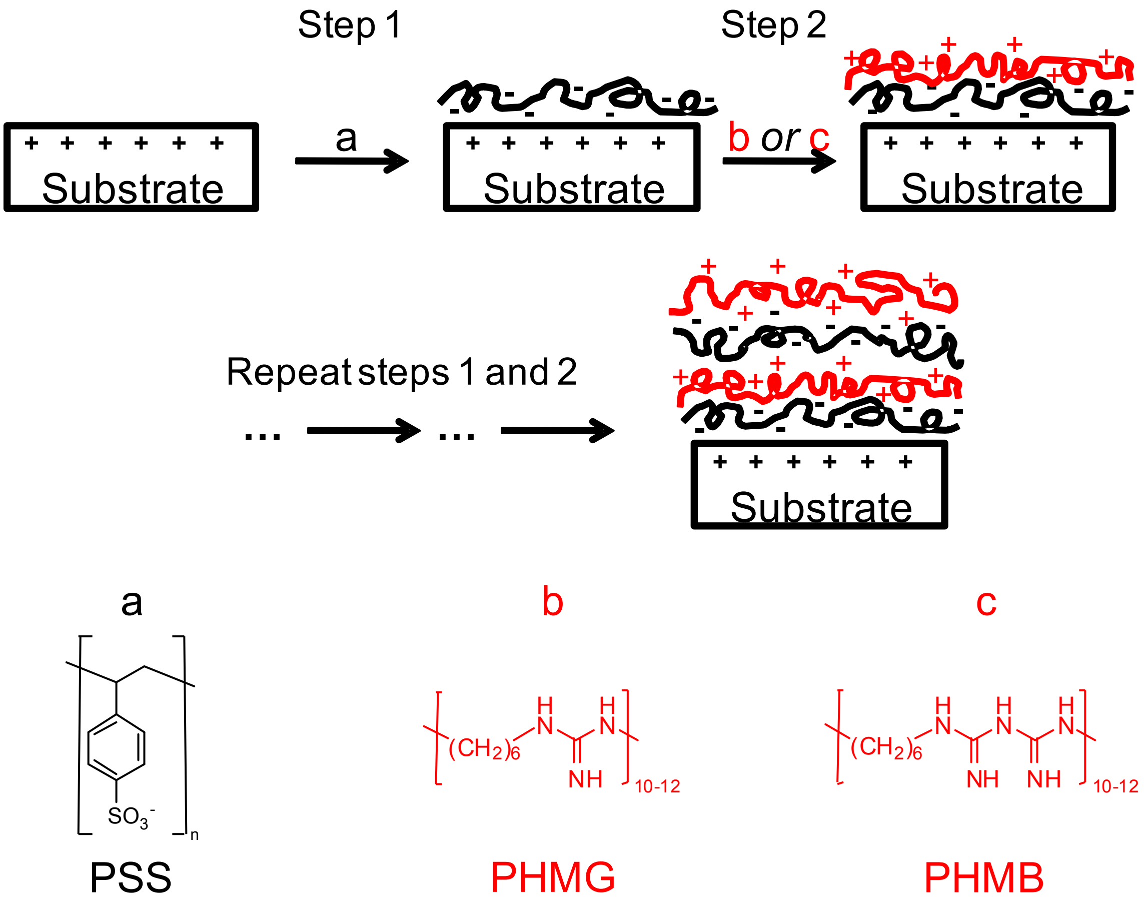

Scheme 4.1: Preparation of an antibacterial polyelectrolyte multilayer film using (a) poly(styrenesulfonate) (PSS), and (b) poly(hexamethylene guanidine) (PHMG) or (c) poly(hexamethylene biguanidine) (PHMB).

Scheme 4.2 shows the proposed mechanism by which PHMG kills bacteria.[37] Interactions between guanidinium groups and acidic phospholipids lead to aggregation of these phospholipids and eventually membrane deformation and cell death.[37-39] The presence of neighboring guanidinium groups in the PHMB repeat unit makes this

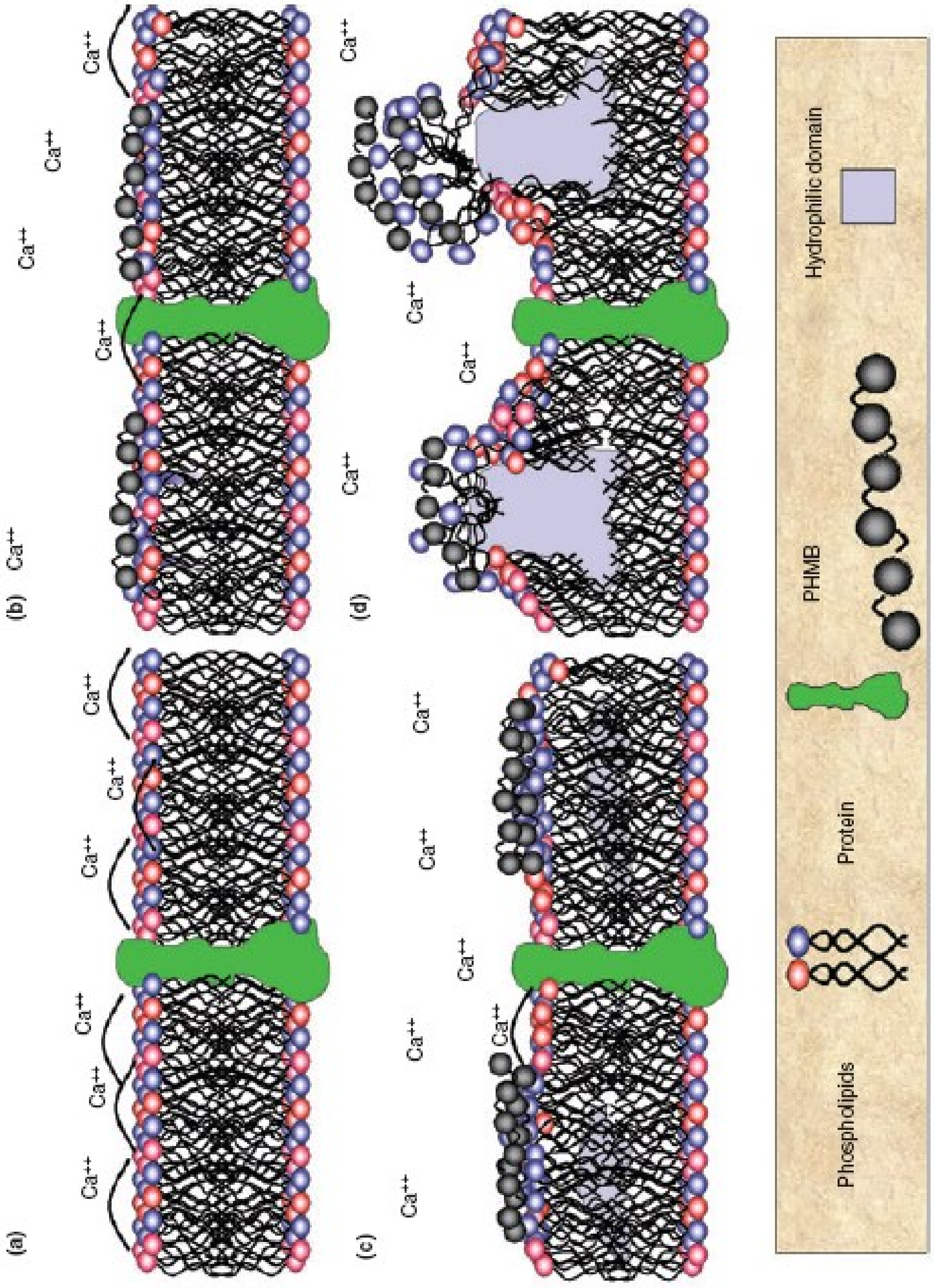

Scheme 4.2: Mechanism of PHMB antibacterial action. (a) The healthy bacterial membrane contains a mixture of acidic and neutral phospholipids. (b) PHMB adsorbs to the bacterial membranes through interaction with phospholipds. (c) The affinity of PHMB for acidic phospholipids leads to sequestration of these phospholipids under the polymer. (d) Lipid sequestration leads to membrane deformation and eventually cellular leakage and death. Reproduced with permission from [37]

polymer potentially more antibacterial than PHMG. The minimum solution concentration to reach an antibacterial activity of 100% is 5.0 ppm for PHMG and 1.25 ppm for PHMB.[38, 40-42]

Considering the need for antifouling coatings in membrane applications[43] and the previously reported ion-selective transport through polyelectrolyte multilayer membranes,[32, 44] this chapter explores the potential application of guanidine-containing polyelectrolyte multilayers as membrane skins that resist biofouling and provide selective ion transport. We report the influence of the number of PSS/PHMG or PSS/PHMB bilayers on surface charge, ion rejections, and antibacterial properties.

Materials and Method

Preparation of films. Poly(sodium 4-styrenesulfonate) (PSS, Mw = 70,000 Da) was purchased from Sigma-Aldrich, and poly(hexamethylene biguanidine) (PHMB, Vantocil IB) was used as received from Arch Biocides. The poly(hexamethylene guanidine), PHMG, was synthesized by Dr. Viktorya Konovalova according to a previously published procedure.[40, 45] Deionized water (Millipore purification system, 18.2 MΩcm) was used for membrane rinsing and preparation of the polyelectrolyte solutions. PES membranes with a molecular-weight cutoff of 50 kDa were kindly provided by Pall Corporation (Port Washington, NY) and PES membranes with a molecular-weight cutoff of 20 kDa were purchased from Microdyn-Nadir. All PES membranes were initially soaked in 0.1 M NaOH for 1 h, then soaked in DI water for 24 h and rinsed with DI water. For ellipsometry and reflectance FTIR studies, films were formed on Si wafers that were sputter-coated with 200 nm of Al.

PSS deposition solutions contained 0.02 M PSS (polymer concentrations are always given with respect to the repeating unit) in 0.5 M NaCl, and the pH of this solution was either left at 5.7 or adjusted to 3.4 with 0.1 M HCl. The poly(hexamethylene guanidine) deposition solution contained 3.0 % (w/v) PHMG (0.169 M) in 0.5 M NaCl, and the pH of this solution was either left at 7.4 or adjusted to 2.4 with 0.1 M HCl. PHMB was adsorbed from a solution containing 3% (w/v) PHMB (0.15 M) in 0.5 M NaCl at an unadjusted pH of 5.4.

Formation of polyelectrolyte multilayer films involved alternating immersions of the substrate in PSS and PHMG or PHMB solutions with a 1-min rinse with deionized water after adsorption of each polymer. The adsorption time was 10 min. for the initial PSS layer and 5 min for each subsequent layer.

Zeta potential values for coated PES membranes were calculated from streaming potentials measured using an Anton Paar ElectroKinetic Analyzer. Reflectance FT-IR spectroscopy of films on Al-coated Si was performed using a Nicolet Magna-IR 560 spectrometer with a Pike grazing angle (80°) attachment. A UV/ozone cleaned aluminum-coated wafer served as the background sample. Thicknesses of films formed on the coated wafers were determined with a rotating analyzer ellipsometer (J.A. Woollam model M44) at an incident angle of 75°. The data were fit to a model of an Al substrate covered by an Al_2O_3 layer and then the polymeric film. Thicknesses were determined at a minimum of three locations on each aluminum-coated substrate.

Characterization of solute rejection. The following flux and solute rejection experiments were performed by Dr. Konovalova. Pure water trans-membrane flux and solute rejection were determined using an Amicon 8050 cylindrical dead-end filtration cell (Millipore) at room temperature. The operating pressure was 300 kPa. Solute rejection was determined with solutions containing 0.01 M NaCl or $MgCl_2$, and conductivity measurements were used to determine electrolyte concentrations in feed and permeate solutions. Solute rejection, R, was calculated using Eq. (4.1),

$$R(\%) = \left(1 - \frac{C_p}{C_f}\right) \times 100\% \tag{4.1}$$

where C_f and C_p are solute concentrations in the feed and permeate, respectively.

Evaluation of membrane antimicrobial activity. Dr. Konovalova performed the antibacterial studies described in this chapter. Future studies should be performed on 50 kDa PES membranes to verify the findings. The microorganisms were gram-negative Escherichia coli BE strains from the Ukrainian Collection of Microorganisms. The bacteria were cultivated in broth overnight in an incubator shaker (250 rpm) at 37 °C, and the suspension was then diluted (1 mL in 100 mL) with fresh, autoclaved broth, and further cultivated to mid-logarithmic phase as defined by an optical density of 0.6-0.8 at a wavelength of 600 nm. The number of bacterial cells was then adjusted to approximately 5×10^8 cells per mL (optical density at 600 nm of ~0.5) in broth.[46] Cells were collected by centrifugation (10 min, 3000 rpm), and then resuspended in sterile, deionized water.

To test the antibacterial activity of modified and bare membranes, 3 mL of this bacteria suspension was immediately filtered through a membrane in an Amicon dead-end filtration cell at room temperature and 300 kPa. The membrane pore size is less than the dimensions of the cell, so all bacterium should be deposited on the face of the membrane after filtration. After filtration, the membranes were incubated on Endo Agar medium for 24 hours at 30^{o}C.

Bactericidal activity, η, was calculated as follows:

$$\eta = \frac{N_1 - N_2}{N_1} \times 100\% \tag{1.49}$$

where N_1 and N_2 are the numbers of viable colonies on control and modified membranes, respectively. Optical microscopy was used to count the bacterial colonies, and the control membranes were unmodified PES.

Results

Membrane Surface Characterization. The goal of this work is to use layer-by-layer adsorption of PSS/PHMG or PSS/PHMB films to create selective, highly permeable nanofiltration membranes that resist bacterial growth. The first step in these studies is characterization of the adsorption of PSS/PHMG or PSS/PHMB films on model substrates. Reflectance FTIR spectra of these films deposited on aluminum-coated silicon wafers show strong absorption bands in the 1500-1700 cm^{-1}, 1100-1250 cm^{-1}, and 2800-3500 cm^{-1} regions (Figures 4.1, 4.2, and 4.4). Table 4.1 lists the polyelectrolyte vibrational modes that give rise to these absorbances.

Table 4.1: Strong infrared absorption modes for PSS/PHMG and PSS/PHMB films.

Wavenumbers (cm^{-1})	Absorption mode	Functional group	Ref.
3320	v sym(H-N-H)	guanidine	47
3180	v (N-H)	guanidine	47
2800 - 3000	v asym and sym (H-N$^+$-H)	guanidine	47
1580 - 1690	(N—C=N) NH and NH$_2$ deformation	guanidine	47
1550 - 1640	v (asym) (NCN)	guanidine	48
1588	v (C=N)	guanidine	48
1550	v (C=N)	biguanidine	48
1400 - 1500	v (C-N) + δ (N-H)	guanidine	48
1120 - 1250	v (OSO)	sulfonate	48
1009	Ring stretch	Monosubstituted ring	48

Figures 4.1 and 4.2 show the reflectance FTIR spectra of PSS/PHMG films from 3600-2800 and 1800-1000 cm^{-1}, respectively. Absorbances increase regularly, suggesting controlled layer-by-layer growth of these films. Figure 4.3 shows peak height versus the number of PSS/PHMG bilayers for two specific IR absorbances, 1643 cm^{-1} and 1009 cm^{-1}, that are characteristic of PHMG and PSS, respectively.

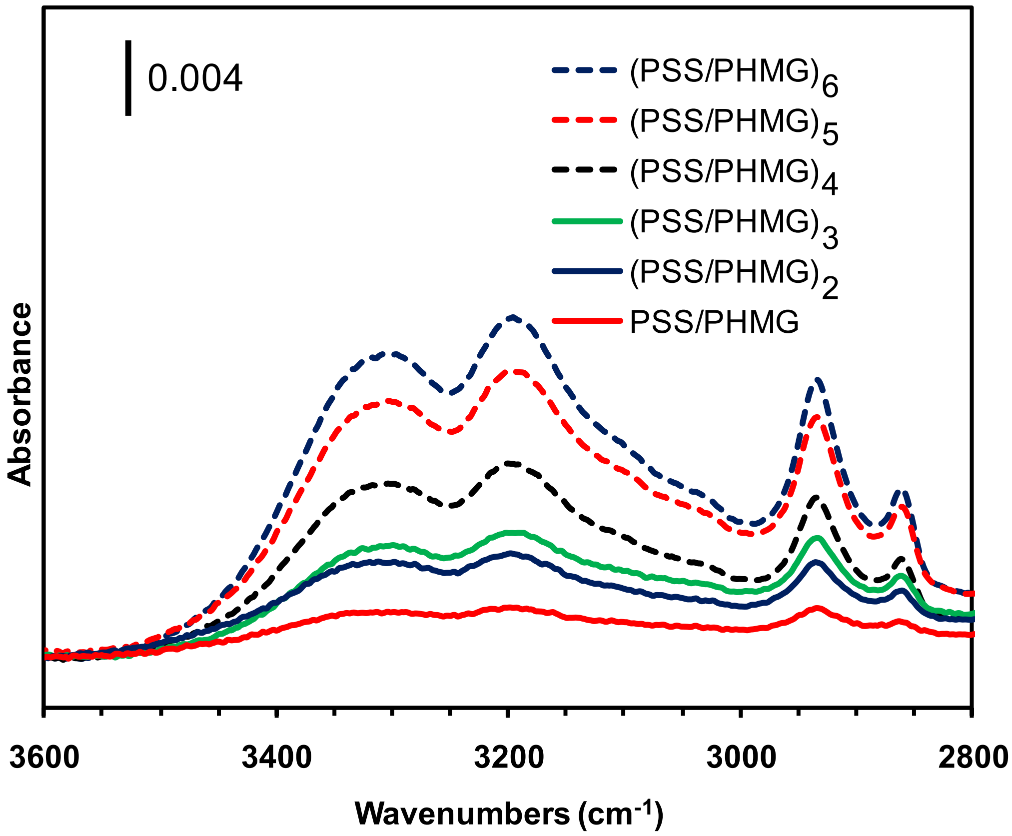

Figure 4.1: Reflectance FTIR spectra (3600-2800 cm^{-1}) of $(PSS/PHMG)_x$ films adsorbed on aluminum-coated Si wafers.

With the exception of the 3-bilayer coating, the films show an approximately linear increase in film thickness with the number of deposited layers. The figure may suggest an increase in the amount adsorbed per layer after deposition of the third bilayer.

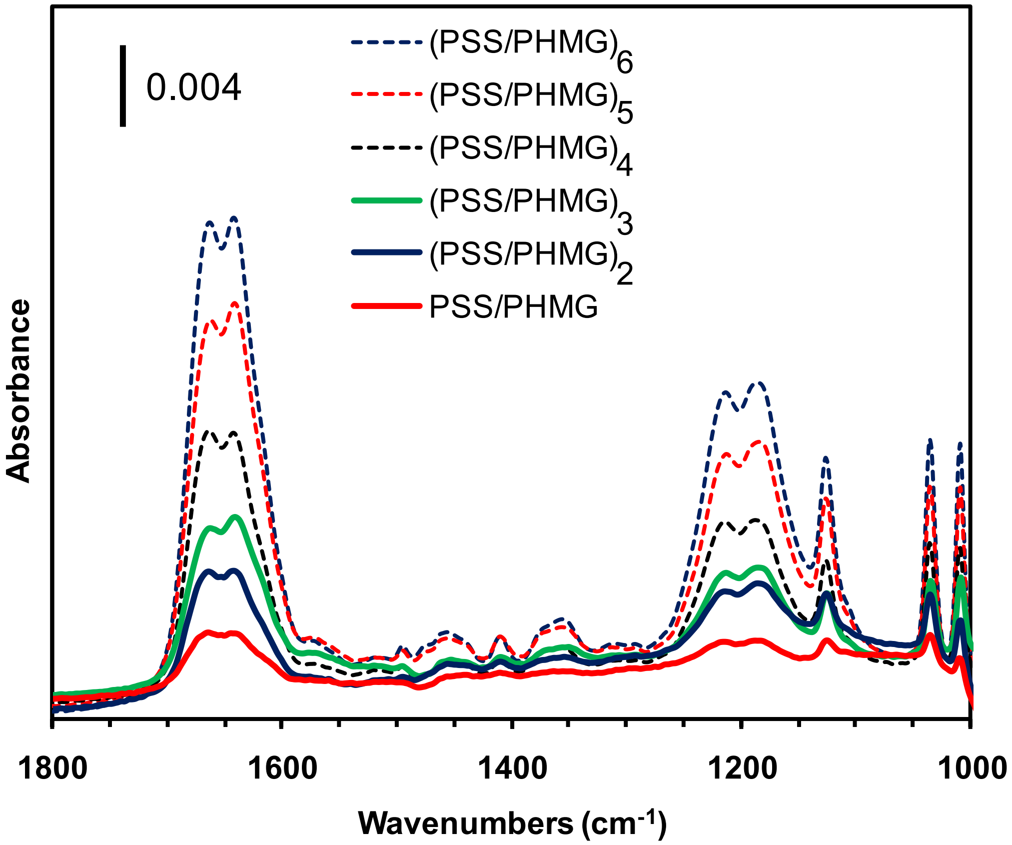

Figure 4.2: Reflectance FTIR spectra (1800-1000 cm^{-1}) of $(PSS/PHMG)_x$ films adsorbed on aluminum-coated Si wafers.

Often in the deposition of polyelectrolyte mulitlayers, deposition of a few priming layers on the substrate precedes regular growth.[32, 49] The spectra of (PSS/PHMB) films show trends similar to those of (PSS/PHMG) films (Figures 4.4-4.6).

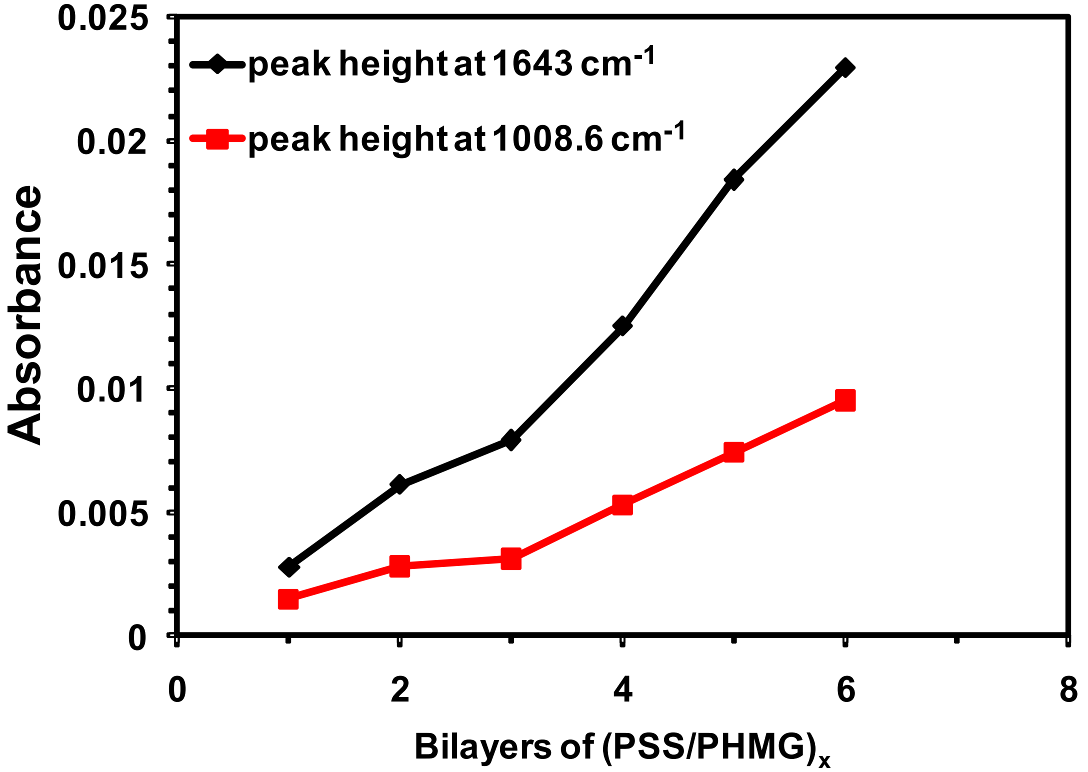

Figure 4.3: Peak heights (1643 and 1008.6 cm^{-1}) in reflectance FTIR spectra of (PSS/PHMG)$_x$ films as a function of the number of adsorbed bilayers, x.

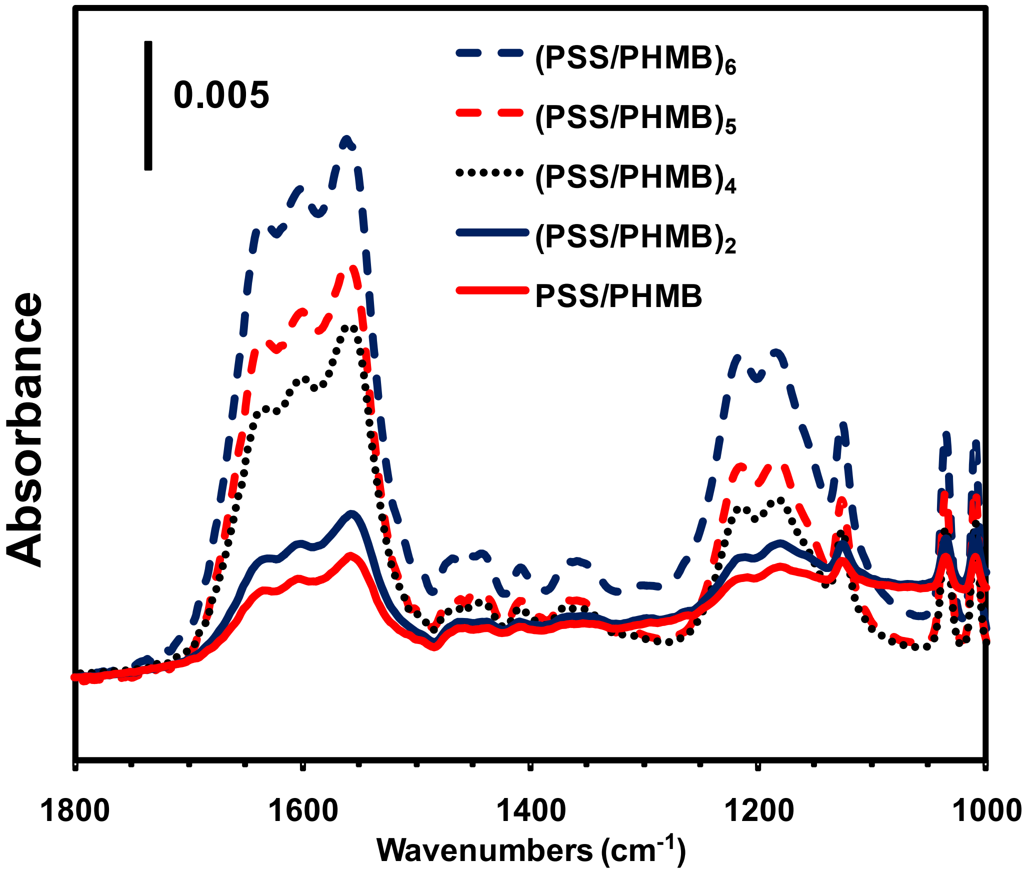

Figure 4.4: Reflectance FTIR spectra (1800-1000 cm^{-1}) of (PSS/PHMB)$_x$ films adsorbed on Al-coated Si wafers.

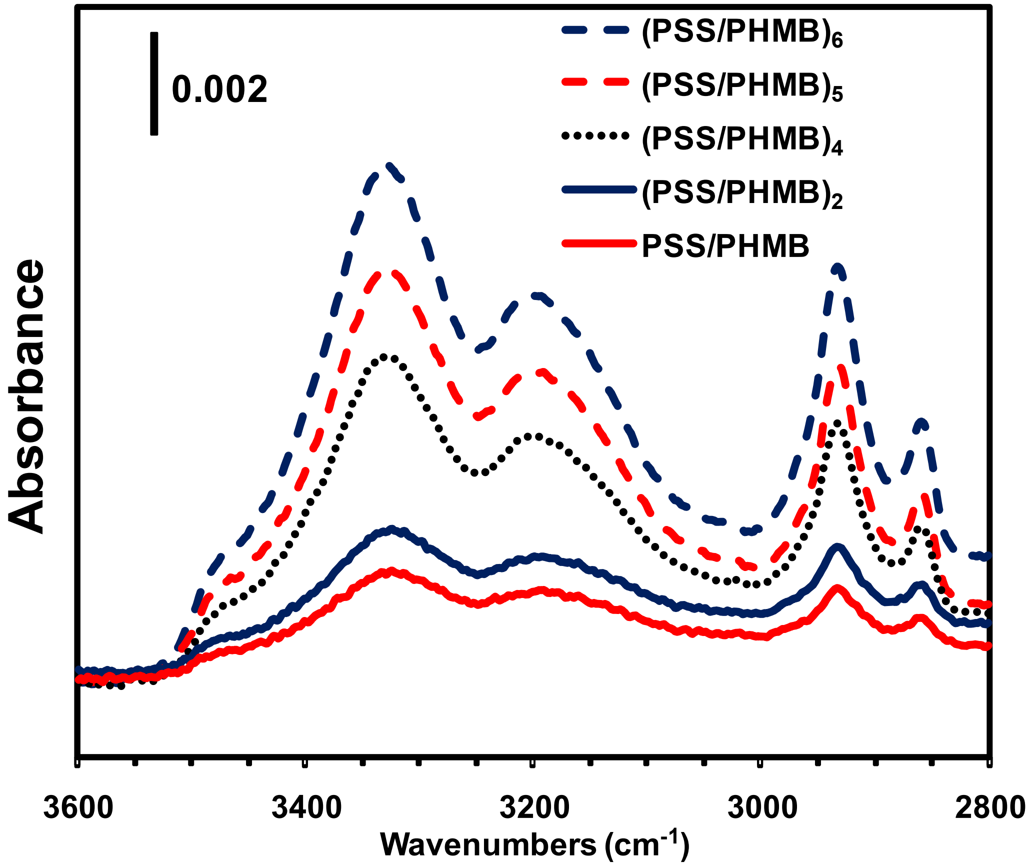

Figure 4.5: Reflectance FTIR spectra of 0.5-6 bilayers of $(PSS/PHMB)_x$ films adsorbed on aluminum-coated Si wafers.

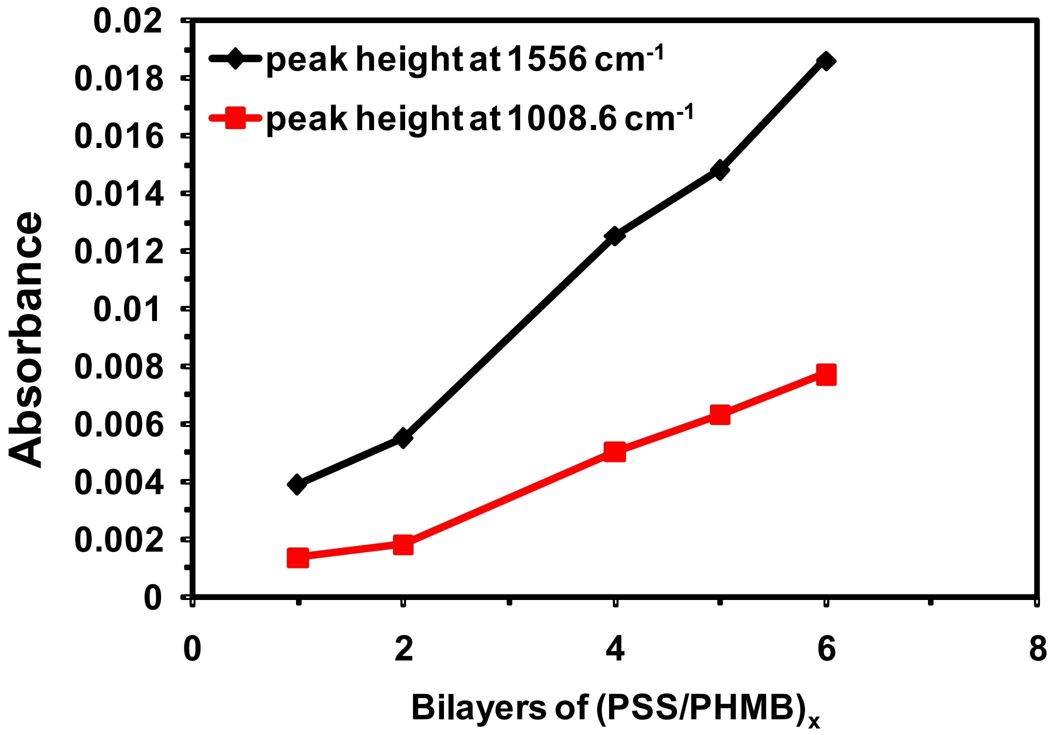

Figure 4.6: The peak heights of reflectance FTIR spectra of $(PSS/PHMB)_x$ films as a function of the number of adsorbed bilayers, x. Absorption increases with every sequential layer.

Zeta Potentials. The rejection of ions in nanofiltration depends in part on Donnan (electrostatic) exclusion, which is a function of the fixed charge in the membrane. The membrane zeta potential, the potential at the slip plane outside the surface relative to the potential in the bulk solution, provides an indication of the surface charge on modified membranes. Figure 4.7 shows how the zeta potentials of modified PES membranes vary with the number of adsorbed PSS/PHMG or PSS/PHMB layers.

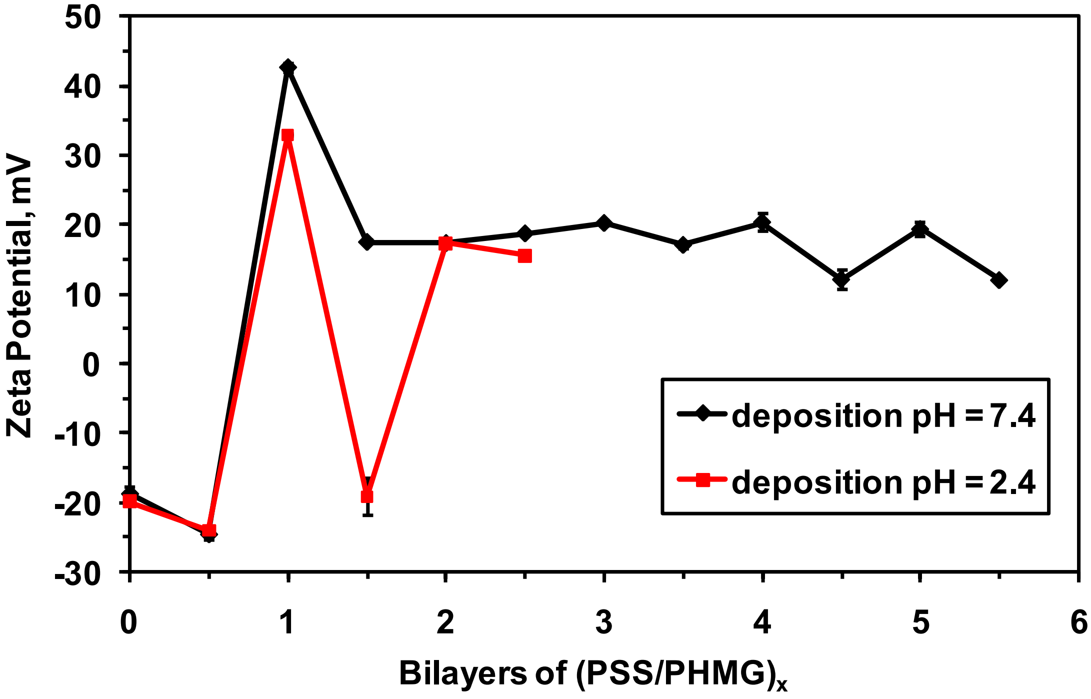

Figure 4.7: Zeta potentials of (PSS/PHMG) multilayers deposited on 50 kDa PES membranes. Each data point represents an average zeta potential of at least two samples generated on the same day using the same solutions. The pH refers to the electrolyte deposition solution as described in the experimental section. (Films with integer numbers of bilayers terminate with PHMG, whereas fractional bilayer numbers indicate termination with PSS.)

The unmodified membranes are negatively charged, and thus they have an inherent negative zeta potential. Deposition of the first PSS layer via hydrophobic interactions introduces more negative charge on the surface and decreases the zeta potential. Subsequent adsorption of PHMG at pH 7.4 changes the zeta potential from -25 mV to +43 mV, which is consistent with charge reversal due to polycation adsorption. However, all further deposition steps at pH 7.4, up to the formation of 5.5-bilayer films, give a zeta potential around 20 mV. The lack of negative zeta potentials after PSS deposition could indicate a lack of polyelectrolyte adsorption, but this is inconsistent with the nanofiltration flux declines after deposition of each layer (see below). Another possible explanation for the consistently positive zeta potentials is that these film undergo exponential growth where the polycation diffuses throughout the film, so that zeta potentials are always positive.[32] However, the IR data given above suggest a regular film growth after adsorption of each layer. At this point, we do not understand the trends in zeta potentials.

Deposition pH may also affect the zeta potentials of PSS/PHMG films by altering the extent of protonation of the guanidine groups of PHMG. The typical pKa_1 of guanidine groups is 13.6 and in PHMB the pKa_2 is 2.8.[33] To increase the charge density on PHMG groups, we deposited films at pH 2.4, and this results in a zeta potential of -20 mV after deposition of the second PSS layer. However, for films consisting of 2 and 2.5-bilayers, zeta potentials were similar to those for films deposited at pH 7.4, i.e., the zeta potential stays at 20 mV.

Antibacterial Activity. The dependence of the deposition solution on the antibacterial activity of the films against *E. coli* was tested. A recent publication compared the bactericidal activity of different oligomers (5 – 50 units) of bisphenol-A, propoxide, or methoxide, all chain-end-modified with guanidine (end-caps).[50] In solution, the oligomer chains with only two guanidine moieties per chain showed a minimal inhibitory concentration of 180 ppm for Pseudomonas aeruginosa and 140 ppm for Staphylococcus aureus.[50] When these oligomers were deposited on 0.05 μm pore size polyethylene terephthalate (PET) track-etched membranes, in a manner similar to the one in this chapter, oligomer-modified membranes showed 100 % bactericidal activity when the deposition solution was 1000 ppm guanidine-containing oligomer.[50] Despite only having antibacterial active sites at the end of the oligomers, it was interpreted that high activity was due to the ability of the guanidine groups to dangle away from the surface. In a separate study, the adsorption of PHMB on cellulose with deposition solutions at these concentrations have been attributed to a combination of electrostatic interactions and hydrogen-bonding forces.[33] The PHMG and PHMB used in this study contain significantly higher density of guanidine units, and therefore should provide high bactericidal activity. Presumably, the number of functional groups needed to provide sufficient adhesion is only a small fraction of the guanidine units, which will leave guanidine moieties available as antibacterial sites.

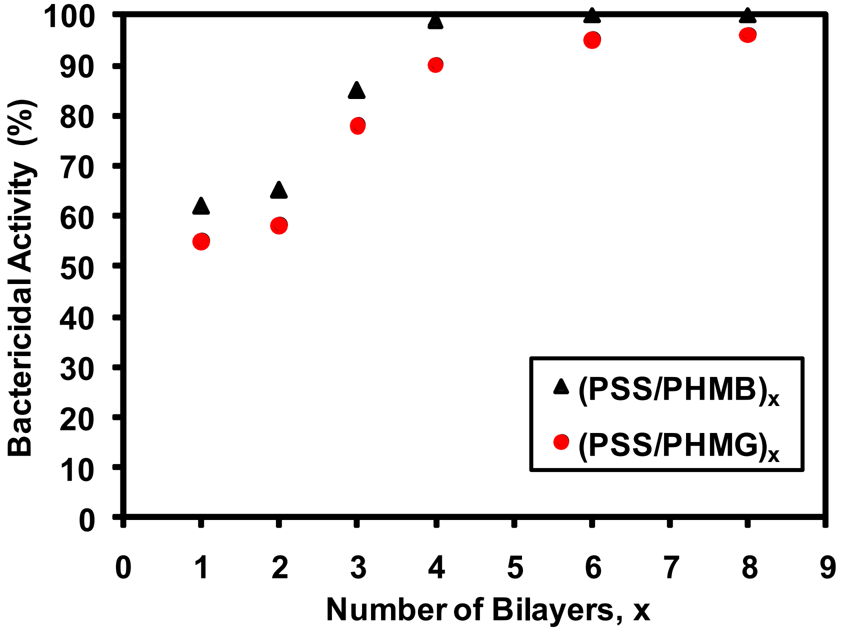

Figure 4.8: The bactericidal activity of 20 kDa PES membranes coated with $(PSS/PHMB)_x$ and $(PSS/PHMG)_x$ films. Activity was calculated by counting the number of colony forming units on bare and coated membranes [see Eq. (1.2)].

Figure 4.8 shows the antibacterial activities of $(PSS/PHMB)_x$ and $(PSS/PHMG)_x$ films on PES membranes. In both cases the antibacterial activity increases with the number of adsorbed bilayers, and remarkably, the (PSS/PHMB) films reach 100 % bactericidal activity after deposition of 6 bilayers. The (PSS/PHMB) films show higher antibacterial activity than (PSS/PHMG) regardless of the numbers of layers in the film, which is consistent with the higher density of guanidinium groups in PHMB.

Transport properties. Figure 4.9 shows the pure water permeability, m3×m^{-2}×d^{-1}×MPa^{-1} at a feed pressure of 300 kPa, for PES membranes coated with different numbers of (PSS/PHMG) and (PSS/PHMB) bilayers. As expected, flux decreases with the number of adsorbed bilayers, but even after deposition of 4 bilayers, the membrane permeability is about 9-10% of that through typical commercial membranes.[51] Deposition of 1-bilayer films leads to a greater flux decline for PSS/PHMB than PSS/PHMG, but with adsorption of more bilayers, the fluxes were essentially the same for the two systems. To maximize flux, one should deposit as few bilayers as possible, but the need for high NF selectivities and antibacterial properties will likely dictate the optimal number of bilayers for a particular application.

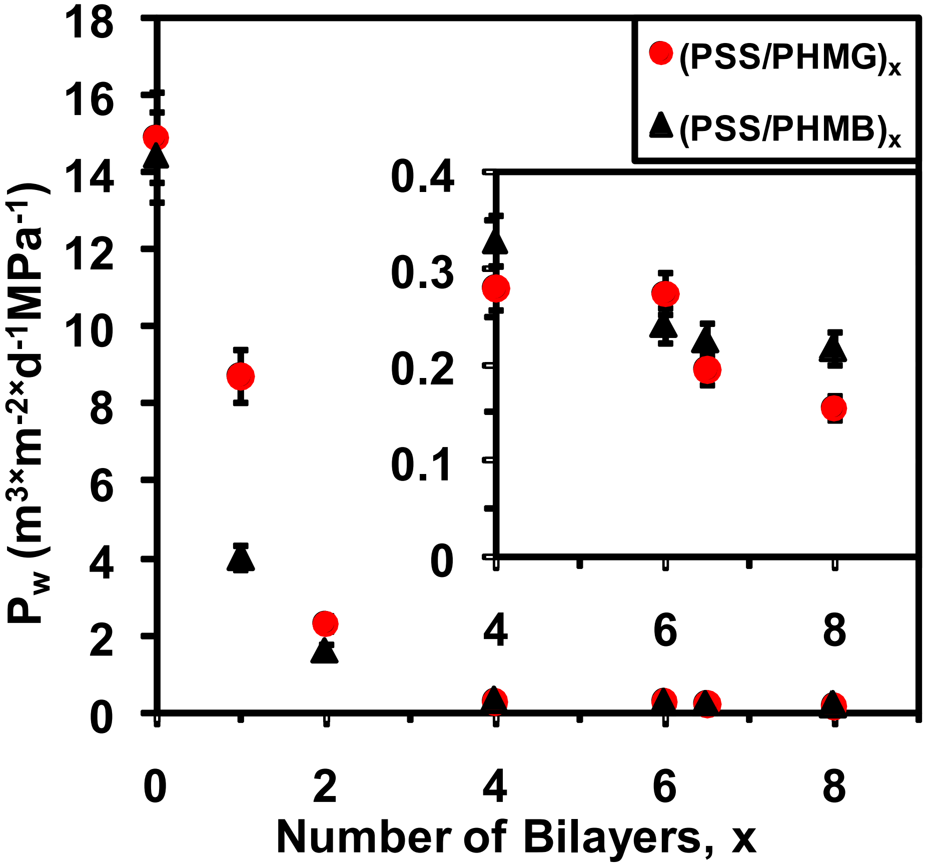

Figure 4.9: Membrane pure water permeability as a function of the number of bilayers, x, for $(PSS/PHMG)_x$- and $(PSS/PHMB)_x$-modified 20 kDa PES ultrafiltration membranes. The pure flux was measured under a transmembrane pressure of 300 kPa.

Figures 4.10 and 4.11 show the NaCl and $MgSO_4$ rejections of 20 kDa PES ultrafiltration membranes coated with different numbers of PSS/PHMB or PSS/PHMG bilayers. Both the NaCl and $MgSO_4$ rejections are higher for PSS/PHMB than for PSS/PHMG films with the same number of bilayers. However, in all cases, the rejection is less than 50%, suggesting that these membranes are not very selective. Nevertheless, this conclusion must be viewed with some caution because filtration in the dead-end cell can lead to very high concentration polarization, which will limit rejection. Future studies will examine these membranes in cross-flow nanofiltration where the degree of concentration polarization will be much less. Additionally, our previous studies show that rejection depends on the substrate, and the 50 kDa Pall membranes do not lead to as high of rejections as 50 kDa substrates from Millipore.[44]

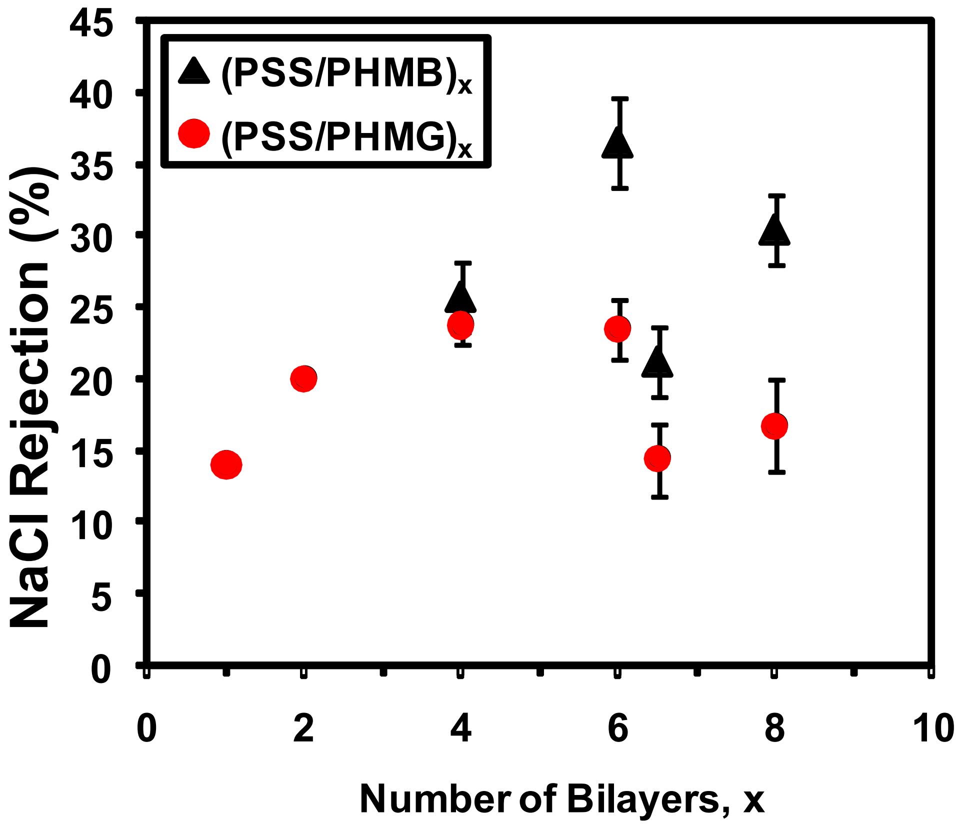

Figure 4.10: NaCl rejection in dead-end filtration of 0.01 M NaCl solutions through 20 kDa PES ultrafiltration membranes coated with $(PSS/PHMB)_x$ (black triangles) and $(PSS/PHMG)_x$ (red circles) films.

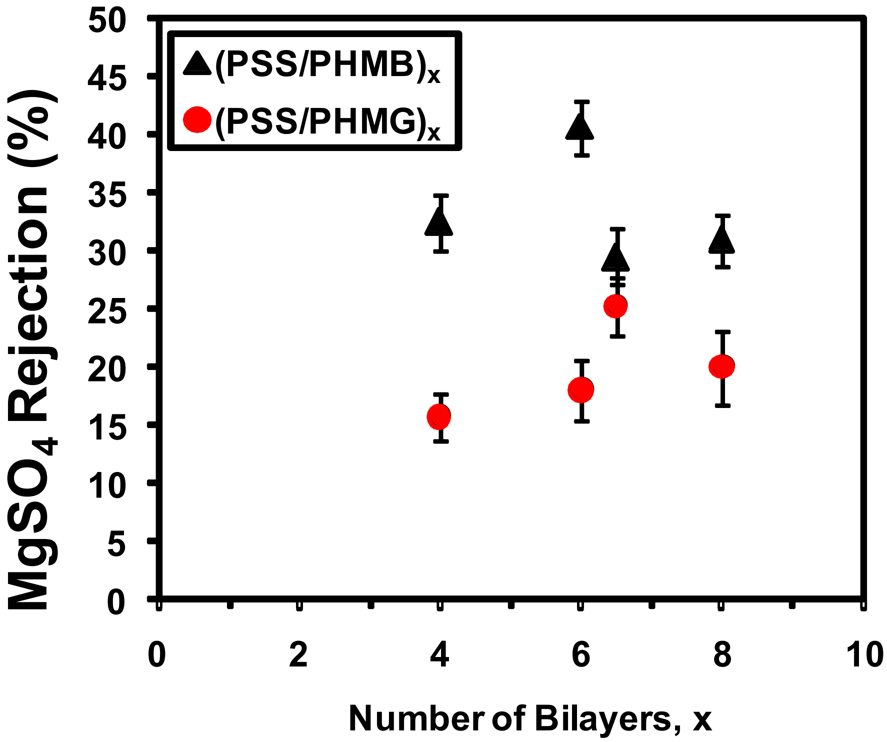

Figure 4.11: $MgSO_4$ rejection in dead-end filtration of 0.01 M $MgSO_4$ solutions through 20 kDa PES ultrafiltration membranes coated with $(PSS/PHMB)_x$ (black triangles) and $(PSS/PHMG)_x$ (red circles) films.

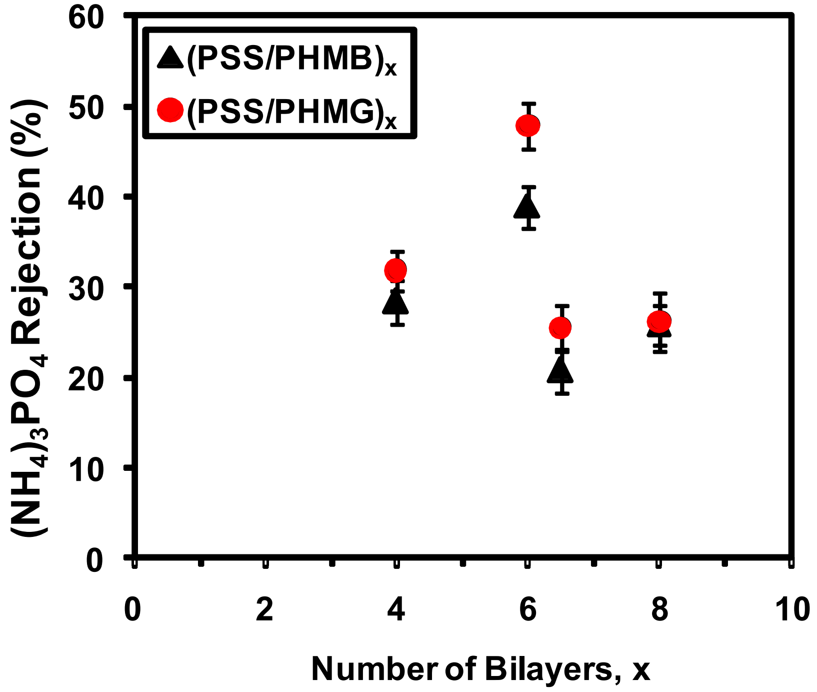

Figure 4.12: $(NH_4)_3PO_4$ rejection in dead-end filtration of 0.01 M $(NH_4)_3PO_4$ solutions through 20 kDa PES ultrafiltration membranes coated with $(PSS/PHMB)_x$ (black triangles) and $(PSS/PHMG)_x$ (red circles) films.

Figure 4.12 shows the $(NH_4)_3PO_4$ Rejections by PSS/PHMG and PSS/PHMB-modified membranes. In this case, the PHMG and PHMB ammonium rejections were comparable, but the rejections are still very low, suggesting that the membranes skins are highly swollen.[52]

Conclusions

Surface modification of porous PES membranes with either $(PSS/PHMB)_x$ or $(PSS/PHMG)_x$ creates surfaces with antibacterial properties. Reflectance FTIR spectra confirm the layer-by-layer growth of the polyelectrolyte films on aluminum-coated Si, but the zeta potentials of coated membranes do not oscillate between positive and negative values after deposition of polycations and polyanions, as would be expected. The 20 mV zeta potential of films with more than 2 bilayers suggests an excess of PHMB or PHMG in these films. Decreases in water flux with an increasing number of (PSS/PHMB) or (PSS/PHMG) bilayers on PES membranes confirms regular film growth in spite of the constant zeta potential. Preliminary filtration studies show low NaCl, $MgSO_4$, and $(NH_4)_3PO_4$ rejections, but this may occur due to a high degree of concentration polarization in the dead-end filtration cells.

REFERENCES

REFERENCES

(1) Bhattacharyya, D.; Hestekin, J.; Shah, D.; Ritchie, S. *J. Chin. Inst. Chem. Eng.* **2002,** 33, 61-66.

(2) Reissmann, F. G.; Uhl, W. *Desalination* **2006,** 198, 225-235.

(3) Kontek Ecology Systems, I. Microfiltration Systems. http://www.kontekecology.com/files/micro.pdf (accessed Sept. 2, 2010).

(4) Susanto, H.; Ulbricht, M. *J. Membr. Sci.* **2005,** 266, 132-142.

(5) Frank, B. P.; Belfort, G. *Langmuir* **1997,** 13, 6234-6240.

(6) Chambers, L. D.; Stokes, K. R.; Walsh, F. C.; Wood, R. J. K. *Surf. Coat. Technol.* **2006,** 201, 3642.

(7) Schumacher, J. F.; Carman, M. L.; Estes, T. G.; Feinberg, A. W.; Wilson, L. H.; Callow, M. E.; Callow, J. A.; Finlay, J. A.; Brennan, A. B. *Biofouling* **2007,** 23, 55.

(8) Hovgaard, M. B.; Rechendorff, K.; Chevallier, J.; Foss, M.; Besenbacher, F. *J. Phys. Chem. B* **2008,** 112, 8241.

(9) Genzer, J.; Efimenko, K. *Biofouling* **2006,** 22, 339.

(10) Callow, J. A.; Callow, M. E.; Ista, L. K.; Lopez, G.; Chaudhury, M. K. *J. R. Soc. Interface* **2005,** 2, 319.

(11) Schmidt, D. L.; Brady, R. F.; Lam, K.; Schmidt, D. C.; Chaudhury, M. K. *Langmuir* **2004,** 20, 2830.

(12) Krishnan, S.; Ayothi, R.; Hexemer, A.; Finlay, J. A.; Sohn, K. E.; Perry, R.; Ober, C. K.; Kramer, E. J.; Callow, M. E.; Callow, J. A.; Fischer, D. A. *Langmuir* **2006,** 22, 5075.

(13) Krishnan, S.; Wang, N.; Ober, C. K.; Finlay, J. A.; Callow, M. E.; Callow, J. A.; Hexemer, A.; Sohn, K. E.; Kramer, E. J.; Fischer, D. A. *Biomacromolecules* **2006,** 7, 1449.

(14) HoipkemeierWilson, L.; Schumacher, J.; Carman, M.; Gibson, A.; Feinberg, A.; Callow, M.; Finlay, J.; Callow, J.; Brennan, A. *Biofouling* **2004,** 20, 53.

(15) Dudley, L. Y.; Darton, E. G. *Desalination* **1997,** 110, 11-20.

(16) Ma, W.; Zhao, Y.; Wang, L. *Desalination* **2007,** 203, 256-259.

(17) Kwak, S.-Y.; Kim, S. H.; Kim, S. S. *Environ. Sci. Technol.* **2001,** 35, 2388-2394.

(18) Zhao, Y.-J.; Wu, K.-F.; Wang, Z.-J.; Zhao, L.; Li, S.-S. *J. Env. Sci.* **2000,** 12, 241-251.

(19) Grunlan, J. C.; Choi, J. K.; Lin, A. *Biomacromolecules* **2005,** 6, 1149-1153.

(20) Jansen, B.; Kohnen, W. *J. Ind. Microbiol.* **1995,** 15, 391-396.

(21) Lee, D.; Cohen, R. E.; Rubner, M. F. *Langmuir* **2005,** 21, 9651-9659.

(22) Fu, J.; Ji, J.; Yuan, W.; Shen, J. *Biomaterials* **2005,** 26, 6684-6692.

(23) Rabea, E. I.; Badawy, M. E. T.; Stevens, C. V.; Smagghe, G.; Steurbaut, W. *Biomacromolecules* **2003,** 4, 1457-1465.

(24) Cen, L.; Neoh, K. G.; Kang, E. T. *Langmuir* **2003,** 19, 10295-10303.

(25) Nakagawa, Y.; Hayashi, H.; Tawaratani, T.; Kourai, H.; Horie, T.; Shibasaki, I. *Appl. Environ. Microbiol.* **1984,** 47, 513-518.

(26) Tiller, J. C.; Liao, C.-J.; Lewis, K.; Klibanov, A. M. *Proc. Natl. Acad. Sci. U. S. A.* **2001,** 98, 5981-5985.

(27) Harris, J. J.; Stair, J. L.; Bruening, M. L. *Chem. Mater.* **2000,** 12, 1941-1946.

(28) Hollman, A. M.; Bhattacharyya, D. *Langmuir* **2004,** 20, 5418-5424.

(29) Krasemann, L.; Tieke, B. *Mat. Sci. & Eng. C* **1999,** 8-9, 513-518.

(30) Malaisamy, R.; Bruening, M. L. *Langmuir* **2005,** 21, 10587-10592.

(31) Smuleac, V.; Butterfield, D. A.; Bhattacharyya, D. *Langmuir* **2006,** 22, 10118-10124.

(32) Adusumilli, M.; Bruening, M. L. *Langmuir* **2009,** 25, 7478-7485.

(33) Blackburn, R. S.; Harvey, A.; Kettle, L. L.; Payne, J. D.; Russell, S. J. *Langmuir* **2006,** 22, 5636-5644.

(34) Lim, N.; Goh, D.; Bunce, C.; Xing, W.; Fraenkel, G.; Poole, T. R. G.; Ficker, L. *Amer. J. Ophthal.* **2008,** 145, 130-135.

(35) Kim, B. R.; Anderson, J. E.; Mueller, S. A.; Gaines, W. A.; Kendall, A. M. *Water Res.* **2002,** 36, 4433-4444.

(36) Kawabata, A.; Taylor, J. A. *Dyes Pigm.* **2006,** 68, 197-204.

(37) Gilbert, P.; Moore, L. E. *J. Appl. Microbiol.* **2005,** 99, 703.

(38) Broxton, P.; Woodcock, P. M.; Gilbert, P. *J. Appl. Bacteriol.* **1983,** 54, 345.

(39) Ikeda, T.; Ledwith, A.; Bamford, C. H.; Hann, R. A. *Biochim. Biophys. Acta* **1984,** 769, 57.

(40) Wei, D. F.; Ma, Q. X.; Guan, Y.; Hu, F. Z.; Zheng, A. N.; Zhang, X.; Teng, Z.; Jiang, H. *Mater. Sci. Eng. C-Mater. Biol. Appl.* **2009,** 29, 1776-1780.

(41) Qian, L. Y.; Guan, Y.; He, B. H.; Xiao, H. N. *Polymer* **2008,** 49, 2471-2475.

(42) Bazaron, L. U.; Stel'makh, S. A. *Russ. J. App. Chem.* **2008,** 81, 2021-2025.

(43) Xiong, Y.; Liu, Y. *Appl. Microbiol. Biotechnol.* **2010,** 86, 825-837.

(44) Ouyang, L.; Malaisamy, R.; Bruening, M. L. *J. Membr. Sci.* **2008,** 310, 76-84.

(45) East, G. C.; McIntyre, J. E.; Shao, J. *Polymer* **1997,** 38, 3973-3984.

(46) Lehtinen, J.; Nuutila, J.; Lilius, E.-M. *Cytometry, Part A* **2004,** 60A, 165-172.

(47) Lin-Vien, D.; Colthup, N. B.; Fateley, W. G.; Grasselli, J. G. *The Handbook of Infrared and Raman Characteristic Frequencies of Organic Molecules*. Academic Press: San Diego, 1991.

(48) Barker, J.; Kilner, M. *Coord. Chem. Rev.* **1994,** 133, 219-300.

(49) Bruening, M. L.; Dotzauer, D. M.; Jain, P.; Ouyang, L.; Baker, G. L. *Langmuir* **2008,** 24, 7663-7673.

(50) Vakuliuk, P.; Burban, A.; Konovalova, V.; Bryk, M.; Vortman, M.; Klymenko, N.; Shevchenko, V. *Desalination* **2009,** 235, 160-169.

(51) The Dow Chemical Company. Filmtec Membranes. http://www.dow.com/PublishedLiterature/dh_006b/0901b8038006bfea.pdf?filepath=liquidseps/pdfs/noreg/609-00346.pdf&fromPage=GetDoc (accessed Sep. 2, 2010).

(52) Miller, M. D.; Bruening, M. L. *Chem. Mater.* **2005,** 17, 5375-5381.